UNIVERSITY OF SOUTHAMPTON

FACULTY OF ENGINEERING SCIENCE AND MATHEMATICS

School of Engineering Sciences

Probabilistic Manufacturing Variability Quantification from Measurement Data for Robust Design of Turbine Blades

by

Nikita Thakur

Thesis submitted for the Degree of Doctor of Philosophy

May 2010

UNIVERSITY OF SOUTHAMPTON

ABSTRACT

FACULTY OF ENGINEERING, SCIENCE AND MATHEMATICS

SCHOOL OF ENGINEERING SCIENCES

Doctor of Philosophy

PROBABILISTIC MANUFACTURING VARIABILITY QUANTIFICATION FROM MEASUREMENT DATA FOR ROBUST DESIGN OF TURBINE BLADES

by Nikita Thakur

Turbine blades are critical to the performance of an aircraft engine and their life is central to the integrity of the engine. These blades, when manufactured, inevitably exhibit some deviations in shape from the desired design specifications as a result of manufacturing variability. An approach to characterizing these deviations may be made by analysing the blade measurements for any changes from the datum design values. The measurement data, is however, always affected by measurement errors that cloud these effects.

In the present study, a methodology is proposed that employs the probabilistic data analysis techniques of Principal Component Analysis (PCA) and Fast Fourier Transform (FFT) analysis for de-noising the measurement data to capture the underlying effects of manufacturing variability as manufacturing drift with time and blade to blade manufacturing error. An approach using dimensionality reduction in the case of PCA and sub-selecting Fourier coefficients in the case of FFT is proposed that uses prior knowledge on the measurement error. A Free-Form Deformation (FFD) based methodology is then presented for characterizing the 3-dimensional (3-d) geometric variability in blade shapes from the limited number of available measurements. This is followed by the application of a linear elasticity based approach for generating and morphing 3-d volume meshes in FEA ready form. A finite element analysis (FEA) of the resulting probable blade shapes indicates that the presence of manufacturing variability reduces their mean life by about 1.7% relative to the nominal design with a maximum relative reduction in life of around 3.7%. The probabilistic estimates of manufacturing perturbations are employed for robust design studies with the objectives of maximizing the mean and nominal lives and minimizing the blade life variability. A comparison of the robust-optimal solution with an optimal deterministic design is also performed. The designs explored by the multiobjective optimization process are analysed to understand the effects of geometric changes in turbine blades on the nominal values of life and the variations in blade life.

Contents

List of Figures

List of Tables

Declaration Of Authorship

I, **Nikita Thakur**, declare that the thesis entitled **Probabilistic Manufacturing Variability Quantification from Measurement Data for Robust Design of Turbine Blades** and the work presented in it are my own. I confirm that:

- this work was done wholly or mainly while in candidature for a research degree at this University;
- where any part of this thesis has previously been submitted for a degree or any other qualification at this University or any other institution, this has been clearly stated;
- where I have consulted the published work of others, this is always clearly attributed;
- where I have quoted from the work of others, the source is always given. With the exception of such quotations, this thesis is entirely my own work;
- I have acknowledged all main sources of help;
- where the thesis is based on work done by myself jointly with others, I have made clear exactly what was done by others and what I have contributed myself;
- parts of this work have been published and some articles are under review as:
    1. N. Thakur, A. Keane, P.B. Nair, Capture of Manufacturing Uncertainty in Turbine Blades through Probabilistic Techniques, in: Proceedings of the 7th ASMO-UK/ISSMO International Conference on Engineering Design Optimization, Bath, UK, 2008, pp. 387-396.
    2. N. Thakur, A. Keane, P.B. Nair, Probabilistic Analysis of Manufacturing Uncertainty in Turbine Blades, in: Proceedings of the ASME 2009 International Design Engineering Technical Conferences & Computers and Information in Engineering

Conference (IDETC/CIE 2009), no. DETC2009-86190, San Diego, California, USA, 2009.

3. N. Thakur, A.J. Keane, P.B. Nair, Estimating the effect of Manufacturing Variability on Turbine Blade Life, in: M. Beer, R.L. Muhanna, R.L. Mullen (Eds.), Proceedings of the 4th International Workshop on Reliable Engineering Computing (REC 2010), Singapore, 2010, pp. 311-322.
4. N. Thakur, A. Keane, P.B. Nair, A.R. Rao, Probabilistic Measurement Data Analysis for estimating the impact of Manufacturing Variability on Turbine Blade Life, ASME Journal of Mechanical Design - Under Review.
5. N. Thakur, A.J. Keane, P.B. Nair, Robust Design of Turbine Blades against Manufacturing Variability, (In Preparation).

Signed:..
Date:...

Acknowledgements

I would like to express my gratitude to my supervisor, Prof. A. J. Keane, for his tremendous support, motivation and ideas and for always being willing to offer his advice. I am also very thankful to my co-supervisor, Dr. P. B. Nair, for his insightful discussions and constant encouragement. I owe a big thanks to Abhijit R. Rao and Mike Wardle for their technical support in SCO3 related problems and for providing the SCO3 plugins, turbine blade models and lifing analysis codes. I am obliged to Ivan, Maria and Tony for helping me in setting up the iSIGHT workflow and for clarifying my doubts from time to time.

The discussions held with Dave Knott and Richard Latham on the turbine blade manufacturing and measurement procedures were very insightful and their help in facilitating this research by providing the measurement datasets is highly appreciated. A special thanks to Ron Bates, Amar Singh Bedi and Tamsyn Thorpe for going through the trouble of reading and re-reading my papers and thesis for the Rolls-Royce approval process.

I owe a lot to my parents for their encouragement and blessings, and for helping me pull through tough times. Many thanks to Apurva for his emotional support and professional guidance and for surviving through all my tantrums. A special mention to my parents-in-law for being caring and supportive towards my efforts. I have had some great times in the department with Sanjay, Felix, Asha, Moresh, Surya and Thanasius and would like to thank all of them for their cheerful talks.

This work was supported by Rolls-Royce plc. and the UK DTI. I would like to take this opportunity to thank the Computational Engineering and Design Group, University of Southampton for facilitating this research with an excellent working environment.

Nomenclature

$(\quad)^T$	Transpose of a matrix
α	Number of model divisions in the **S** direction
β	Number of model divisions in the **T** direction
$\boldsymbol{\sigma}$	Cauchy stress tensor
Δt	Sampling time interval
δ	Vector containing the threshold errors for the measurement point locations
ϵ	Normally distributed error terms
γ	Number of model divisions in the **U** direction
ν	Poisson's ratio
$\overline{\mathbf{VAR}}$	Overall mean of the threshold variances
$\overline{\mathbf{X}}$	Matrix populated with the row-wise means for **X**
$\mathbf{C_Y}$	Covariance matrix of **Y**
$\mathbf{G}_{ijk}$	Vector containing the Cartesian coordinates of the control points
$\mathbf{I}_t$	Identity tensor
$\mathbf{lb_x}$	Vector containing lower bounds for the x-coordinates of the control points
$\mathbf{lb_y}$	Vector containing lower bounds for the y-coordinates of the control points
$\mathbf{P_0}$	Origin of the local coordinate system
$\mathbf{P}_{ffd}$	Vector containing the Cartesian coordinates of the displaced point

$\mathbf{ub_x}$	Vector containing upper bounds for the x-coordinates of the control points
$\mathbf{ub_y}$	Vector containing upper bounds for the y-coordinates of the control points
$\mathbf{X}_0$	Mean-centered data matrix for one-off measurements
$\mathbf{x_{g0}}$	Vector containing the nominal x-coordinates of the control points
$\mathbf{x_g}$	Vector containing x-coordinates of the control points
$\mathbf{y_g}$	Vector containing y-coordinates of the control points
L_1	Lamé's first parameter
L_2	Lamé's second parameter
θ_h	Kriging hyperparameter measuring the 'activity' of an input variable
B	Bernstein polynomial
$bldt$	Temperature applied to the blade
$C1$	Canonical variable representing the maximum separation between groups
$C2$	Canonical variable orthogonal to $C1$ and representing the maximum separation between groups
E	Young's modulus
f	Frequency
F^o	Fourier transform formed from the odd components
F^e	Fourier transform formed from the even components
g	Number of time-based groups
l	Number of operators
m	Number of measured samples
N	Number of measurements taken with respect to time
n	Number of measurements taken

$N_{critical\ life}$	Critical life of turbine blades expressed as number of cycles
N_{life}	LCF life of turbine blades expressed as number of cycles
nf	Scaling factor for shaft speed
p	Total number of repeated measurements per sample
p_h	Kriging hyperparameter defining smoothness
pf	Scaling factor for gas loads
q	Number of samples for repeated measurement dataset
r	Number of repeated measurements per operator
R^2	Correlation coefficient
$Rfact$	Normalized value of life
std	Standard deviation
T_0	Temperature subjected to the blade
$thot$	Temperature scaling factor for running conditions
$tmap$	Mapped temperatures obtained from thermal analysis
Var	Variance
x_d	Deformed x-coordinate position
x_e	Desired x-coordinate position
y_d	Deformed y-coordinate position
y_e	Desired y-coordinate position
z_g	Control point coordinate along the Z-axis
$\mathbf{C}$	Matrix containing the product of Bernstein polynomials
$\mathbf{d}$	Vector containing the desired values of x-coordinates for measurement points
$\mathbf{e}$	Vector containing the values of measurement error

f	External force applied on the node
N(j)	Matrix containing the repeated measurement dataset for the j_{th} sample
P	A point on the model in the local coordinate system
VAR	Vector containing the threshold variance values
var(j)	Variance matrix for the j_{th} sample
v	Vector containing the true value of measurements
w	Displacement field for the volume mesh
X	Data matrix consisting of one-off measurements
CAD	Computer Aided Design
CDI	Changing the Design
CE	Center
DFT	Discrete Fourier Transform
DOE	Design of Experiments
FEA	Finite Element Analysis
FFD	Free Form Deformation
FFT	Fast Fourier Transform
LCF	Low Cycle Fatigue
LE	Leading Edge
LES	Linear Elasticity Solving
LLS	Linear Least-Squares
MANOVA	Multivariate Analysis of Variance
MTO	Maximum Take-Off
MVA	Manufacturing Variability Analysis

NSGA-II	Nondominated Sorting Genetic Algorithm
PCA	Principal Component Analysis
PS	Pressure Surface
RSM	Response Surface Model
SS	Suction Surface
TE	Trailing Edge
TM	Threshold magnitude for Fourier coefficients
tr	Trace of a matrix

Chapter 1

Introduction

1.1 Motivation

Turbine blades are critical to the performance of gas turbine engines. Efficient design and manufacture of turbine blades is an area of extensive research because of the contribution it has in improving the overall efficiency of the engine. It may take months for an entire team of analysts, design engineers and manufacturing engineers to design a turbine blade that meets the expected life and performance specifications. However, the manufactured blades inevitably exhibit some deviations from their desired shape due to the presence of manufacturing variability. This variability may result due to various contributing factors, e.g., changes in the surrounding temperature and humidity levels while manufacturing, slight deviations from the desired shape in the dies used for casting, wear and tear of the tools, hand-finishing operations like polishing and grinding, human error, etc.

It is usually very expensive or perhaps even impossible to eliminate these sources of variability in the system. The resulting deviations or the geometric variability in the manufactured shapes may lead to variations in the overall efficiency, performance and life of these blades from their designed values. This has become an important issue in the aircraft engine manufacturing industry. With the introduction of new market paradigms like *Power By The Hour* and *TotalCare* contracts, engine manufacturers have undertaken the responsibility for providing overall lifetime support to the engine, from the time the engine is delivered to the customer until it goes out of service [1, 2, 3]. The implications of *Power By The Hour* contracts on turbine blade lifing are clearly indicated in the recent work of Bagnall et al. [4]. The effects of manufacturing variability on turbine blade shapes may result in unpredictable behaviour of these blades in operating conditions, reduced efficiency during operation, or even reduced life, ultimately leading to company losses. This has lead to the increasing interest in identification of the sources of manufacturing variability and estimation of their effects on blade life and performance. If realistic estimations of these effects are available, this information may further be used for seeking new turbine blade designs with improved performance and lifing robustness in the face of manufacturing variability.

An approach to understanding the effects due to variations in the manufacturing processes may be made by taking measurements on turbine blades and comparing this data with the designed values to characterize any differences in shapes. The measurement data is, however, inevitably clouded by measurement error due to the limitations of the measurement techniques. Therefore, it becomes essential to filter out the measurement error from the measured dataset to capture the underlying effects, and identify the sources of manufacturing variability. Techniques may then be devised to use this information for estimating the 3-dimensional (3-d) geometric variability observed in turbine blade shapes. These 3-d models may further be employed for quantifying the effects of the shape changes on turbine blade lifing properties. If such methodologies can be designed to capture the effects of manufacturing variations from measurement data, robust design studies may then follow in search of new designs with better lifing characteristics and reduced variability in life due to manufacturing variations.

The focus of the present research is to devise methodologies for extracting information from the measurement datasets in order to capture the underlying effects of manufacturing variability. The sources of manufacturing variations are first segregated into manufacturing drift with time and the blade to blade manufacturing error. A methodology that uses limited measurements for characterizing 3-d geometric variability in the manufactured shapes is also proposed. The deformed geometries obtained from the application of this methodology represent the probable shapes of manufactured parts. The information obtained from these geometries is used for obtaining 3-d volume meshes in FEA ready form by mesh morphing. These volume meshes are analysed for estimating the effects of manufacturing variability on turbine blade life. Finally, robust design optimization studies are conducted to result in a new turbine blade design that not only indicates an improved value of designed life, but also demonstrates reduced variability in life in the presence of manufacturing variations.

1.2 Background

In the recent past, there has been a lot of emphasis on capturing and modelling uncertainty and performing probabilistic analyses during the design phase [5, 6]. Recently, the aircraft propulsion industry has also extensively employed probabilistic design methods, driven largely by the need to reduce risk through quantification of uncertainty [7, 8]. Sidwell [9] performed probabilistic analysis on a commercial jet engine to quantify the variability in turbine blade flow and oxidation life due to uncertainty in operating conditions. Moeckel [2] investigated manufacturing variability and its effect on first-stage turbine blades using a parametric geometry model and a finite element thermal model. Garzon [10] applied statistical and probabilistic techniques to assess the impact of geometric and operating condition uncertainty on axial compressor performance. Kumar [1] proposed methods to represent and propagate geometric uncertainty on compressor blades in order to quantify its impact on aerodynamic performance. He also proposed methods for seeking robust optimal compressor blades that have reduced sensitivities to geometric uncertainty caused due to erosion and manufacturing variations. However, the research conducted so far in this area has been limited in its scope either due to the unavailability of measurement data on the final manufactured parts, or, due to its focus on improving the base design rather than identifying and characterizing the nature of manufacturing variabilities influencing the shapes of the final manufactured components. Also, the focus of the research in the literature has been on quantifying the effects of manufacturing variations on 2-d geometries generally using hypothetical values. The present work takes a step further by using the limited available measurements for characterizing the 3-d geometric variability in manufactured components and estimating its effects on the life of these parts.

The present research focuses on the implementation of probabilistic data analysis techniques on measurement data in order to identify the sources of manufacturing variability and estimate the probable actual measurements of manufactured parts. Methodologies making use of geometry manipulation techniques are employed for estimating the 3-d geometric variability observed in turbine blade shapes from the limited number of available measurements. A linear elasticity solving (LES) based approach is then used for morphing the volume mesh of the nominal blade model to obtain FE meshes for the probable manufactured blade shapes. These meshes are employed for estimating the effects of manufacturing variability on the Low Cycle Fatigue (LCF) life of hollow turbine blades at Maximum Take-Off (MTO) conditions. The numerical studies presented are conducted on measurement data available on a randomly selected sample of turbine blades manufactured over a span of one year. The probabilistic estimates of the effects of manufacturing variability are obtained in terms of the mean life and standard deviation in life. Perturbations in the nominal design due to the casting process are calculated and applied on a series of new designs for robust design study. In the end, a robust-optimal solution is obtained that not only indicates improved values of nominal and mean lives as compared to the base geometry, but also results in a reduced variability in life caused by manufacturing perturbations.

The hollow turbine blades considered here are manufactured using a casting process which involves procedures that can result in significant shape variations in these blades from their nominal design. Blade casting is a complicated process involving a series of steps, e.g., designing and creating the molds, pumping in the hot molten metal, cooling of the casts, extraction of the blades from these molds, grinding, etc. In addition, certain less controllable parameters like temperature and humidity levels of the surroundings, wear and tear of the tools, human error, etc., also add to the manufacturing variations. Therefore, quantification and identification of the nature and the sources of manufacturing variability is a significant task. Various experimental methods and techniques, both destructive and non-destructive, may be employed for this purpose.

A destructive technique may be slicing up sample blades and making internal and external measurements on the blade slices. The implementation of this technique depends on the number of blades available for cutting up which may be very expensive due to the high cost of production of each blade. Besides, the technology and procedure used for slicing of the blades has to be carefully selected in order to obtain pieces that are good enough for making precise measurements. Also, the dimensions to be measured and compared with the base model need to be selected and registered with great care.

One form of non-destructive technique would be experimentally obtaining and comparing 3-d scans of the blades with the nominal turbine blade model. This process involves highly-powered X-ray micro-CT (Computed Tomography) scanners for the high density nickel alloy blades being considered. Such powerful micro-CT scanners are not easily available. Even if access to such scanners is available, obtaining 3-d scans on the blades with the desired resolution is a very expensive and time-consuming process. Another non-destructive technique may be physically making measurements on the external surfaces of the manufactured blades and comparing these measurements with the design specifications. This is a relatively complicated process due to the highly complex shape of the turbine blades. Moreover, it gives no idea of the internal variations in the blade shape, especially, for the hollow turbine blades which possess internal design features that are used for blade cooling.

One of the non-destructive techniques used in production is via ultrasonic devices to measure the blade wall thicknesses. This technique uses ultrasonic beams to measure minimum blade wall thicknesses at various cross-sectional planes and at various locations across each plane to give an idea of the final shape of the manufactured blades. Besides using ultrasonic measurement devices, some other non-destructive evaluation techniques that may be used for measuring the wall thicknesses are, impulse-video-thermography [11], X-ray tomography [12] which as discussed previously is highly dependent on the power of the machine available and the density of the blade to be measured, and eddy current techniques [13]. Because of their ready availability, the presented work uses ultrasonic minimum wall thickness measurement data available on a randomly selected sample of hollow turbine blades manufactured over a span of one year. Minimum wall thicknesses hold great importance during fatigue failure, and hence, are measured during the blade inspection process.

The measurements taken through ultrasonic devices are easily corrupted by errors introduced during the measurement process. Some of the sources of this measurement variability are: 1) error in calibration of the measurement devices, 2) error in orientation of the blade when it is held on top of the ultrasonic head, 3) error due to the measured surface being out of view of the operator, 4) human error, etc. Therefore, it becomes essential to filter out any measurement error/noise from the measured data before these thicknesses are compared with the nominal design measurements. The estimated values of manufactured thicknesses may then be used for deforming the nominal turbine blade model in order to obtain probable representations of the manufactured shapes. This may be followed by generating FE meshes on the perturbed geometries for lifing, thermal and stress analysis. The results obtained from the proposed analysis will help develop an understanding of the effects of manufacturing variations on blade life variability. Information obtained from the proposed analysis may further be employed for imposing relatively more realistic perturbations on the various competing base designs to finally enable the selection of a robust nominal design.

1.3 Objectives of the Thesis

The main objectives of the work presented in this thesis are :

1. To propose a practical methodology for de-noising routinely available measurement data in order to capture the underlying effects of manufacturing variability in terms of the manufacturing drift with time and the blade to blade manufacturing error. This methodology makes use of prior information available on measurement error for segregating the random noise from measured datasets to result in probabilistic estimations of the true values of measurements for the manufactured parts.

2. To characterize the 3-d geometric variability observed in turbine blade shapes from the limited number of measurements available per blade. The 3-d representations are used to estimate the effects of manufacturing variability on turbine blade life.

3. To apply the manufacturing perturbations obtained from the turbine blade measurement data analysis for robust design optimization studies. The application of these perturbations on each new design explored by the optimizer helps in obtaining relatively more realistic estimates of the effects of manufacturing variations on blade life variability. It also enables the trading-off between the two robustness metrics of mean life and standard deviation in life against the nominal or designed values of life.

1.3.1 Probabilistic Measurement Data Analysis

A methodology that employs the probabilistic data analysis techniques of Principal Component Analysis (PCA) and Fast Fourier Transform (FFT) analysis is proposed here for filtering out the measurement error from one-off measurements taken on turbine blades manufactured over a year. The one-off measurements consist of data collected during the blade inspection process. Application of the PCA and FFT techniques on these measurements helps in capturing the effects of manufacturing drift with time. An approach to dimensionality reduction in case of PCA and sub-selecting the Fourier coefficients for FFT analysis is proposed that uses prior knowledge available on the measurement error. Information on measurement noise is collected from a repeated set of blade measurements taken on a randomly selected sample of blades manufactured within the same week. These measurements account for most of the random measurement error since they are taken at different measurement stations, by different operators, at different times of the day, and on different days. A statistical analysis of the repeated measurement dataset is also conducted to estimate the blade to blade manufacturing variations. The final collective data representing the effects of manufacturing drift with time and the blade to blade manufacturing error is then used for characterizing the 3-d geometric variability observed in turbine blade shapes from their datum/nominal design.

1.3.2 Representing 3-d Geometric Variability from Limited Measurement Data

A Free-Form Deformation (FFD) based methodology is proposed for representing the 3-d geometric variability observed in turbine blade shapes from the limited number of measurements available per blade. Negligible influence of manufacturing variability is observed on the external blade airfoil geometry. Hence, it is assumed that the brunt of variations due to the manufacturing processes is borne by the internal design features (core) of the blade. The Sederberg and Parry [14] FFD technique is employed here in conjunction with non-linear optimization to deform the nominal core geometry in order to generate different representations of the probable manufactured core shapes. Filtered measurement data, obtained from the PCA and FFT based methodology introduced in Section 1.3.1, is employed for this purpose. Alternatives to the non-linear optimization process, i.e. constrained and unconstrained forms of linear least-squares (LLS) solution, are also explored. The LLS techniques may be preferred if greater deviations from the nominal geometry are sought as compared to the more regularized deformations obtained from the non-linear optimization process.

Information obtained from the deformed core shapes is used for calculating the nodal displacements to be applied to the surface mesh of the nominal core geometry. This aids in morphing the nominal turbine blade volume mesh using a linear elasticity based approach resulting in a series of morphed volume meshes in FEA ready form. Each of these morphed meshes represent a probable manufactured blade shape. A finite element analysis (FEA) on the morphed meshes is then conducted to estimate the effects of manufacturing variability on turbine blade LCF life. These effects are quantified in terms of the mean value of probable lives and the standard deviation in life.

1.3.3 Robust Design of Turbine Blades against Manufacturing Variability

The manufacturing perturbations obtained from the application of the methodologies discussed in Sections 1.3.1 and 1.3.2 above are finally used for robust design optimization of turbine blades. New designs are sought with the objective of improving the mean and nominal lives and reducing the standard deviation in life. A workflow is created in iSIGHT 3.5-1 [15] that employs a combination of computer aided design (CAD), FEA, MATLAB, JAVA, CADfix [16] and Parasolid [17] tools to change the design of the blades and then estimate the effects of manufacturing variability on each of these new designs. Changes to the nominal design are implemented by fixing the external blade geometry and translating and rotating the core in the $\mathbf{X}$ and $\mathbf{Y}$ directions followed by FFD based core shape changes. If the new design so created satisfies the minimum acceptability criterion on the nominal life, it is passed on to the remaining components of the workflow that apply the FFD based manufacturing perturbations to calculate the probable mean life and standard deviation in life. The values of nominal life, mean life and standard deviation are fed as objective functions to a Nondominated Sorting Genetic Algorithm (NSGA-II) [18] based optimizer. The results of the robust design study are compared with the traditional approach of deterministic design optimization and show that the optimal deterministic design may not always be the best solution. It also shows that with a slight compromise in the mean and nominal values of life, significant improvements in the blade life variability can be achieved.

1.4 Scope of the Thesis

The aim of the presented research is to identify, characterize and quantify the effects of manufacturing variations on a real life industrial problem. This work is focused on the manufacturing variability in turbine blade shapes as a result of the blade casting process and its resultant effects on the blade LCF life. A series of methodologies are devised based on existing and well-established techniques for manufacturing variability analysis. This information is then used for a robust design optimization study and its benefits compared with the traditional approach of deterministic design optimization. An introduction to the mathematical concepts behind the implementation of PCA, FFT analysis, FFD and LLS solution in perspective of the present problem is provided in the subsequent chapters. The proposed technique for dimensionality reduction and Fourier coefficient selection based on the prior information available on measurement error is also dicussed in detail. However, indepth mathematical formulations for Multivariate Analysis of Variance (MANOVA), linear elasticity solving method, single objective non-linear optimization processes and NSGA-II are beyond the scope of the present work. The focus of the research is on devising strategies to apply these approaches for the benefit of the industrial design process rather than delving deeply into their underlying concepts. For the interested readers, a relatively detailed explanation of MANOVA analysis is provided in Appendix B. In the present case, MANOVA is used for a preliminary test to ascertain the presence of manufacturing drift with time in the turbine blade measurements before proceeding with the PCA and FFT based analysis. Usage of the response surface modelling (RSM) techniques, specifically Kriging, in conjunction with the LP_τ design of experiments (DOE) approach is also explored for creating surrogate models in an effort to save the computational cost required for the FEA runs. These techniques, however, do not prove to be helpful for the current problem. A brief introduction to Kriging and LP_τ DOE techniques is provided for interested readers.

1.5 Layout of the Thesis

This thesis is organized as follows :

Chapter 2 explains the casting process used for manufacturing hollow turbine blades with both internal and external design features. It also gives a brief description of the various procedures used for blade inspection after casting. The information presented is based on a first-hand experience at the shop floor and has been collected from regular discussions with the design and manufacturing engineers working at the casting facility. Various possible sources of geometric variability during the manufacturing process and measurement error during the ultrasonic blade wall thickness inspection are also presented. The discussion concludes by providing an insight into the benefits that a manufacturing variability analysis may offer at the shop floor.

Chapter 3 proposes a methodology that employs probabilistic data analysis techniques of PCA and FFT analysis for de-noising measurement data in order to capture the underlying effects of manufacturing variability. It also proposes a technique for dimensionality reduction in case of PCA, and selecting the threshold magnitude (TM) for discarding Fourier coefficients in case of FFT, that uses prior information available on the measurement error. A brief historical background on the PCA and FFT techniques and an introduction to their mathematical concepts is provided. The usage of repeated measurement data for de-noising the one-off measurements available in production is discussed in detail. This is followed by the application of the proposed methodology to the turbine blade problem along with a summary of the main results.

Chapter 4 proposes a FFD based methodology for representing the 3-d geometric variability observed in turbine blade shapes from the limited number of measurements available per blade. After an introduction to the development of the FFD technique, the main mathematical concepts behind the implementation of the Sederberg and Parry FFD technique [14] are presented. This is followed by a discussion on the need for using an optimization process in conjunction with FFD to obtain the best match to the probable manufactured core shape. The objective function linking FFD with the non-linear optimization processes is formulated. Alternatives to the optimization process, namely, constrained and unconstrained LLS solution are also discussed. The results of LLS solution are compared with the shapes obtained from the optimization process and show that using non-linear optimization in conjunction with FFD results in more regularized geometries. In the end, the application of the proposed FFD based methodology is demonstrated on turbine blade core shapes resulting in representations of the 3-d geometric changes caused by manufacturing variations.

Chapter 5 discusses the application of a linear elasticity based approach for mesh morphing. A methodology is implemented that uses information obtained from the FFD analysis for generating 3-d volume meshes on the probable manufactured turbine blades in FEA ready form. The boundary conditions and mathematical formulations used for conducting turbine blade lifing analysis at maximum take-off (MTO) conditions are presented. A mesh convergence study is undertaken to estimate the appropriate mesh size for finite element analysis. This is followed by numerical studies resulting in estimating the mean life and standard deviation in life observed for the probable turbine blade shapes. The main findings of this study are summarized at the end of the chapter.

Chapter 6 makes an attempt to generate RSMs for lifing predictions using the probabilistic values of turbine blade measurements as inputs. An introduction to the LP_τ design space sampling technique is provided followed by a brief description of the Kriging approach for response surface modeling. Different techniques used for validating the RSMs including the leave-one-out cross-validation method are also discussed. Finally, the numerical studies conducted for the turbine blade problem are presented showing that creating RSMs is not very helpful in the present case.

Chapter 7 describes a robust design optimization study for turbine blades in the presence of manufacturing variability. The need for using robust design techniques in the industry when creating new designs is discussed. An overview of the state of the art in robust design methods along with a detailed explanation of the approach for robust design using multiobjective optimization is presented. This is followed by a brief introduction to the NSGA-II optimizer and a detailed description of the iSIGHT workflow used for optimization studies in the present case. A 3-d Pareto front obtained from the multiobjective optimization is analysed to select robust-optimal solutions. Trade-off studies between the mean life and standard deviation in life against the nominal turbine blade life are conducted. Results obtained from the deterministic design optimization are compared with the optimal robust solution indicating that the optimal deterministic design may not always be the best solution. Finally, the chapter concludes with a summary of the main observations from the numerical studies conducted for the present problem.

Chapter 8 concludes this thesis with a brief summary of the main observations of this research. A mention is made of the contributions of this work to the literature and probable directions for future research are outlined.

Chapter 2

Sources of Manufacturing Variability and Measurement Error in Turbine Blades

This chapter briefly outlines the procedure employed for manufacturing the turbine blades considered in this thesis. It also presents a brief discussion on the various measurement procedures used for inspecting whether the manufactured blades are within the desired tolerance limits. The discussion then moves on to explaining the need for manufacturing variability analysis from the perspective of the benefits it may offer in improving the productivity at the shop floor. Section 2.1 provides a brief introduction to the various manufacturing and measurement processes based on a first-hand experience at the shop floor. It also explains the various probable sources of manufacturing variability and measurement error in the existing manufacturing and measurement techniques, respectively. Section 2.2 deviates slightly from the objective of the thesis presented in Chapter 1 and discusses the reasons for which a manufacturing variability analysis may be beneficial for the shop floor by providing valuable feedback on the manufacturing and measurement processes being used at present.

2.1 Manufacturing and Measurement of Turbine Blades

Turbine blades, especially those with both internal and external design features, are very complicated geometries to manufacture and to measure. Not much literature is available at present

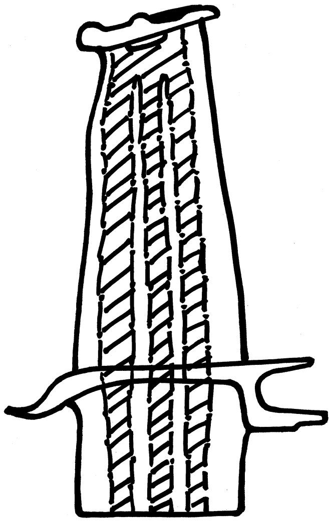

Figure 2.1: A typical turbine blade shape with internal core passages.

on the various processes used for manufacturing and measurement of turbine blades, probably due to the proprietary nature of this information. The aim of this section is to give a brief description of the processes used for manufacturing turbine blades, and discuss the various types of measurements taken for blade inspection to ensure that these blades are not defective. This is followed by a discussion in Section 2.1.1 on the probable sources of manufacturing variability introduced into the turbine blade shapes. Section 2.1.2 discusses the possible sources of measurement error that may be observed in the measurement data taken on these blades. The knowledge presented in this section is based on a first-hand experience at the shop floor where hollow turbine blades are manufactured. Regular discussions on the probable sources of manufacturing variability and measurement error have also been held with the design and manufacturing engineers at the casting facility.

The sketch of a typical turbine blade shape with internal core passages is shown in Figure 2.1. The solid lines mark the external blade surface and the dashed lines represent the core. A flowchart representation of the casting process used for manufactur-

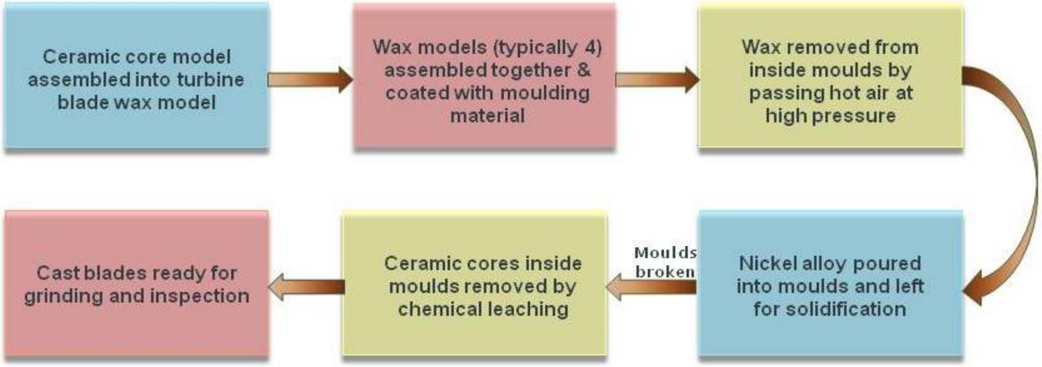

Figure 2.2: Flowchart depicting the casting process used for manufacturing hollow turbine blades.

ing hollow turbine blades is shown in Figure 2.2. Manufacturing of turbine blades involves a series of complex processes that need to be accomplished with precision in order to ensure that a majority of the manufactured blades meet the design specifications. It starts with creating the molds that are used for casting the blades. Since the blades have both internal and external design features, the preparation of molds is in itself a fairly complicated process. A separate core model is manufactured from ceramic based material for the internal passages and assembled into a wax model of the turbine blade. For this, the core models are held in dies into which molten wax is poured to create geometric representations of the desired blades. During this process, sufficient spacing is allowed for these core models to expand or drift slightly from their nominal positions so that the delicate ceramic models do not break, bend or twist when the molten wax is poured. The resultant wax models of the blades are then measured on their external surfaces using coordinate measuring machines to check if all these models meet the design requirements. This is followed by assembling a few (typically 4) wax models together and coating the molding material over these assemblies to create the final mold that will produce all these blades at one go. The wax models are fixed in the assembly with their tip at the bottom end and root at the top end. This is done to ensure the monocrystalline structure of the Nickel based alloy that is pumped later into the molds from the bottom tip end. A pictorial representation of a typical turbine blade wax model held in the mold assembly is shown in Figure 2.3.

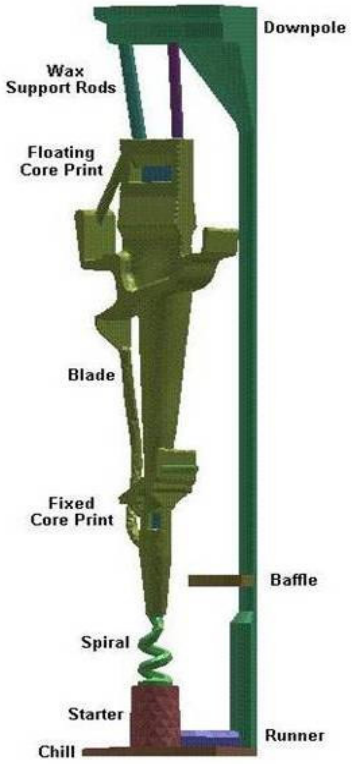

Figure 2.3: Typical turbine blade wax model held in the mold assembly. Courtesy: Rolls-Royce plc., Derby.

Once the molds are ready, air is passed through them at high temperature and pressure to melt and remove the inside wax. This results in creating hollows into which molten Nickel alloy is pumped (tip first, as stated before) and left for solidification. In Figure 2.3, the fixed core print is a direct bond between the core and shell material. The floating core print has a thin gap to allow for thermal expansion differences. At cast, the alloy is poured down the empty downpole and sent through the runners to each of the blades in the mold assembly. The alloy fills up through the starter (which also contains a filter although this is not formally modelled) and up through the blade. On completion of the solidification process, the molds are broken to take out the cast blades. These cast blades still have ceramic cores inside them which are removed by chemical leaching, a process in which the ceramic material is dissolved using suitable solvents. The cast blades so obtained are then ground to remove any irregularities on the external blade surface, e.g., moldlines, flashing, etc.

The final blades obtained after grinding are measured using different measurement procedures to check if they meet the desired design specifications. These measurements include:

- airfoil shape measurements,
- bow and twist measurements,
- blade wall thickness measurements,
- measurements for the trailing edge thickness and the blade platform thickness,
- internal passage hole measurements at the base of the blade,
- die penetration and X-ray scanning for cracks.

Coordinate measuring machines are used to plot the coordinates of the external aerofoil blade surface to compare the profiles so obtained with the nominal aerofoil profiles. If the aerofoil sections obtained are within the tolerance limits, the blades are accepted. The process of grinding is used for removing any mouldlines and flashing from the cast blades. Bending or twisting of blades is checked by measuring and comparing the coordinates of selected locations along the pressure and suction surfaces across different planes along the length of the blade. This is followed by measuring minimum blade wall thicknesses using ultrasonic measurement devices such that the location to be measured is placed perpendicular to the ultrasonic head and moved very slowly in a to and fro motion until the minimum thickness value is obtained for that particular cross-section. The thicknesses of the trailing edge and blade platform, and the positions of the holes formed by the core at the base of the blade are also measured and checked. The die penetration technique is used to investigate the presence of any external or internal cracks that are visualized using X-ray scanning machines. Thus, each and every blade that is manufactured goes through a collection of measurement procedures during the inspection process. The blades are accepted if all the measurements taken are within the specified tolerance limits or rejected otherwise. Also, if the die penetration and X-ray scanning procedures reveal any cracks, the blades are rejected.

2.1.1 Sources of Manufacturing Variability

The various sources of manufacturing variability in the casting process include :

- While creating the wax models, the ceramic cores are held relatively loosely in the dies in order to allow sufficient space for the cores to expand or deviate slightly from their base positions when the molten wax is poured. This may cause the core models to deviate to a much larger extent than expected.
- The high temperature and pressure at which air is passed through the final mold assembly for wax removal may cause the ceramic models to deflect or deform slightly from their desired shapes.
- The high temperature at which the molten metal is poured into the casts along with the hydrostatic pressure exerted by the molten metal on the core may result in the core becoming semi-plastic in nature and instigate undesirable deformations. As pointed out in Section 2.1, the floating core print shown in Figure 2.3 supports the thermal expansion differences that occur during this process.
- The ceramic core models may have air bubbles trapped inside them which may result in increasing or decreasing the blade wall thicknesses. The high temperature of the poured in molten metal may cause the air trapped inside the bubbles to expand and hence reduce the blade wall thickness values, or, the hydrostatic pressure exerted by the molten metal on the core may end up compressing these bubbles resulting in an increase in the thickness values.
- Changes in the surrounding temperature and humidity levels and wear and tear of the tools may cause manufacturing drift with time.
- The blade to blade variations caused by grinding cannot be ignored.

2.1.2 Sources of Measurement Error

This section discusses the various probable sources of error in the ultrasonic wall thickness measurement process. Other measurement processes are not discussed further since they are beyond the scope of the present work. Some of the sources of measurement error presented below may be common to all the measurement processes and others are only relevant to the ultrasonic wall thickness measurement procedure. In brief, the various sources of measurement error include :

- The blades are held by hand above the ultrasonic head while taking measurements. Non-firm clamping of the blades may cause left and right misalignments of the blade and result in inaccuracies.
- The ultrasonic measurement procedure may be considered to be slightly biased towards over thick readings because any failure to preset the blade at right angles to the probe may result in longer ultrasound paths in the sample being measured.
- The markings for the measurement locations on the blade surface are quite thick and may lead to an offset from the plane across which measurements are being recorded.
- The pressure or suction surfaces across which measurements are being taken are hidden from view of the operator, making it difficult to check if the measurements are being recorded at the correct location and on the correct plane.
- The minimum thickness values are recorded by pressing a pedal once the ultrasonic device encounters the least thickness value across a desired location. Since the same operator who holds the blade above the ultrasonic head also presses the pedal, any misalignment of the blade while pressing the pedal may result in over-thick readings.
- The ultrasonic measurement device may suffer from calibration error or may have its ultrasonic head slightly tilted from its desired upright position. Since calibration errors are an obvious source of measurement error, care is usually taken to avoid these errors.
- Last but not the least, human error is a possibility that may not be ignored.

2.2 Need for Manufacturing Variability Analysis in improving Productivity

The motivation behind conducting a manufacturing variability analysis on the turbine blades has already been presented in Chapter 1, Section 1.1. Manufacturing the turbine blades is not only a complicated process, but it is also very expensive with each blade costing around £5,000-£10,000. Therefore, the number of acceptable blades manufactured in a particular batch becomes very important. The higher the number of rejected blades coming out of the manufacturing process, the greater is the monetary loss incurred by the company. Thus, identification of the sources of manufacturing variability and possible solutions to reduce or eliminate this variability become highly desirable. Feasible modifications to the existing manufacturing processes may then be proposed in order to reduce the effects of the observed manufacturing variability. However, it is essential to be able to segregate measurement error from measurement datasets to capture the underlying effects of manufacturing variability. There is also a possibility that acceptable blades are being rejected due to measurement error. Therefore, it becomes necessary to estimate the variability in measurements caused by measurement error, identify its possible sources, and suggest any feasible improvements to the existing measurement processes.

Chapter 3

Probabilistic Measurement Data Analysis to Capture the Effects of Manufacturing Variability

This chapter proposes a methodology for filtering noise from measurement datasets in order to capture the underlying effects of manufacturing variability in terms of the manufacturing drift with time and the blade to blade manufacturing error. To begin with, a Multivariate Analysis of Variance (MANOVA) of the measurement data is conducted to ascertain the presence of manufacturing variability. This is followed by the application of probabilistic data analysis techniques, such as, Principal Component Analysis (PCA) and Discrete Fourier Transform (DFT) analysis using the Fast Fourier Transform (FFT) algorithm, for de-noising measurement data to capture the underlying effects of manufacturing variability. A technique for dimensionality reduction in case of PCA, and, selecting the threshold magnitude (TM) in the case of FFT is proposed that uses prior information available on the measurement error. Application of the proposed methodology on turbine blade data results in the probable values of actual measurements for these blades. These measurements may then be used for generating 3-d models of the turbine blade shapes for finite element analysis (FEA).

This chapter is organized as follows: In Section 3.1 we discuss the need for manufacturing variability analysis for turbine blades. Section 3.2 presents the mathematical formulations for the different probabilistic and statistical data analysis techniques implemented for the present problem. It also gives a detailed mathematical explanation of the proposed dimensionality reduction technique that uses prior information on the measurement error. This is followed by Section 3.3 that gives a detailed explanation of the proposed methodology for de-noising measurement data using the PCA and FFT techniques, and, capturing the effects of manufacturing variability in terms of the manufacturing drift with time and the blade to blade manufacturing error. Section 3.4 discusses the application of the proposed methodology to the turbine blade problem and presents the results obtained from the numerical studies. Finally, the main observations are summarized in Section 3.5.

3.1 Need for capturing Manufacturing Variability

The 'need' for conducting a probabilistic analysis to characterize and quantify manufacturing variability has been discussed in Chapters 1 and 2. In Section 1.1, we noted that the turbine blades coming out of the manufacturing process exhibit variations in shape from their designed/nominal shapes. Various factors may be contributing to these variations, e.g., slight differences in the shapes of the molds used during the casting process, changes in the surrounding temperature and humidity levels when the blades are cast, hand-finishing operations such as grinding and polishing, subjecting different blades to varying loads at the same or different positions, wear and tear of the tools, etc. The variations observed in blade shapes may in turn lead to bigger problems, such as, affecting the performance or the life of these turbine blades during operation. It becomes essential therefore, to identify and estimate manufacturing variability and observe its effects on turbine blade life and performance in operating conditions. As discussed in Section 1.2, the most obvious solution to this problem appears to be taking measurements on the blades to get some idea of the manufactured blade shapes. However, the measurement data may be clouded by measurement error, or, what is commonly known as random error or noise. Therefore, segregation of this measurement error/noise from the measurement dataset to capture the underlying manufacturing variability, and then, quantification of this manufacturing variability along with identification of its various sources is a significant task.

This chapter proposes a methodology based on existing de-noising techniques, namely PCA and FFT, for filtering out the measurement error from measured data collected on turbine blades coming out of the manufacturing process. The application of this methodology also results in segregating the manufacturing variability so obtained into manufacturing drift with time, and the blade to blade manufacturing error. The presence of manufacturing drift with time is ascertained by the usage of MANOVA on the measurement dataset. The resultant probable manufactured blade measurements may then be used for obtaining 3-d representations of the variations in turbine blade shapes as discussed further in Chapter 4.

3.2 Probabilistic Data Analysis Techniques

This section presents an overview of the mathematical aspects of PCA and FFT techniques. It also gives a detailed explanation of the proposed techniques for dimensionality reduction that use prior information on the measurement error. The usage of measurement error information for selecting the TM when using FFT for de-noising measurement dataset is also discussed. Here, TM refers to the threshold magnitude used as cut-off for discarding the Fourier coefficients.

Consider an $m \times n$ data matrix $\mathbf{X}$, where m represents the number of blades measured and n represents the number of measurements taken on each blade. This data matrix $\mathbf{X}$ can further be divided into g time-based groups, namely, $\mathbf{X}_1, \mathbf{X}_2, \mathbf{X}_3, \cdots, \mathbf{X}_g$ with dimensions $m_1 \times n, m_2 \times n, m_3 \times n, \cdots, m_g \times n$ respectively, such that, $m_1 + m_2 + m_3 + \cdots + m_g = m$. In the present case, since the dataset $\mathbf{X}$ consisted of measurements taken on turbine blades manufactured over a year, $\mathbf{X}$ was split into 12 time-based groups ($g = 12$) such that the blades manufactured within the same month were grouped together. Subsequently, MANOVA (refer Appendix B) may be applied on these groups to ascertain the presence of manufacturing drift with time. This may be followed by the application of PCA and FFT techniques on each of the g groups separately to obtain measurements capturing the effects of manufacturing drift with time.

Information on measurement error was additionally collected through a specially designed experiment in which r repeated trials of the same experiment on the same blade were conducted by l different operators. This process was repeated for q randomly selected blades. It may be noted that most of the random measurement errors have been taken into account in this experiment since the same sample was measured at different stations, by different operators, at different times of the day, and on different days. The measurement noise information can be converted into a data matrix $\mathbf{N}$, such that, each row is populated with the measurements on the same blade and location and each column contains the measurements from the same trial.

For each of the q blades, the repeated measurement data may be represented as a $n \times p$ matrix $\mathbf{N}(j)$ $(j = 1, 2, \cdots, q)$, where n is the total number of measurement locations and $p = l \times r$. For the present problem, $l = 3$ and $r = 4$, therefore $p = 12$.

3.2.1 Principal Component Analysis (PCA)

Background

PCA is a non-parametric method for extracting relevant information from complex datasets [19]. It is used for identifying patterns in data that highlight their similarities and differences, and compressing this data with minimal loss of information [20]. PCA has been used for varied applications such as face recognition in computer vision [20], gene expression analysis in bioinformatics [21], shape prediction of femoral heads from partial information in medical imaging [22], reconstruction of human body shapes from range scans in computer graphics [23], etc. In addition, PCA has proved to be particularly useful for data analysis in diverse fields like oceanography [24, 25], climatology [26], geophysics [27, 28], geology [29], astronomy [30, 31], etc. Lately, more complicated forms of PCA have been developed and demonstrated on varying sets of data. Smidl and Quinn [32] proposed Bayesian PCA and demonstrated the advantages of orthogonal variational PCA (OVPCA) on scintigraphic dynamic image sequences of kidneys. Tipping and Bishop [33] demonstrated the advantages of Probabilistic PCA (PPCA) by its application to a set of *Tobamovirus* data (a genus that contains viruses that infect plants). Hagan, Roble, Russell and Mlynczak [28] made use of Complex PCA (CPCA) on satellite data for planetary wave and tidal analysis in the middle atmosphere. The PCA technique, though very popular in many fields of research, has not found many applications in the aircraft engine manufacturing and design industry. One of the reasons may be lack of availability of measurement data on aircraft engine components which is usually kept classified by the manufacturing companies. Recently, some researchers in the aerospace research community have conducted successful research in constructing high-fidelity models of manufacturing variability using PCA, e.g., in 2003 Garzon and Darmofal [10, 7] used PCA to construct models of geometric variability suitable for probabilistic analysis and design from external surface measurements of an ensemble of compressor rotor airfoils.

“The goal of principal component analysis is to compute the most meaningful *basis* to re-express a noisy data set. The hope is that this new basis will filter out the noise and reveal hidden structure" [19]. The mathematics behind PCA and its various properties are explained in great detail in the works of Shlens [19], Jolliffe [34] and Mandel [35]. In the present work, an attempt is made to cover these mathematical formulations in a concise form. At this point, it is essential to understand the important assumptions that PCA makes while performing data analysis:

- It assumes that there exists a *basis* which is a linear combination of the original basis that can be used to express the data set.
- It assumes that the measurement dataset comprising measurements of the same measurement type/variable on different samples has a multivariate normal distribution.
- It assumes that the measurement noise in the input dataset is low as compared to the actual measurement or input signal. Thus, the principal components (PCs) with larger variances capture the dynamics of the input signal while the PCs with lower variances capture noise.
- It assumes that all the PCs are orthogonal.

Mathematical Formulations

The mathematical formulations of PCA that follow are based on the paper by Shlens [19]. As discussed before, we have a $m \times n$ data matrix $\mathbf{X}$. Now, let us assume that $\mathbf{X}_0$ is a $n \times m$ mean-centered input data matrix for PCA defined as,

$$\mathbf{X}_0 = \mathbf{X}^{\mathrm{T}} - \overline{\mathbf{X}^{\mathrm{T}}}. \tag{3.1}$$

In equation (3.1) above, $\overline{\mathbf{X}^{\mathrm{T}}}$ is a $n \times m$ data matrix in which each column is populated with the mean values of each row from $\mathbf{X}^{\mathrm{T}}$. Let $\mathbf{Y}$ be another $n \times m$ matrix related to $\mathbf{X}_0$ by a linear transformation $\mathbf{L}$, such that,

$$\mathbf{L}\mathbf{X}_0 = \mathbf{Y}. \tag{3.2}$$

The goal of PCA is to find an orthonormal matrix $\mathbf{L}$ such that the covariance matrix of $\mathbf{Y}$,

$$\mathbf{C}_{\mathbf{Y}} \equiv \frac{1}{n-1}\mathbf{Y}\mathbf{Y}^{\mathrm{T}}, \tag{3.3}$$

is diagonalized. Rewriting equation (3.3) using (3.2) we get,

$$\begin{aligned}\mathbf{C_Y} &= \frac{1}{n-1}(\mathbf{L}\mathbf{X}_0)(\mathbf{L}\mathbf{X}_0)^{\mathrm{T}},\\ &= \frac{1}{n-1}\mathbf{L}\mathbf{X}_0\mathbf{X}_0^{\mathrm{T}}\mathbf{L}^{\mathrm{T}},\\ &= \frac{1}{n-1}\mathbf{L}(\mathbf{X}_0\mathbf{X}_0^{\mathrm{T}})\mathbf{L}^{\mathrm{T}},\\ \mathbf{C_Y} &= \frac{1}{n-1}\mathbf{L}\mathbf{A}\mathbf{L}^{\mathrm{T}}. \qquad (3.4)\end{aligned}$$

In equation (3.4), $\mathbf{A} \equiv \mathbf{X}_0\mathbf{X}_0^{\mathrm{T}}$ is *symmetric* (by Theorem 1, Appendix A) and hence is diagonalized by an orthogonal matrix of its eigenvectors (by Theorem 3, Appendix A). Therefore, $\mathbf{A}$ may be represented as,

$$\mathbf{A} = \mathbf{E}\mathbf{D}\mathbf{E}^{\mathrm{T}}, \qquad (3.5)$$

where $\mathbf{D}$ is a diagonal matrix and $\mathbf{E}$ is a matrix of eigenvectors of $\mathbf{A}$ arranged as columns. Now, we select the matrix $\mathbf{L}$ such that each row of this matrix is an eigenvector of $\mathbf{X}_0\mathbf{X}_0^{\mathrm{T}}$. This implies, $\mathbf{L} \equiv \mathbf{E}^{\mathrm{T}}$. Substituting this relation into equation (3.5) it is observed that,

$$\mathbf{A} = \mathbf{L}^{\mathrm{T}}\mathbf{D}\mathbf{L}. \qquad (3.6)$$

We know that the inverse of an orthogonal matrix is its transpose, i.e. $\mathbf{L}^{-1} = \mathbf{L}^{\mathrm{T}}$ (by Theorem 2, Appendix A). Using this relation and substituting equation (3.6) into equation (3.4), we observe that $\mathbf{L}$ diagonalizes $\mathbf{C_Y}$. This is proven as follows:

$$\begin{aligned}\mathbf{C_Y} &= \frac{1}{n-1}\mathbf{L}\mathbf{A}\mathbf{L}^{\mathrm{T}},\\ &= \frac{1}{n-1}\mathbf{L}(\mathbf{L}^{\mathrm{T}}\mathbf{D}\mathbf{L})\mathbf{L}^{\mathrm{T}},\\ &= \frac{1}{n-1}(\mathbf{L}\mathbf{L}^{\mathrm{T}})\mathbf{D}(\mathbf{L}\mathbf{L}^{\mathrm{T}}),\\ &= \frac{1}{n-1}(\mathbf{L}\mathbf{L}^{-1})\mathbf{D}(\mathbf{L}\mathbf{L}^{-1}),\\ \mathbf{C_Y} &= \frac{1}{n-1}\mathbf{D}. \qquad (3.7)\end{aligned}$$

In the expression above, the off-diagonal values of the matrix $\mathbf{D}$ are zero and the diagonal values are ordered in terms of decreasing variance. Hence, the eigenvector corresponding to maximum variance represents the first PC, the eigenvector corresponding to maximum variance subject to it being orthogonal to the first PC represents the second PC, and so on. The results of PCA may be summarized as follows:

- The PCs of $\mathbf{X}_0$ or the rows of $\mathbf{L}$ are the eigenvectors of $\mathbf{X}_0\mathbf{X}_0^{\mathrm{T}}$. These eigenvectors are ordered in terms of decreasing variance.

- The i^{th} diagonal value of $\mathbf{C_Y}$ is the variance of $\mathbf{X}_0$ along its i^{th} eigenvector.

For the present problem, PCA is applied separately to each of the g different time-based groups, i.e., $\mathbf{X}_1, \mathbf{X}_2, \mathbf{X}_3, \cdots, \mathbf{X}_g$, respectively. The mean values of the reconstructed measurements obtained from each of the g groups result in g different blade shapes capturing the effects of manufacturing drift with time. Please note that each blade shape is characterized by just n measurement locations.

3.2.2 Dimensionality Reduction using Measurement Error Information

Background

Once PCA has been performed, the next issue is choosing the number of PCs to be retained that would account for most of the variation in the input dataset [34, 36]. Numerous techniques for dimensionality reduction are available in the literature. Some of these techniques are, - 1) *Cumulative Percentage of Total Variation*, 2) *Kaiser's rule*, 3) *Scree Graph* and the *Log-Eigenvalue Diagram*, 4) *Cross-Validatory Methods*, 5) *Partial Correlation*, 6) *Bayesian model selection*, 7) the *forward orthogonal search(FOS)-maximizing overall dependancy(MOD)* or the *FOS-MOD* algorithm, etc. [34, 36, 37]. Many readymade packages are also available in MATLAB which perform dimensionality reduction for a given dataset, e.g., *Correlation dimension estimator, Nearest neighbour estimator, Maximum likelihood estimator, Eigenvalue-based estimator, Packing numbers estimator, Geodesic minimum spanning tree (GMST) estimator*, etc. [38]. However, most of these techniques are useful when there is no prior knowledge of the error that needs to be filtered out of the measurement dataset. If information on the measurement error is available in advance, it is more desirable to use this knowledge for reducing the dimensionality of the given dataset. The present work proposes an approach to dimensionality reduction using measurement error information.

Mathematical Formulations

For the present case, information on the measurement error is collected from the repeated measurements which have been formulated previously as matrices $\mathbf{N}(j)$, $j = 1, 2, \cdots, q$. Thus, if each row of $\mathbf{N}$ is represented by a vector $\mathbf{n}_{ij}$, where i represents the measurement location number and j is the repeated trial number, then we have q matrices :

$$\mathbf{N}(1) = \begin{pmatrix} \mathbf{n}_{11} \\ \vdots \\ \mathbf{n}_{n1} \end{pmatrix}, \quad \cdots, \mathbf{N}(q) = \begin{pmatrix} \mathbf{n}_{1q} \\ \vdots \\ \mathbf{n}_{nq} \end{pmatrix}. \tag{3.8}$$

The variance of each row of $\mathbf{N}$ may be represented as the sum of the variance in the true value of the variable (say $\mathbf{v}_{ij}$) and the variance due to the measurement error (say $\mathbf{e}_{ij}$),

$$Var(\mathbf{n}_{ij}) = Var(\mathbf{v}_{ij}) + Var(\mathbf{e}_{ij}), \quad i = 1, ..., n, \quad j = 1, ..., q. \tag{3.9}$$

Now, the true value of the same variable for the same sample is constant, i.e. $Var(\mathbf{v}_{ij}) = 0$. Substituting this in equation (3.9), we get,

$$Var(\mathbf{n}_{ij}) = Var(\mathbf{e}_{ij}), \quad i = 1, ..., n, \quad j = 1, ..., q. \tag{3.10}$$

Assuming that the measurement error is random in nature, the variance of each row of $\mathbf{N}$ is actually the variance due to the measurement error because the value of the true measurement for the same blade at the same measurement location remains unchanged. Therefore, the variance matrices for expression (3.8) are obtained as :

$$\mathbf{var}(1) = \begin{pmatrix} Var(\mathbf{n}_{11}) \\ \vdots \\ Var(\mathbf{n}_{n1}) \end{pmatrix}, \quad \cdots, \mathbf{var}(q) = \begin{pmatrix} Var(\mathbf{n}_{1q}) \\ \vdots \\ Var(\mathbf{n}_{nq}) \end{pmatrix}, \tag{3.11}$$

where, $\mathbf{var}$(j) is the variance matrix for the j^{th} sample, $j = 1, 2, \cdots, q$. This variance data may then be consolidated into one $n \times q$ variance matrix. The mean of each row of the consolidated variance matrix would finally result in n different values, one each for the n different variables, i.e.,

$$\mathbf{VAR}_{n\times 1} = \frac{\mathbf{var}(1) + \mathbf{var}(2) + \cdots + \mathbf{var}(q-1) + \mathbf{var}(q)}{q}. \tag{3.12}$$

Now, taking the one-off measurements and performing PCA on this data, the reconstruction error may be defined as,

$$\textit{Reconstruction Error} = \textit{Original measurement} - \textit{Reconstructed measurement}. \tag{3.13}$$

Assuming that the reconstructed measurements represent the probable true measurements of the manufactured blades, the reconstruction error may then be assumed to represent the measurement error. By selecting the new dimensionality of the measurement data, such that,

Algorithm 1 Methodology for capturing Manufacturing Drift with time using PCA.

1. To start with, divide the one-off measurements comprising the data matrix $\mathbf{X}$ into g time-based groups.

2. Perform PCA on each of the g time-based groups separately.

3. For each of the time-based groups $\mathbf{X}_1, \mathbf{X}_2, \mathbf{X}_3, \cdots, \mathbf{X}_g$, increase the number of PCs from 1 to n in a stepwise manner and obtain the reconstructed measurements for all the samples comprising that group.

4. Subtract the reconstructed measurements from the original measurement data for each group to obtain the reconstruction error.

5. For each of the time-based groups, calculate the variance in the reconstruction error at each measurement location and plot the measurement error variance vs. location number plot as the number of PCs increase from 1 to n, respectively.

6. Now, calculate the mean variances **VAR** from the separated repeated measurement experiment.

7. For each of the time-based groups, plot the values in the variance matrix **VAR** vs. location number on the plot obtained in Step 5 above. This will result in g different variance plots for the g different time-based groups.

8. For each group, observe which PC number gives a reconstruction error variance plot that matches best with the threshold variance **VAR** plot. An easy way to determine this is by calculating and comparing the overall means of the threshold variances $\overline{\mathbf{VAR}}$ and the reconstruction error variances. In the end, the dimensionality for the reconstructed dataset is selected such that the difference between the overall means is minimized.

9. For each of the time-based groups, reconstruct the measurements using the reduced dimensionality as obtained from Step 8 above.

10. For each of the g groups, calculate the mean of the reconstructed measurements at each of the measurement locations to eliminate the blade to blade manufacturing variations. This will result in g different sets of n measurements, one from each group, capturing the effects of manufacturing drift with time.

the variance in the reconstruction error for each measurement is as close as possible to the mean variance values **VAR**, we are able to estimate the true measurements of the turbine blades. A stepwise algorithm for the application of PCA in conjunction with the proposed dimensionality reduction technique for capturing the effects of manufacturing drift with time is given in Algorithm 1.

3.2.3 Fast Fourier Transform (FFT) Analysis

Background

The Fast Fourier Transform (FFT) is a popular and very efficient algorithm for calculating the Discrete Fourier Transform (DFT) of a sequence of N numbers [39]. The credit for the discovery of FFT has been given to James W. Cooley and John W. Tukey in their work, "An Algorithm for the Machine Calculation of Complex Fourier Series" in the year 1965 [40]. In retrospect, it was discovered that an algorithm similar to the FFT was discovered by Carl Friedrich Gauss as early as 1805 [39]. Gauss' work however went largely unnoticed because it was published in Latin, used 'difficult to understand' notation, and used real trigonometric functions rather than complex exponentials [39]. Also, Burkhardt in 1904 and Goldstine in 1977 pointed out Gauss' algorithm and suggested its connection with FFT but their works were published in books primarily dealing with history and hence went unnoticed [39]. A contributing factor to the popularity of the Cooley-Tukey algorithm was that they discovered the FFT at the right time i.e. the advent of the computer revolution [41].

DFT is used widely for de-noising data in various fields of research, such as, acoustics [42, 43, 44], bioinformatics [45], pure and applied physics [46], image processing [47], etc. Recently, DFT has also found application to stress-strain problems in composite mechanics aiding in the modelling of elastically highly heterogeneous bodies [48]. Much research work has been devoted to developing variants of DFT which have proven to be more efficient than the simple DFT for certain problems. A modification of DFT, called the Subband DFT [49] makes use of the frequency-separation property of subsequences, eliminating the subsequences with negligible energy contribution. The Quick Fourier Transform (QFT) uses symmetric properties of the basis function to remove redundancies in the calculation of DFT [50]. Modified Discrete Fourier Transform (MDFT) is another technique developed for denoising speech signals leading to the improvement of speech communication quality [43]. Reducing the running cost of FFT computation has also been sought after by many researchers, including the IBM Thomas J. Watson Research Center [51, 52], with added research work focussing on the development of more efficient FFT algorithms [53, 54, 55, 56, 57, 58]. Not much literature is available on the usage of FFT in the aircraft industry except certain cases where in-flight data has been analysed using FFT based techniques [59, 60]. The present work proposes the application of FFT for de-noising measurement data taken on aircraft engine turbine blades during the blade inspection process. The formulations of FFT that follow are based on the book by Press, Teukolsky, Vetterling and Flannery [61].

Mathematical Formulations

"A physical process can be described either in the *time domain*, by the values of some quantity h as a function of time t, e.g., *h(t)*, or else in the *frequency domain*, where the process is specified by giving its amplitude H (generally a complex number indicating phase also) as a function of frequency *f*, that is *H(f)*, with $-\infty<f<\infty$" [61]. *Fourier transform* may be used to convert *h(t)* to *H(f)* and vice-versa since they are two different *representations* of the *same* function [61],

$$H(f) = \int_{-\infty}^{\infty} h(t)e^{2\pi \mathrm{i} f t}\mathrm{d}t, \tag{3.14}$$

$$h(t) = \int_{-\infty}^{\infty} H(f)e^{-2\pi \mathrm{i} f t}\mathrm{d}f. \tag{3.15}$$

The DFT takes a discrete signal in the time domain and transforms that signal into its discrete frequency domain representation [62]. The mathematical formulations of DFT and the various existing FFT algorithms have been explained in great detail in the literature [41, 61]. Let Δt denote the sampling time interval between N consecutive sampled values

$$h_\phi \equiv h(t_\phi), \quad t_\phi \equiv \phi\Delta t, \quad \phi = 0, 1, 2, \cdots, N-1. \tag{3.16}$$

With N numbers of input, N independent numbers of output are produced. According to the DFT technique, the estimates of the Fourier transform *H(f)* are sought only at the discrete values,

$$f_\psi \equiv \frac{\psi}{N\Delta t}, \quad \psi = -\frac{N}{2}, \cdots, \frac{N}{2}. \tag{3.17}$$

Approximating the integral in (3.14) by a discrete sum using equations (3.16) and (3.17), we get,

$$H(f_\psi) = \int_{-\infty}^{\infty} h(t)e^{2\pi \mathrm{i} f_\psi t}\mathrm{d}t \approx \sum_{\phi=0}^{N-1} h_\phi e^{2\pi \mathrm{i} f_\psi t_\phi}\Delta t = \Delta t \sum_{\phi=0}^{N-1} h_\phi e^{2\pi \mathrm{i}\phi\psi/N}. \tag{3.18}$$

The equation (3.18) above is called the *discrete Fourier transform* of the N points h_ϕ and can also be represented as,

$$H_\psi \equiv \sum_{\phi=0}^{N-1} h_\phi e^{2\pi \mathrm{i}\phi\psi/N}, \tag{3.19}$$

where, $H(f_\psi) = \Delta t H_\psi$. The formula for the discrete *inverse* Fourier transform, which recovers the set of h_ϕ's exactly from H_ψ's is:

$$h_\phi = \frac{1}{N}\sum_{\psi=0}^{N-1} H_\psi e^{-2\pi \mathrm{i}\phi\psi/N}. \tag{3.20}$$

From equations (3.19) and (3.20), we observe that the routine for calculating discrete Fourier transforms can also be used for calculating the inverse transforms with slight modification, the only differences being:

- change of sign in the exponential, and
- division of the expression by N.

"The FFT operates by decomposing an N point time domain signal into N time domain signals each composed of a single point. The second step is to calculate the N frequency spectra corresponding to these N time domain signals. Lastly, the N spectra are synthesized into a single frequency spectrum" [41]. It can be observed from equation (3.19) that the discrete Fourier transform requires $O(N^2)$ computations. However, the *fast Fourier transform (FFT)* algorithm helps to compute the DFT in $O(Nlog_2N)$ operations. Assuming, $W \equiv e^{2\pi \mathrm{i}/N}$, the DFT of length N can be rewritten as the sum of two DFTs, each of length $N/2$ as follows:

$$\begin{aligned}
F_\phi &= \sum_{j=0}^{N-1} e^{2\pi \mathrm{i} j\phi/N} f_j, \\
&= \sum_{j=0}^{N/2-1} e^{2\pi \mathrm{i}\phi(2j)/N} f_{2j} + \sum_{j=0}^{N/2-1} e^{2\pi \mathrm{i}\phi(2j+1)/N} f_{2j+1}, \\
&= \sum_{j=0}^{N/2-1} e^{2\pi \mathrm{i}\phi j/(N/2)} f_{2j} + W^\phi \sum_{j=0}^{N/2-1} e^{2\pi \mathrm{i}\phi j/(N/2)} f_{2j+1}, \\
&= F^e_\phi + W^\phi F^o_\phi.
\end{aligned} \tag{3.21}$$

In equation (3.21), we may observe that:

- F^e_ϕ denotes the ϕ^{th} component of the Fourier transform of length $N/2$ formed from the even components of the original f_j's,

- F_ϕ^o denotes the ϕ^{th} component of the Fourier transform of length $N/2$ formed from the odd components of the original f_j's,
- ϕ varies from 0 to N, not just 0 to $N/2$ [61].

In order to perform FFT on the turbine blade measurement data, measurements taken on the different blades in each group, i.e., $\mathbf{X}_1, \mathbf{X}_2, \mathbf{X}_3, \cdots, \mathbf{X}_g$ respectively, are sorted according to the time of their manufacture. For example, lets assume that i represents the row number and j represents the column number of any data matrix, say $\mathbf{X}_1$. Now $i = 1, 2, \cdots, m_1$ and $j = 1, 2, \cdots, n$. Representing $\mathbf{X}_1$ in matrix form,

$$\mathbf{X}_1 = \begin{pmatrix} x_{1;1,1} & x_{1;1,2} & x_{1;1,3} & \cdots & x_{1;1,n} \\ x_{1;2,1} & x_{1;2,2} & x_{1;2,3} & \cdots & x_{1;2,n} \\ \vdots & \vdots & \vdots & \cdots & \vdots \\ x_{1;m_1,1} & x_{1;m_1,2} & x_{1;m_1,3} & \cdots & x_{1;m_1,n} \end{pmatrix}. \tag{3.22}$$

Data in this matrix is ordered such that the measurements on the blade manufactured at time t_1 are placed in row 1, the measurements on the blade manufactured at time t_2 are placed in row 2 and so on for time $t_1 < t_2$. This data is then populated into a new matrix, $\mathbf{X}_{F1}$ of size $m_1 * n \times 1$ as represented below,

$$\mathbf{X}_{F1} = \begin{pmatrix} x_{1;1,1} & x_{1;1,2} & x_{1;1,3} & \cdots & x_{1;m_1,n-2} & x_{1;m_1,n-1} & x_{1;m_1,n} \end{pmatrix}. \tag{3.23}$$

A FFT is then executed on the data matrix $\mathbf{X}_{F1}$ and also on the re-ordered matrices obtained from the other groups, i.e., $\mathbf{X}_{F2}, \mathbf{X}_{F3}, \mathbf{X}_{F4}, \cdots, \mathbf{X}_{Fg}$. The threshold thicknesses for selecting the value of TM are obtained by taking the means of the repeated measurements available in matrices $\mathbf{N}(1), \cdots, \mathbf{N}(q)$. The value of TM is selected such that the best match to the threshold thicknesses is obtained. Here, TM refers to the absolute value used as cut-off for discarding the Fourier coefficients. This is graphically illustarted in Figure 3.1. As seen in the figure, selecting a value of TM = 22 results in discarding all the Fourier coefficients that have a magnitude less than 22. In the example shown in Figure 3.1, only five Fourier coefficients are retained. For the present case, this procedure of selecting the TM is repeated until the best match to the threshold thicknesses is obtained. Once an appropriate value of TM is selected, the retained Fourier coefficients are used to reconstruct the probable thickness values. The reconstructed thicknesses obtained from the inverse FFT analysis of each of the g groups capture the effects of manufacturing drift with time. The proposed application of this technique is demonstrated further in Section 3.4.

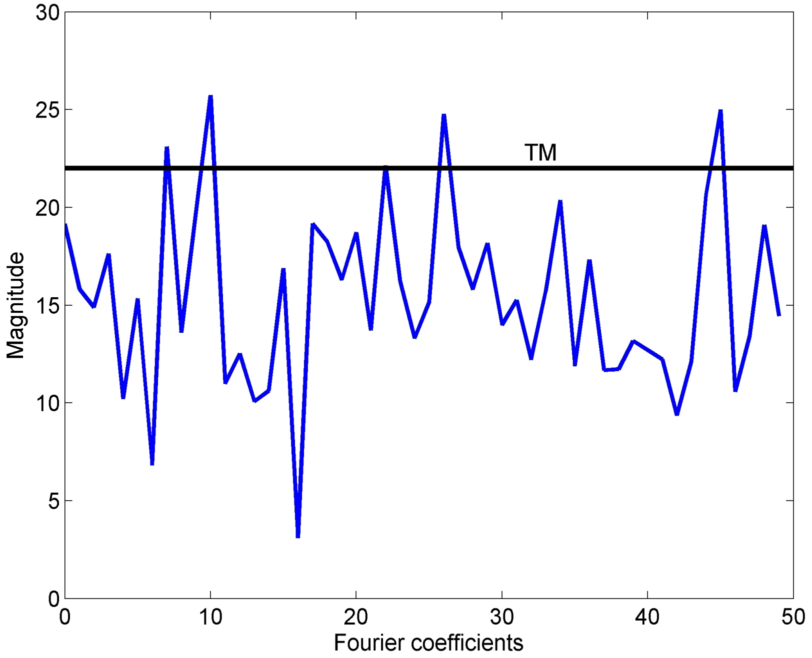

Figure 3.1: Graphical illustration of the selection of Fourier coefficients using TM.

3.3 Methodology for capturing Manufacturing Variability from Measurement Data

This section discusses in detail the proposed methodology for filtering out the measurement error from measurement data, and estimating the underlying manufacturing variability in terms of the manufacturing drift with time and the blade to blade manufacturing error. By manufacturing drift with time, we are referring to the drift in the manufactured blade shapes that may be observed with the passage of time. This may be caused due to the wear and tear of the tools employed during the manufacturing process, changes in the surrounding temperature and humidity levels, etc. The blade to blade manufacturing error refers to the inherent variations in the manufacturing process that may lead to subtle geometric differences between two or more blades manufactured at the same time. Some of the causes of blade to blade manufacturing error could be :

- Subjecting two or more blades to slightly different manufacturing loads at the same location.
- Subjecting two or more blades to the same manufacturing load at slightly different locations.

- Subtle differences in the shapes of the molds used for casting, etc.

The proposed methodology should not only be able to detect any sudden or abrupt changes in the manufacturing process, but also mark out subtle changes in the blade shapes observed with respect to time. A flowchart representation of the methodology is shown in Fig. 3.2.

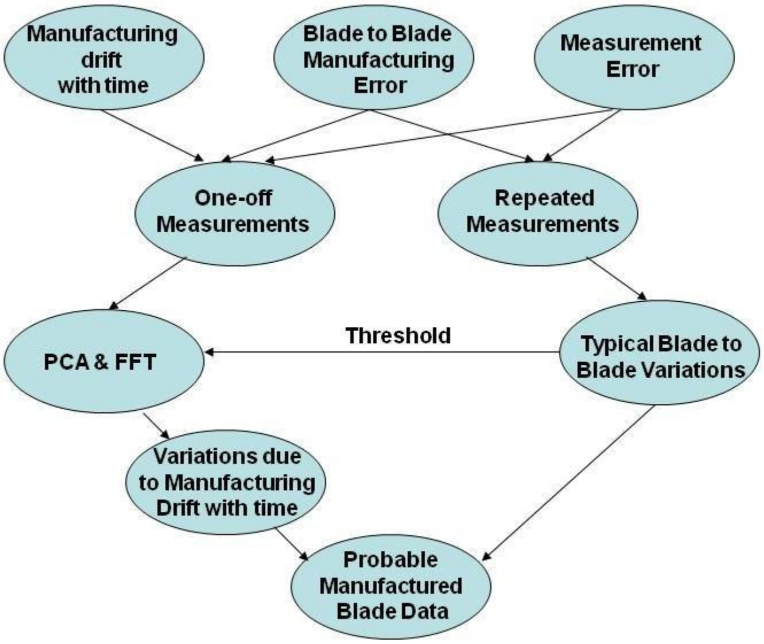

Figure 3.2: Flowchart representation of the methodology proposed for filtering out the measurement error from measurement data to capture the effects of manufacturing variability.

The one-off measurements shown in Figure 3.2 are taken on the turbine blades manufactured over a span of one year. Hence, these measurements are influenced by manufacturing drift with time, blade to blade manufacturing error and measurement error. However, the repeated measurements are taken on blades manufactured within a week. Therefore, these measurements contain negligible effects of the manufacturing drift with time and are majorly influenced by the blade to blade manufacturing error and the measurement error. Measurement error, as we know, is inevitable in any measurement procedure.

Assuming that the measurement error is random in nature, the mean of the p repeated measurements on each of the q selected blades helps nullify any random error and result in q sets of measurements capturing the effects of blade to blade manufacturing error. This information on the blade to blade manufacturing error, when used as the threshold for cut-off while executing PCA and FFT (as already explained in Section 3.2), helps in eliminating the measurement error from the original measurement data. Taking the mean of the reconstructed measurements obtained from the application of PCA and FFT on each of the g different time-based groups may further help in eliminating the blade to blade manufacturing error and result in measurements capturing the effects of manufacturing drift with time.

The application of the methodology depicted in Figure 3.2 above results in q samples from the repeated measurements capturing the blade to blade manufacturing error, and g samples each from the application of PCA and FFT on the one-off measurements capturing the effects of manufacturing drift with time. So, in total we have $q+2g$ sets of blade measurements capturing the cumulative effects of manufacturing variability. In some cases, however, FFT may result in more than g samples when more than one value of TM satisfies the threshold criterion. The application of the proposed methodology to the turbine blade problem is presented in detail in the next section.

3.4 Capture of Manufacturing Variability in Turbine Blades

Ultrasonic minimum wall thickness measurements were available on 1050 hollow turbine blades manufactured over a span of one year. These measurements were taken during the blade inspection process after casting. Since the blades were hollow, they demonstrated both external and internal design features. The measurements were taken such that the thicknesses were measured across three cross-sections, - Tip (plane located close to the tip of the curved blade surface), Mid (middle of the curved surface), and Root (plane located close to the root of the curved blade surface). The three measurement cross-sections are marked in Figure 3.3(a) which shows a typical CAD generated turbine blade model. Minimum wall thicknesses were measured at six locations across each cross-section, - 1) pressure side leading edge (PS-LE), 2) pressure side center (PS-CE), 3) pressure side trailing edge (PS-TE), 4) suction side trailing edge (SS-TE), 5) suction side center (SS-CE), and, 6) suction side leading edge (SS-LE). The cross-sectional locations of the six measurement positions are labelled in Figure 3.3(b) and also numbered from 1-6. Therefore, the measurement process resulted in a total of $n = 3 \times 6 = 18$ measurements per blade for the $m = 1050$ blades. These measurements were consolidated into a 1050×18 data matrix $\mathbf{X}$, such that going by the numbering order shown in Figure 3.3(b), columns 1-6 consisted of measurements taken at the Tip section, columns 7-12 contained measurements taken at the Mid section, and columns 13-18 consisted of measurements taken

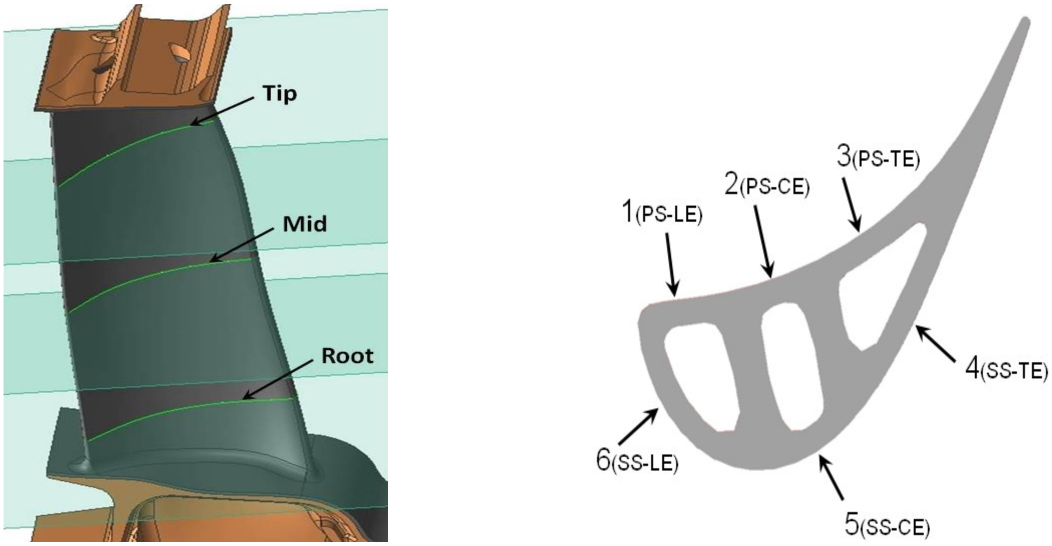

(a) (b)

Figure 3.3: (a) Typical model of a turbine blade showing three cross-sections of measurement. (b) Measurement locations across typical cross-section.

at the Root section. We shall follow the same scheme for numbering the measurement locations from 1 to 18 throughout the discussion in this chapter.

Another set of repeated measurements were taken as part of a specially designed experiment where $q = 11$ randomly selected blades were measured repeatedly at the 18 locations by $l = 3$ operators, $r = 4$ times each. This resulted in $p = 12$ repeated sets of 18 measurements on each of the 11 blades. Data on each of these blades was consolidated in the form of matrices $\mathbf{N}(j)$ $(j = 1, 2, \cdots, 11)$, as stated before in Section 3.2. Since the 11 blades selected for this experiment were all manufactured within the same week, these measurements contained negligible effects of manufacturing drift with time. The measurements were taken by different operators, at different measurement stations, on different days and at different times of the same day accounting for most of the random errors.

First of all, the one-off measurements were grouped according to the time of manufacture of the blades on which these measurements were taken, resulting in $g = 12$ time-based groups. Then, a MANOVA was conducted on these groups to observe if there were any marked differences in measurements with passage of time. A mathematical description of MANOVA is given in Appendix B. A scatter plot of $C1$ vs. $C2$ and a dendrogram plot of distance between the g group means vs. group number obtained from MANOVA is shown in Figure 3.4. $C1$

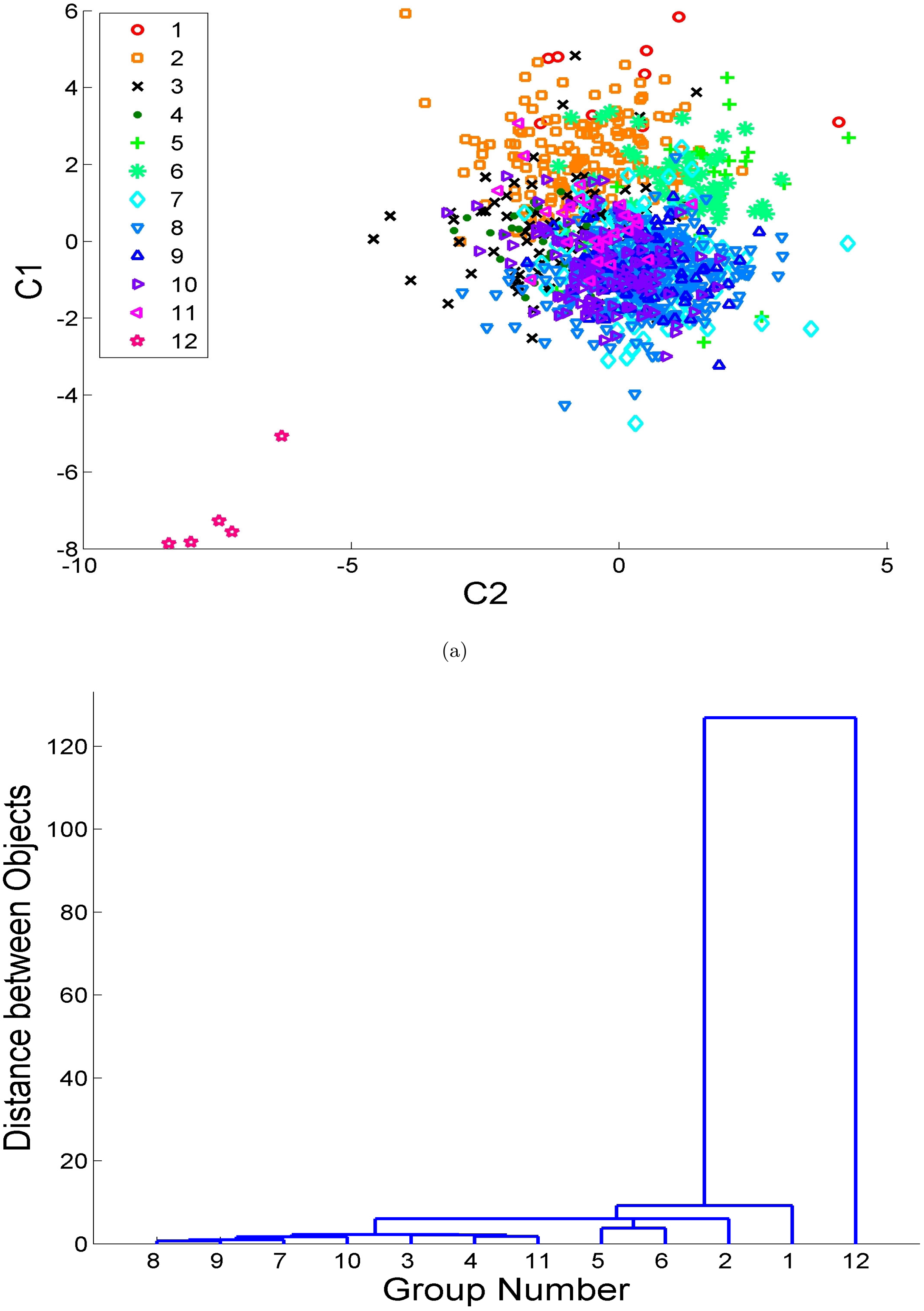

(a)

(b)

Figure 3.4: (a) Scatter plot, and (b) Dendrogram plot, obtained from MANOVA of the 12 time-based groups.

is the linear combination of the columns of $\mathbf{X}$ that represents the maximum separation between the grouped datasets and $C2$ represents the maximum separation subject to it being orthogonal to $C1$. Therefore, a scatter plot of $C1$ vs. $C2$ or a dendrogram plot of the group means after a MANOVA analysis may help in determining any noticeable differences between the measurements contained in each of the time-based groups (refer Appendix B). A scatter plot of the 12 time-based groups is shown in Figure 3.4(a) and a dendrogram plot is shown in Figure 3.4(b). The y-axis in the dendrogram plot is a measure of the differences between each of the measurement groups. The groups that are closest to each other are connected along the x-axis. Observing Figure 3.4, it becomes clear that while measurements in group 12 are markedly different from the remaining measurement data, groups 1-11 show more subtle differences between each other. The major differences between group 12 and the remaining groups were caused by the introduction of new airfoil blocks in the manufacturing process before the blades comprising group 12 were manufactured. Although this replacement of airfoil blocks is a part of the standard process adherence to counter manufacturing drift with time, it resulted in a reduction of around 17% in thickness values for all those blades that were manufactured immediately after this change. A point to be noted here is that even though the thicknesses were reduced by 17%, we are talking in terms of fractions of a millimeter (mm), hence the delta deviations in thickness values were very small in magnitude. The subtle drift in thickness values of blades comprising groups 1-11 indicates the presence of manufacturing drift with time.

This was followed by the application of PCA and dimensionality reduction techniques on each of the 12 time-based groups. As discussed before in Section 3.2.2, the mean variance values, **VAR**, were used as the threshold for cut-off while selecting the number of PCs to be retained for de-noising the measurement data. A plot of the **VAR** values vs. measurement location for the present dataset is shown in Figure 3.5. It may be observed in Figure 3.5 that the mean variance is maximum at positions 11, 12 and 13 which denote the Mid SS-CE, the Mid SS-LE and the Root PS-LE. This may arise due to the large curvature of the blade surface at these locations. It can also be observed that the measurement variability at the Tip and Root sections is lower as compared to the Mid section. A possible reason for this could be difficulty in holding the Mid section perpendicular to the ultrasonic beam head due to non-firm hold on the blade in this region. The Tip section is closer to the shroud, and the Root section is closer to the blade platform and firtree, allowing a relatively firmer hold by the operators at these cross-sections.

However, there are greater chances of left and right misalignments of the blade from the measurement markings at the Mid section. Also, an important observation in the threshold variance values was that the magnitude of the actual wall thickness measurements was approximately 10-20 times that of the maximum value of standard deviation calculated from these variances. This observation implies that the measurement variability affecting the measurement datasets is small as compared to the thickness values, and may indicate that the operators are well trained. The magnitude of variances is not shown in Figure 3.5 due to proprietary issues.

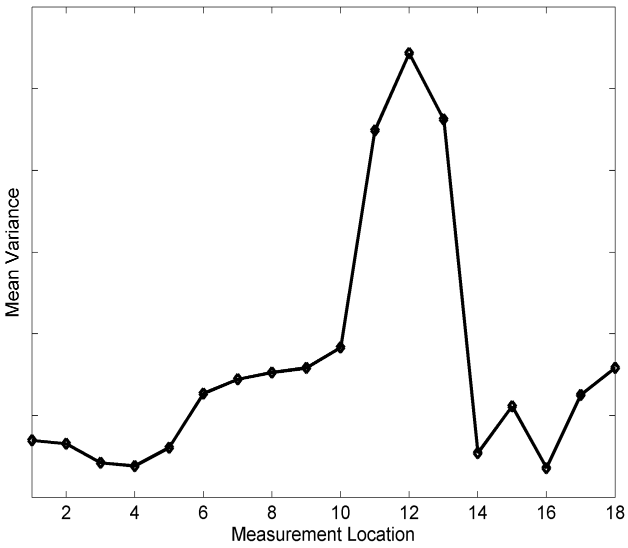

Figure 3.5: Plot of threshold variance values **VAR** vs. measurement location obtained from repeated measurement dataset.

Following Algorithm 1 given in Section 3.2.2, the variance plots for each of the 12 one-off measurement groups were plotted to calculate the new dimensionality for each of these groups separately. As an example, the variance plot obtained for group 3 is shown in Figure 3.6. The figure shows the plot of the threshold variance, **VAR**, for each of the 18 measurement locations. The overall mean of all these 18 variances, $\overline{\mathbf{VAR}}$, is also plotted as a staight line parallel to the x-axis. Similarly, the variances in reconstruction error for each measurement location and the overall mean variance as the number of PCs increases from 1 to 3 have also been plotted. It may be noted that a PCA on each of the 12 groups actually results in $n = 18$ PCs for each group. However, comparison of only the first 3 PCs has been depicted in Figure 3.6 for ease of visualization. In Figure 3.6, PC = 1 implies that only the first PC has been used for reconstructing the de-noised thickness values. PC = 2 implies that the first two PCs have been used, and PC = 3 implies that the first three PCs have been used to reconstruct the measurements. According to equation (3.13), reconstruction error is the difference between the original measurements and the reconstructed measurements. As already discussed in Section 3.2.2, our aim is to reduce the dimensionality of the measurement

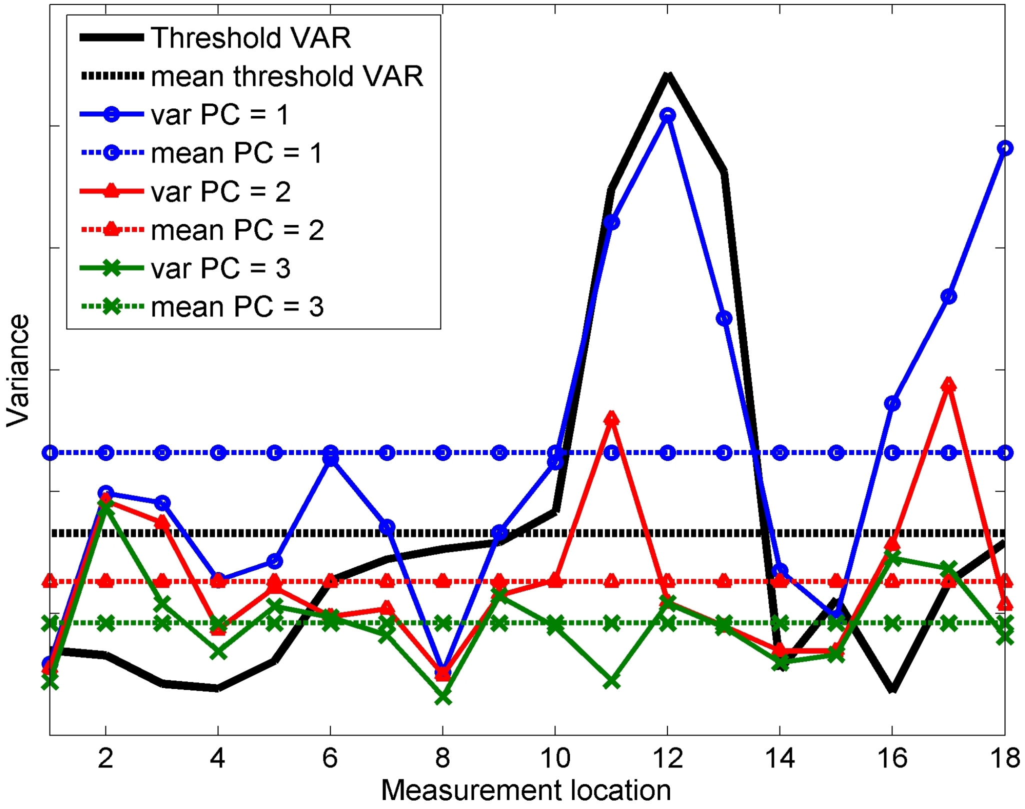

Figure 3.6: Variance plot for dimensionality reduction using PCA on the measurement data.

data such that the variances in the reconstruction error are as close as possible to the threshold variances, **VAR**. On observing Figure 3.6, it may appear that the variances for PC $= 1$ are closer to the threshold variances. However, a comparison of the overall mean variance plots indicates that PC $= 2$ results in minimizing the differences between the reconstruction error variances and the threshold variances. Therefore, the selected dimensionality for group 3 is PC $= 2$. This means that for group 3, the measurements reconstructed using the first two PCs capture the probable effects of manufacturing variability. These reconstructed measurements contain the effects of both, manufacturing drift with time, and the blade to blade manufacturing error. Taking means of reconstructed measurements at each measurement location for all the blades comprising group 3 may, however, filter out the effects of blade to blade manufacturing error and only capture the effects of manufacturing drift with time. Similarly, PCA and dimensionality reduction can be performed on each of the 11 remaining time-based groups to finally result in 11 more mean measurement sets, one from each group. In the end, we have $g = 12$ mean measurements sets capturing the effects of manufacturing drift with time.

Ideally, one would prefer to validate the results obtained from PCA with the true thickness values. One way of measuring the true thicknesses would be taking computed tomography (CT) scans on the turbine blades. However, this process needs highly powered X-ray CT scanners for the high density nickel alloy blades which are not readily available. Moreover, CT scanning contributes significant scanning errors which need to be filtered out from the scanned data before these measurements can be trusted to represent the true thicknesses. This again brings us back to the problem we are trying to solve using probabilistic techniques. Another method of obtaining the true thicknesses would be slicing up the sample blades and taking measurements on these slices. Not only is this cumbersome due to the lack of blades available for cutting up, but also because of the difficulty in registering and measuring the measurement locations for comparison. Therefore, it was considered appropriate to use an alternative de-noising technique, i.e. FFT, on the same two measurement datasets and compare the results obtained from FFT analysis with those obtained from PCA. FFT is a technique that is based on completely different fundamentals as compared to PCA, but, both these techniques can be used for the same objective of de-noising measurement data to reveal the underlying trends in the estimates of actual measurements. This may also aid in the manufacturing variability analysis by providing additional measurements capturing the effects of manufacturing drift with time.

Like PCA, FFT analysis was also performed separately on each of the 12 time-based groups. The application of FFT analysis on the blades comprising group 12 is demonstrated in Figure 3.7. Figure 3.7(a) shows the mean of threshold thicknesses and measured thicknesses plotted in a time domain. Converting into the frequency domain, a FFT analysis is executed on the measurement data to calculate the DFT of the noisy measurements. The value of TM is increased in a step-wise manner and all the Fourier coefficients with absolute value less than TM are discarded. The inverse FFT of this de-noised data reconstructs the probable values of manufactured thicknesses. Figures 3.7(b), 3.7(c) and 3.7(d) show the reconstructed thicknesses for TM = 4, TM = 6 and TM = 10, respectively. The final value of TM is selected such that the reconstructed thicknesses match best with the threshold thicknesses. In Figure 3.7, TM = 4 appears to be the best choice. Similarly, measurement data in each of the other 11 groups was de-noised to result in 19 sets of reconstructed thicknesses capturing the effects of manufacturing drift with time. One may wonder that why FFT resulted in 19 sets of reconstructed measurements while PCA resulted only in 12. This is because, for some of the

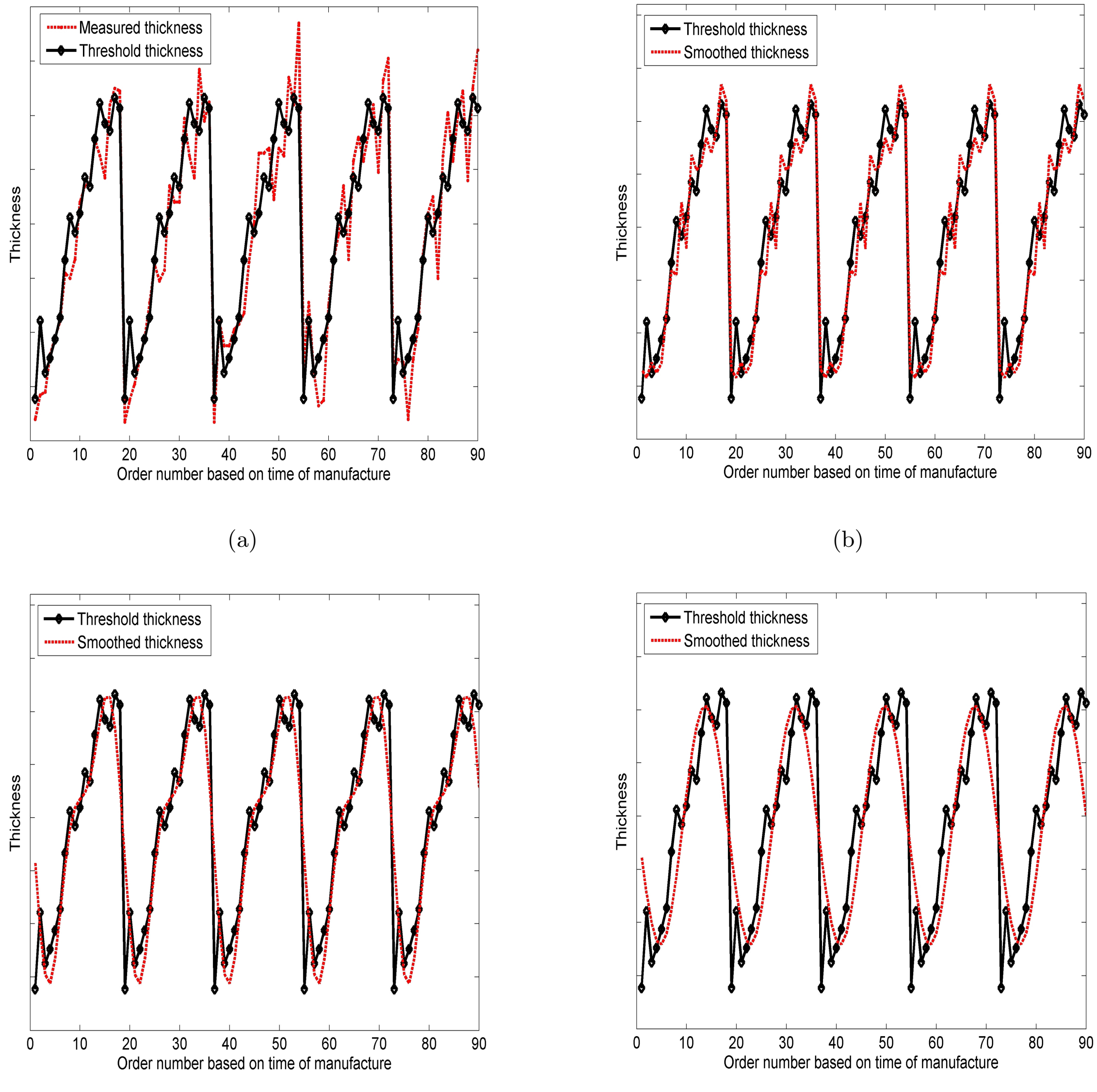

(a) (b)

(c) (d)

Figure 3.7: (a) Measurements ordered according to the time of blade manufacture. (b) Smoothed measurement data when TM = 4. (c) Smoothed measurement data when TM = 6. (d) Smoothed measurement data when TM = 10.

groups more than one values of TM satisfied the threshold criterion.

A comparison of the results obtained from the PCA and FFT analysis is shown in Figure 3.8 on the same scale. As we can observe, the reconstructed thicknesses obtained from both PCA and FFT analysis possess similar patterns and their values when compared with the nominal and mean threshold thicknesses suggest that our results are reasonably correct. The

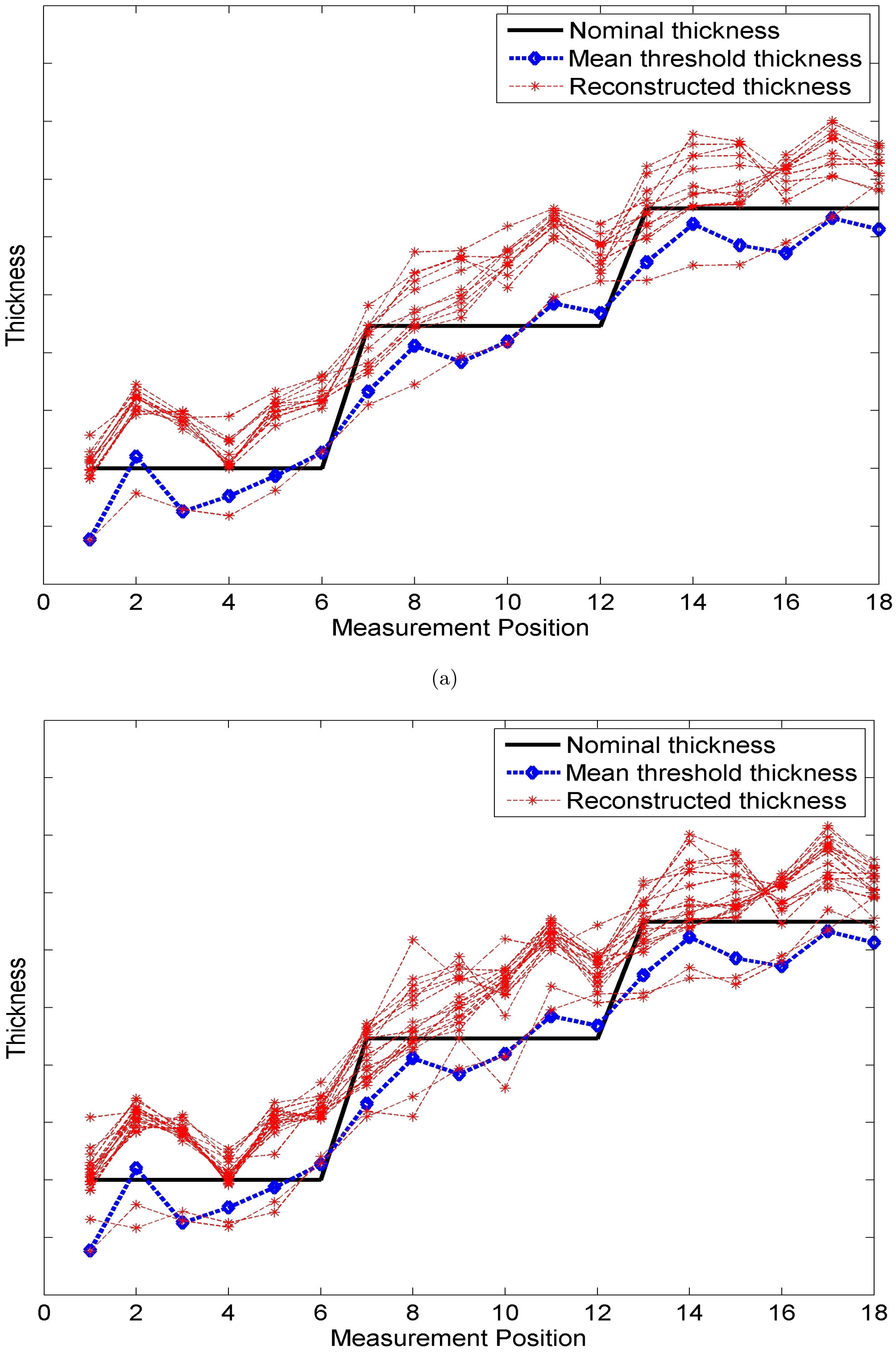

(a)

(b)

Figure 3.8: Results obtained from (a) PCA analysis, and (b) FFT analysis, compared with the mean of threshold thicknesses and nominal thicknesses.

reconstructed thicknesses closest to the mean threshold thickness values in both the plots are obtained from group 12. This is because the 11 blades on which repeated measurements were taken and the blades in group 12 were all manufactured shortly after the introduction of new airfoil blocks. It can be seen that the reconstructed thicknesses obtained from groups 1-11 are on an average 17% thicker than the threshold thicknesses. This confirms that despite the different times of manufacture of the blades, the threshold criteria for both PCA and FFT techniques is sufficient to capture the effects of manufacturing drift with time. As discussed before in Section 3.3, the threshold thicknesses used for the FFT analysis are actually the means of the repeated measurements taken on the 11 blades. These thicknesses capture the effects of the blade to blade manufacturing variation. Thus, in the end we have $11 + 12 + 19 = 42$ sets of reconstructed measurements capturing the effects of manufacturing drift with time and blade to blade manufacturing error. These measurements may now be used for generating 3-d representations of the probable manufactured turbine blade shapes for FE analysis.

3.5 Summary

In this chapter, a methodology based on well-established de-noising techniques, i.e., PCA and FFT, was proposed for segregating measurement error from the measurement dataset to reveal the underlying manufacturing variability. Application of the proposed methodology helped in segregating the effects of manufacturing variability into manufacturing drift with time and the blade to blade manufacturing error. A technique that makes use of prior information on measurement error was proposed and implemented for dimensionality reduction in case of PCA, and selecting the TM for FFT analysis. The variance plot obtained from the repeated measurements while using this approach may also provide some extra information on the sources and magnitude of measurement error. For example, for the present problem of analysing hollow turbine blade data, it was observed that :

- The magnitude of measurement variability is maximum at the Mid section suction side center, Mid section suction side LE, and Root section pressure side LE positions, possibly due to the large curvature at these locations.
- Measurement variability is lower at the Tip and Root sections as compared to the Mid section. A relatively firmer hold on the blade at the Tip and Root sections due to the presence of shroud and firtree could possibly account for this difference. It may be

possible that there is a larger left and right misalignment of the blade at the Mid section when it is held perpendicular to the ultrasonic head.

- The magnitude of the variance due to measurement variability is relatively small as compared to the magnitude of the wall thickness measurements. The thickness values are 10-20 times greater than the maximum value of standard deviation observed in the repeated measurements. This may indicate that the human error is relatively very small and the operators are well trained.

Application of MANOVA on the time-based grouped datasets was not only able to capture the sudden and abrupt changes in the manufacturing process, it also captured the subtle differences in turbine blade measurements due to manufacturing drift with time. Analysis using the proposed methodology resulted in a sample of 42 probable manufactured blade measurements, 31 of which captured the effects of manufacturing drift with time, and the remaining 11 captured the blade to blade manufacturing variations. These measurements may now be used for generating 3-d representations of probable manufactured turbine blade shapes for lifing, stress and thermal analysis.

Chapter 4

3-d Geometry Manipulation using Limited Measurements

This chapter proposes a methodology based on the application of the Free-Form Deformation (FFD) approach in conjunction with optimization, or alternatively, linear least-squares solution, to obtain deformed geometries of the turbine blade core models from the limited number of available measurements. These deformed core models are representative of the probable turbine blade core shapes coming out of the manufacturing process that are affected by manufacturing variability. The chapter is organized as follows: In Section 4.1, the need for approximating the deformations along the entire blade surface using limited number of measurements is discussed. This is followed by Section 4.2 which provides a brief background on FFD and discusses its mathematical formulations. Section 4.3 discusses the need for using an optimization process in conjunction with FFD and formulates the objective function. Section 4.4 presents the formulations for minimizing the value of this objective function using non-linear optimization. Following this, Section 4.5 discusses the constrained and unconstrained forms of the linear least-squares solution approach that may be used as an alternative to the optimization process. Finally, Section 4.7 presents the numerical studies conducted on the turbine blade problem and Section 4.8 summarizes the results obtained from these studies.

4.1 Need for 3-d Geometry Manipulation

In Chapter 3, we presented a methodology for de-noising factory measurement datasets to obtain estimates of the true measurements for the turbine blades. It is then desirable to be able to use these measurements for generating 3-d geometric representations for the probable turbine blade shapes. The manual generation of a new model in a CAD tool for each and every blade shape is not desirable since this process will be time consuming and would require significant manual intervention. This leads to the need for automatically morphing the base/nominal geometry in order to generate 3-d models representing the different blade shapes being manufactured. Due to the limited number of measurements available per blade, it is very difficult to characterize the complete geometric variability along the entire length of the blade. It becomes essential therefore to use geometry manipulation techniques, e.g. Free-Form Deformation (FFD), that enable the use of a limited number of measurements to approximate the deformations on the entire blade surface according to the flexibility decided by the user. However, the process of identifying the best match to the expected blade shape cannot be executed without a process to optimize the match between desired and actual shapes working in conjunction with FFD.

In this study, the primary focus is on deforming the shape of the blade core passages. A rough sketch of this core is given in Chapter 2, Figure 2.1. In a separate study conducted on the external blade airfoil measurements, it was found that manufacturing variability has negligible influence on the external airfoil shapes and the brunt of its effects is borne by the internal core shape. Further details on this study will be presented in Section 4.6. Therefore, it was considered appropriate to fix the external shape of the nominal turbine blade model, and deform the base core in order to characterize the 3-d geometric variability. This chapter proposes the application of the Sederberg and Parry FFD technique [14] for deforming a nominal core surface mesh using the turbine blade measurement data obtained from the studies conducted in Chapter 3. The deformations are implemented such that they are neither too global nor too local in nature. The best match to the expected core shape is obtained by using an optimization process in conjunction with the FFD approach. The deformed core surface meshes obtained from this analysis may then be used for generating 3-d volume meshes on the probable turbine blade shapes for FEA.

4.2 Free-Form Deformation (FFD)

4.2.1 Background

Free-Form Deformation (FFD) is a very popular geometric deformation technique that allows the user to conceptually embed an object, or several objects, in a parallelepiped of clear, flexible plastic, and apply deformations to the plastic such that the embedded object is deformed in a manner that is intuitively consistent with the motion of the plastic [14, 63, 64]. This clear, flexible plastic is more commonly called the *lattice* of control points that enclose the object to be deformed. FFD was first introduced by Sederberg and Parry in 1986 [14]. Sederberg and Parry define the lattice as a trivariate tensor product of Bernstein polynomials such that the control points are actually the coefficients of the polynomials. Changes in positions of these control points deform the object embedded inside the lattice. Further advances to the FFD technique were proposed by Coquillart in 1990, introducing an extension of the FFD technique called Extended Free-Form Deformation (EFFD) [65]. This method uses arbitrarily shaped lattices, enabling better control of the enclosed object for local deformations. The idea of having better control of the object for local deformations was developed further by Hsu, Hughes and Kaufman in 1992, who proposed a direct manipulation of free-form deformations such that a point on an object may be selected by using a pointer and moved directly to the desired location [66]. A very useful implementation of Directly Manipulated Free-Form Deformation (DMFFD) is demonstrated by Frisch and Ertl [67] who have applied this technique for local deformations in car crash simulations to perform finite element calculation. In 1994, Lamousin and Waggenspack [64] introduced a Non-uniform Rational B-Splines (NURBS) based FFD technique, sometimes also called the NFFD technique. NFFD enables the division of the lattice associated with the object into an arbitrary number of non-uniform sections as opposed to Sederberg's and Parry's FFD which requires that the divisions are uniform in nature. Further to this, Noble and Clapworthy [68] demonstrated the use of NFFD for direct manipulation of surfaces such that NFFD weights were used to add local details/deformations. The use of FFD has not been limited to static objects, but has been extended further for animation synthesis in the form of *dynamic FFD* [69] in which control points evolve automatically through time in accordance with mechanical principles, enabling smooth animated movements.

Although, most of the FFD related work available in the literature is focused on gaining better control of the deformations using direct manipulation or NURBS-based FFD techniques etc., a recent work by Singh and Kokkevis [70] proposes the use of surface-oriented FFD for skinning animated characters such that the space deformed by the lattice is not the volume enclosed by the control points, but is based on a distance metric from the surface defined by the control point structure. FFD techniques have also found wide applications in aerodynamic shape parameterization and optimization problems [71, 72, 73, 74], however, its use for characterizing geometric variability from the limited number of available measurements, especially in the aircraft engine manufacturing industry, remains relatively unexplored. The present work proposes the application of the Sederberg and Parry FFD technique [14] for 3-d manipulation of the nominal turbine blade core surface mesh, using the limited number of available measurements, for characterizing the geometric variations caused due to the presence of manufacturing variability.

4.2.2 Mathematical Formulations

Before considering the mathematics behind the FFD approach, the reader needs to be familiar with Bezier curves [75, 76] and possess a basic understanding of solid modeling [77]. This section discusses the mathematical formulation of the FFD technique proposed by Sederberg and Parry [14] in 1986.

FFD is defined in terms of a trivariate tensor product of Bernstein polynomials where the control points form the co-efficients of the polynomials. First of all, a local coordinate system is imposed upon the parallelopiped structure enclosing the object such that any point $\mathbf{P}$ has (s, t, u) coordinates in this system,

$$\mathbf{P} = \mathbf{P_0} + s\mathbf{S} + t\mathbf{T} + u\mathbf{U}, \tag{4.1}$$

where, $\mathbf{P_0}$ is the origin of the local coordinate system. The (s, t, u) coordinates of $\mathbf{P}$ can be found by the vector solution,

$$s = \frac{\mathbf{T} \times \mathbf{U}.(\mathbf{P} - \mathbf{P_0})}{\mathbf{T} \times \mathbf{U}.\mathbf{S}}, t = \frac{\mathbf{S} \times \mathbf{U}.(\mathbf{P} - \mathbf{P_0})}{\mathbf{S} \times \mathbf{U}.\mathbf{T}}, u = \frac{\mathbf{S} \times \mathbf{T}.(\mathbf{P} - \mathbf{P_0})}{\mathbf{S} \times \mathbf{T}.\mathbf{U}}. \tag{4.2}$$

It may be noted that for any point on the interior of the parallelopiped, $0 < s < 1$, $0 < t < 1$ and $0 < u < 1$. Now, a grid of control points ($\mathbf{G}_{ijk}$) is imposed upon the parallelopiped structure such that it is divided into $\alpha + 1$ planes in the $\mathbf{S}$ direction, $\beta + 1$ planes in the $\mathbf{T}$ direction, and $\gamma + 1$ planes in the $\mathbf{U}$ direction. For the Sederberg and Parry approach, these control points need to be uniformly spaced along each direction in accordance with the expression below :

$$\mathbf{G}_{ijk} = \mathbf{P_0} + \frac{i}{\alpha}\mathbf{S} + \frac{j}{\beta}\mathbf{T} + \frac{k}{\gamma}\mathbf{U}, \quad i = 0, \cdots, \alpha, \quad j = 0, \cdots, \beta, \quad k = 0, \cdots, \gamma. \tag{4.3}$$

Here, $\mathbf{G}_{ijk}$ is a vector containing the Cartesian coordinates of the control points for the nominal model. The positions of these coordinates can be varied to deform the model enclosed in this control point lattice structure. For the present problem, an optimization process was employed for deforming the nominal model by varying these control point coordinates within the specified lower and upper bounds, such that, the best match to the expected measurements was obtained. Details of this methodology are further presented in Sections 4.3, 4.4 and 4.6 that follow. The deformation function $\mathbf{P}_{ffd}$ is defined by a trivariate tensor product Bernstein polynomial,

$$\mathbf{P}_{ffd} = \sum_{i=0}^{\alpha} \binom{\alpha}{i} (1-s)^{\alpha-i} s^i \left[\sum_{j=0}^{\beta} \binom{\beta}{j} (1-t)^{\beta-j} t^j \left[\sum_{k=0}^{\gamma} \binom{\gamma}{k} (1-u)^{\gamma-k} u^k \mathbf{G}_{ijk} \right] \right], \tag{4.4}$$

where, $\mathbf{P}_{ffd}$ is a vector containing the Cartesian coordinates of the displaced point.

4.3 Formulation of the Objective function for Mesh Deformations

As discussed in Sections 4.1 and 4.2, the present work proposes the application of the FFD technique for generating a set of probable core shapes for turbine blades from the limited number of measurements available per blade. The deformed core meshes so generated will characterize the 3-d geometric variations that arise due to the presence of manufacturing variability. However, the task of obtaining the best match of the core shape to the probable actual blade measurements cannot be executed without a matching process working in conjunction with FFD. This is because the lattice control points in FFD are located on the parallelepiped structure enclosing the object to be deformed, and not essentially placed on the surface of the object itself (unless the object is a cube or a cuboid). Consequently, it is not easy to establish a direct relationship between the displaced coordinates of a control point and the relative deformation that takes place on the surface of the object as a result of this displacement. One may argue here that the DMFFD approach (discussed in Section 4.2.1) may overcome this problem. However, the DMFFD technique is more suitable for localized deformations. For the present problem, a balance between the local and global deformations was desired since the exact nature of deformations was uncertain due to the unavailability of further information.

However, the FFD process can be modified to induce the desired flexibility in the deformation process by changing the number of lattice control point planes along any of the x-, y- or z-directions. The deformations are relatively more global when the number of control point planes are reduced, and an increase in the number of these planes results in relatively localized geometry manipulation.

The problem of finding the best possible match to the expected core shape can be solved by selecting the coordinates of the measurement points on the nominal mesh, and using FFD to move these coordinates such that they get as close as possible to their expected values. The objective function for this optimization process may be defined as the sum of squared differences between the deformed positions of the selected points and their desired positions. This may be mathematically represented as below :

$$f(\mathbf{x_g},\mathbf{y_g}) = \sum_{i=1}^{n} \left[(x_{d,i}(\mathbf{x_g},\mathbf{y_g}) - x_{e,i})^2 + (y_{d,i}(\mathbf{x_g},\mathbf{y_g}) - y_{e,i})^2 \right], \quad i = 1, \cdots, n, \tag{4.5}$$

where,

n = number of selected points on the object (in our case, the number of measurement points),

$x_{d,i}$ = deformed x-coordinate position of the i^{th} point,

$x_{e,i}$ = desired (or expected) x-coordinate position of the i^{th} point,

$y_{d,i}$ = deformed y-coordinate position of the i^{th} point,

$y_{e,i}$ = desired (or expected) y-coordinate position of the i^{th} point,

$\mathbf{x_g}$ = vector containing x-coordinates of the control points,

$\mathbf{y_g}$ = vector containing y-coordinates of the control points.

4.4 Optimization with FFD

It may be noted in equation (4.5) that the objective function is non-linear in nature and hence the most obvious approach seems to be using one, or a combination of, non-linear optimization algorithms to solve the current problem. The focus of the present work is on using the already existing non-linear optimizers available in standard optimization packages, like iSIGHT [15] (for results obtained from iSIGHT, refer to Section 4.7), or as built-in functions in MATLAB. These tools are preferred since they are readily available and widely accepted in the aircraft engine manufacturing industry.

For the present case, our aim is to minimize the objective function ($f(\mathbf{x_g}, \mathbf{y_g})$) such that the control point coordinates, $\mathbf{x_g}$ and $\mathbf{y_g}$, are varied between $\pm 10mm$ from their respective nominal positions. Since the present problem does not involve any constraints, the optimization problem can be formulated as :

$$\min_{\mathbf{x_g},\mathbf{y_g}} f(\mathbf{x_g}, \mathbf{y_g}) \quad \text{such that} \quad \mathbf{lb_x} \leq \mathbf{x_g} \leq \mathbf{ub_x} \quad \textit{and} \quad \mathbf{lb_y} \leq \mathbf{y_g} \leq \mathbf{ub_y}, \tag{4.6}$$

where, the nominal positions of the control points are used as the initial estimate. In expression (4.6) above :

$\mathbf{lb_x}$ = vector containing the lower bounds for the x-coordinates of the control points,

$\mathbf{ub_x}$ = vector containing the upper bounds for the x-coordinates of the control points,

$\mathbf{lb_y}$ = vector containing the lower bounds for the y-coordinates of the control points,

$\mathbf{ub_y}$ = vector containing the upper bounds for the y-coordinates of the control points.

The final outcome of this optimization is the control point positions that minimize the difference between the deformed coordinate positions and the desired/expected coordinate positions of the selected measurement points. These new control point positions are then used to obtain the deformed mesh representing the probable manufactured core shape. This process can be repeated several times to apply different deformations to the nominal core each time.

4.5 Linear Least-Squares Solution

Another approach to solving the same problem as discussed in Sections 4.3 and 4.4 is to use a linear least-squares (LLS) solution in place of the optimization process. The advantage of using linear least-squares approach is that it results in a more exact solution to the FFD problem. On the other hand, the optimization process leads to relatively more regularized geometries as compared to the LLS approach. A constrained formulation of the LLS problem (as discussed in Section 4.5.2) can help in trade-off studies between the objective function as formulated in equation (4.5) and the delta deformations from the nominal model. However, caution needs to be exercised since in some cases the LLS approach may lead to over-fitting of the resultant geometry. This section discusses various formulations of the LLS solution that may replace the optimization process in accordance with the requirements of the user. For the present problem, the optimization procedure was considered sufficient to obtain the deformed geometries since the manufactured shapes are not expected to deviate a lot from the nominal design, and hence, more regularized solutions are desirable. However, the formulations discussed in Sections 4.5.1 and 4.5.2 may prove to be useful in cases where exact solutions to the shape matching problem, or, trade-off between the objective function and deviation from the nominal model are considered important.

It may be recalled that the final objective of the optimization process is to find suitable positions of the control points that would deform the nominal core mesh to its expected manufactured shapes. Now, as seen in expression (4.5), the objective function for the present problem is quadratic, but the expression for calculating the value of the deformation function, $\mathbf{P}_{ffd}$, is linear in nature. This may be noted by re-writing equation (4.4) as below :

$$\mathbf{P}_{ffd} = \sum_{i=0}^{\alpha} B_i^{\alpha}(s) \left[\sum_{j=0}^{\beta} B_j^{\beta}(t) \left[\sum_{k=0}^{\gamma} B_k^{\gamma}(u) \mathbf{G}_{ijk} \right] \right], \tag{4.7}$$

where, $B_i^{\alpha}(s)$, $B_j^{\beta}(t)$ and $B_k^{\gamma}(u)$ are the Bernstein polynomials for the s, t and u coordinates, respectively. Let us assume that we are displacing v lattice control points, such that,

$$\mathbf{G}_{ijk} = \begin{pmatrix} x_{g,1} & y_{g,1} & z_{g,1} \\ \vdots & \vdots & \vdots \\ x_{g,v} & y_{g,v} & z_{g,v} \end{pmatrix}, \tag{4.8}$$

where, $x_{g,1}, \cdots, x_{g,v}$ are the coordinates of the control points along the $\mathbf{S}$ direction, $y_{g,1}, \cdots, y_{g,v}$ are the coordinates of the control points along the $\mathbf{T}$ direction, and, $z_{g,1}, \cdots, z_{g,v}$ are the coordinates of the control points along the $\mathbf{U}$ direction. Now substituting equation (4.8) in equation (4.7), and expanding equation (4.7), we get,

$$\mathbf{P}_{ffd(x_g)} = B_0^{\alpha}(s) * B_0^{\beta}(t) * B_0^{\gamma}(u) * x_{g,1} + \cdots + B_{\alpha}^{\alpha}(s) * B_{\beta}^{\beta}(t) * B_{\gamma}^{\gamma}(u) * x_{g,v}, \tag{4.9}$$

$$\mathbf{P}_{ffd(y_g)} = B_0^{\alpha}(s) * B_0^{\beta}(t) * B_0^{\gamma}(u) * y_{g,1} + \cdots + B_{\alpha}^{\alpha}(s) * B_{\beta}^{\beta}(t) * B_{\gamma}^{\gamma}(u) * y_{g,v}, \tag{4.10}$$

$$\mathbf{P}_{ffd(z_g)} = B_0^{\alpha}(s) * B_0^{\beta}(t) * B_0^{\gamma}(u) * z_{g,1} + \cdots + B_{\alpha}^{\alpha}(s) * B_{\beta}^{\beta}(t) * B_{\gamma}^{\gamma}(u) * z_{g,v}. \tag{4.11}$$

In the above equations, $\mathbf{P}_{ffd(x_g)}$ gives the x-coordinate of the deformed point along the global X-axis, $\mathbf{P}_{ffd(y_g)}$ gives the y-coordinate of the deformed point along the global Y-axis, and, $\mathbf{P}_{ffd(z_g)}$ gives the z-coordinate of the deformed point along the global Z-axis. Now, if our objective is to deform n such selected points, we will have n equations with v unknowns along each of the X, Y and Z-axis respectively. It is apparent from equations (4.9), (4.10) and (4.11) that the n equations for each axis may be solved independently to obtain the v values which will form the columns of the matrix $\mathbf{G}_{ijk}$. Hence, this becomes a linear least-squares problem with n equations and v unknowns.

4.5.1 Bound-constrained Linear Least-Squares Solution

Using equation (4.9), the expression for the bound-constrained formulation of the linear-least squares solution can be written as :

$$\min_{\mathbf{x_g}} \|\mathbf{C}\mathbf{x_g} - \mathbf{d}\|_2^2 \quad \text{such that} \quad \mathbf{lb_x} \leq \mathbf{x_g} \leq \mathbf{ub_x}. \tag{4.12}$$

Here, the matrix $\mathbf{C}$ contains the product of the Bernstein polynomials as shown in equation (4.9) and $\mathbf{d}$ is defined as the vector containing the expected values of x-coordinates for the selected points. Thus, the expression $\mathbf{C}\mathbf{x_g} - \mathbf{d}$ accounts for the difference between the deformed model and the expected shape of the model. The nominal x-coordinates of the control points are selected as the starting point. These control points are varied in between $\pm 10mm$ from their nominal positions, i.e., by a magnitude of $10mm$ in either direction from the nominal coordinate values. The end result is a vector containing the x-coordinates of the control points that minimize the difference between the deformed x-coordinates of the selected points and the expected values of these coordinates. Similarly, expression (4.12) can also be used for obtaining the y- and z-coordinates of the control points for achieving the expected deformations in accordance with equations (4.10) and (4.11).

4.5.2 Constrained Linear Least-Squares Solution

The solution described in Section 4.5.1 works well for *overdetermined* problems with no constraints, i.e., in cases where $n>v$. However if $n<v$, the problem becomes that of finding a *minimum norm solution* to an *underdetermined* system of linear equations because there may be an infinite number of solutions to $\mathbf{x_g}$ that satisfy $\mathbf{C}\mathbf{x_g} - \mathbf{d} = 0$. In such cases, it is often useful to find a unique solution to $\mathbf{x_g}$ that would minimize the deformation of the base geometry since too much distortion of the deformed model from the base design would not be desirable.

If, in equation (4.12) the expression $\mathbf{C}\mathbf{x_g} - \mathbf{d}$ is replaced by $\mathbf{x_g} - \mathbf{x_{g0}}$, where $\mathbf{x_{g0}}$ is a vector defining the nominal coordinate values of the control points, the problem becomes that of minimizing $\|\Delta\mathbf{x_g}\|_2^2$ instead of minimizing $\|\mathbf{C}\mathbf{x_g} - \mathbf{d}\|_2^2$. Minimizing $\|\Delta\mathbf{x_g}\|_2^2$ will ensure that the solution we seek returns a deformed model that is as close as possible to the base model. This is desirable for problems in which the deformed geometry is not expected to deviate too much from the base geometry. It is also important that the condition $\mathbf{C}\mathbf{x_g} - \mathbf{d} = 0$ is not ignored. A possible solution is using this condition as a constraint for the given problem.

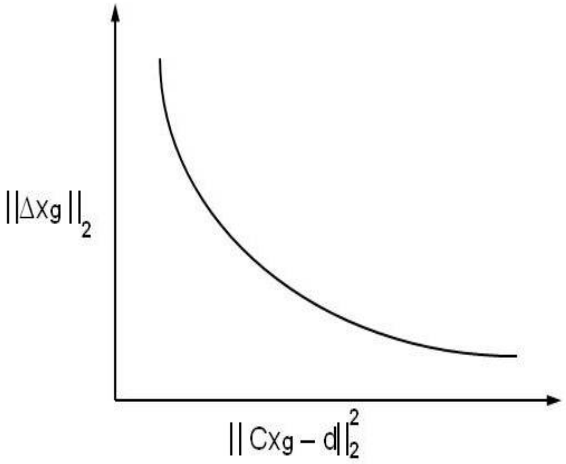

Figure 4.1: $\|\mathbf{\Delta x_g}\|_2$ vs. $\|\mathbf{Cx_g} - \mathbf{d}\|_2^2$ plot.

Defining this condition as an equality constraint might prove to be too stringent for most problems, since an exact solution of the equation $\mathbf{Cx_g} - \mathbf{d} = 0$ may not be feasible. An alternative way of formulating this condition is as a pair of inequalities such that a value $\pm\boldsymbol{\delta}$ is selected as the threshold. This value may be selected based on experience and the nature of the problem at hand. It may be noted however that an increase in the value of $\boldsymbol{\delta}$ increases $\mathbf{Cx_g} - \mathbf{d}$, and decreases $\mathbf{\Delta x_g}$. This implies that a decrease in deviation of the geometry from the base model results in increasing the differences between the deformed shape and the expected shape. This may be represented in the form of a plot between $\|\mathbf{\Delta x_g}\|_2$ and $\|\mathbf{Cx_g} - \mathbf{d}\|_2^2$ as shown in Figure 4.1.

Now, we need to establish the threshold constraint on $\mathbf{Cx_g} - \mathbf{d}$. This is given as,

$$-\boldsymbol{\delta} \leq \mathbf{Cx_g} - \mathbf{d} \leq \boldsymbol{\delta}, \tag{4.13}$$

$$\Longrightarrow \mathbf{Cx_g} - \mathbf{d} \leq \boldsymbol{\delta} \quad \text{and} \quad -\boldsymbol{\delta} \leq \mathbf{Cx_g} - \mathbf{d}, \tag{4.14}$$

$$\Longrightarrow \mathbf{Cx_g} - \mathbf{d} \leq \boldsymbol{\delta} \quad \text{and} \quad -\mathbf{Cx_g} + \mathbf{d} \leq \boldsymbol{\delta}, \tag{4.15}$$

$$\Longrightarrow \mathbf{Cx_g} \leq \boldsymbol{\delta} + \mathbf{d} \quad \text{and} \quad -\mathbf{Cx_g} \leq \boldsymbol{\delta} - \mathbf{d}. \tag{4.16}$$

Equation (4.16) may be represented in matrix form as below :

$$\begin{bmatrix} +\mathbf{C} \\ -\mathbf{C} \end{bmatrix} \mathbf{x_g} \leq \begin{bmatrix} \boldsymbol{\delta} + \mathbf{d} \\ \boldsymbol{\delta} - \mathbf{d} \end{bmatrix}. \tag{4.17}$$

Following this, the constrained formulation of the proposed solver becomes :

$$\min_{\mathbf{x_g}} \|\mathbf{x_g} - \mathbf{x_{g0}}\|_2^2 \quad \text{such that} \quad \left\{ \begin{array}{l} \begin{bmatrix} +\mathbf{C} \\ -\mathbf{C} \end{bmatrix} \mathbf{x_g} \leq \begin{bmatrix} \boldsymbol{\delta} + \mathbf{d} \\ \boldsymbol{\delta} - \mathbf{d} \end{bmatrix}, \quad \textit{and} \\ \mathbf{lb_x} \leq \mathbf{x_g} \leq \mathbf{ub_x}. \end{array} \right\} \tag{4.18}$$

Here, the initial guess for $\mathbf{x_g}$ needs to contain the local x-coordinates of the control points that satisfy the inequality constraint defined in equation (4.17). In cases where it is not easy to find a vector that satisfies the inequality constraint, it may be better to stick to the unconstrained linear least-squares solution, especially if the value of $\mathbf{Cx_g} - \mathbf{d}$ obtained is acceptable for the problem being analysed. Expression (4.18) may similarly be used for obtaining the solutions for the y- and z-coordinates of the control points in accordance with equations (4.10) and (4.11). Further details on this analysis are presented in Section 4.7.

4.6 Methodology for 3-d Geometry Manipulation using Limited Measurements

A flowchart representation of the methodology proposed for characterizing 3-d geometric variability in turbine blade core shapes using the limited number of available measurements is shown in Figure 4.2. As discussed previously in Chapter 3 Section 3.4, measurement data available on turbine blades was analysed using a methodology based on the PCA and FFT techniques for estimating the true thicknesses of the manufactured blades. These estimates were obtained in the form of 18 sets of minimum wall thickness measurements for 42 different blade shapes, capturing the effects of manufacturing variability. It is now desirable to use these measurements for estimating the probable complete 3-d geometric variability in the turbine blade shapes coming out of the manufacturing process.

Before applying any deformations to the nominal turbine blade model, it is essential to understand whether both the external blade airfoils and the internal cores are affected by manufacturing variability, or, only one of these surfaces show any changes. For this, a separate study was conducted in which measurements were taken on the external airfoil surfaces at different planes along the length of the blade using coordinate measuring machines. These airfoil shapes were then superimposed upon each other and showed that all the cross-sections for the different blades almost identically overlapped each other. This implies that the brunt of manufacturing variability is borne by the internal core surface of the blade. Actually, this does not come as a surprise if we recall the turbine blade casting process and various sources of manufacturing variability discussed in Chapter 2, Section 2.1. Therefore, it is considered more appropriate to fix the external blade shape and only deform the internal core for characterizing the 3-d geometric variability observed in the turbine blades.

A 3-d computer aided design (CAD) model of the nominal geometry and a volume mesh for FEA on this model were available. The coordinates of the 18 measurement locations for the nominal turbine blade shape were calculated using an embedded script in the CAD

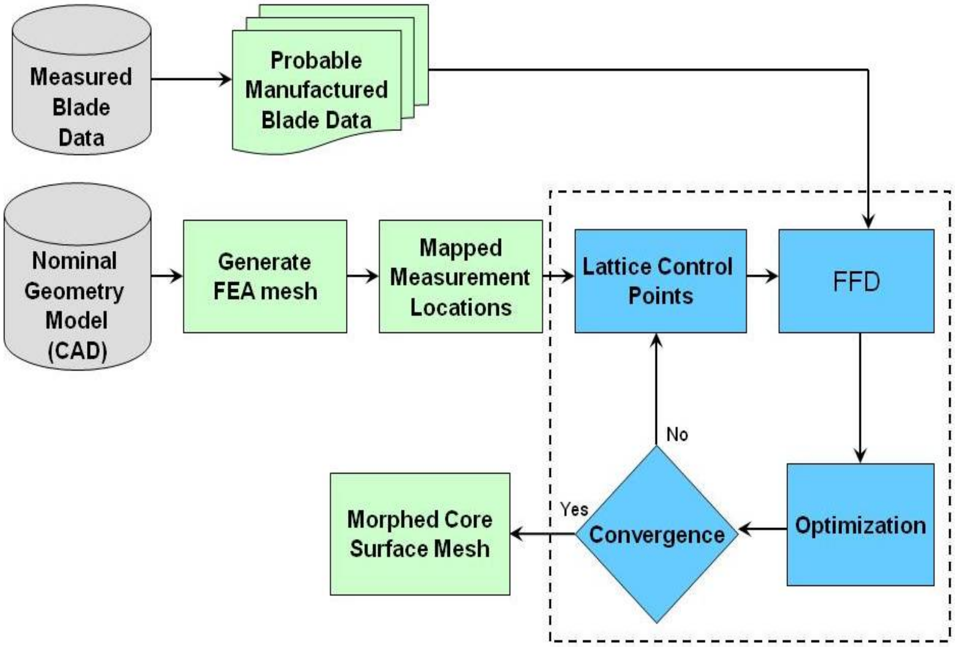

Figure 4.2: Flowchart representation of the methodology proposed for characterizing geometric variability in turbine blade core shapes using limited measurements.

model. It is assumed that the measurements obtained for the 42 probable turbine blade shapes are taken at these same locations, since it is almost impossible to obtain the exact measurement location coordinates for all the blades that are being manufactured and measured at the shop floor. This assumption may be supported by the fact that since FFD encourages smooth deformations, and the real measurement positions may be located somewhere close to the mapped measurement positions, the nodes adjacent to the mapped location will also undergo approximately similar displacements and in the same direction. Therefore, the (x,y,z) coordinates of the 18 measurement locations are mapped onto the surface mesh of the core which is extracted from the turbine blade volume mesh using the FEA tool.

The core surface mesh is fed into the FFD process and the nominal positions of the lattice control points are determined. These control point positions are then varied by the optimizer (or the linear least-squares solver) working in conjunction with the FFD process for minimizing the shape matching objective function. Once the optimization process has converged, the resultant optimal lattice control point positions are used for deforming the nominal core to its probable manufactured shape. This process may be repeated several times (42 times in the present case) for obtaining the 3-d geometric variability in turbine blade cores as a result of manufacturing variations.

4.7 Estimating 3-d Geometric Variability due to Manufacturing Variations

This section discusses in detail the application of the proposed methodology on the available hollow turbine blade data. Input data for the numerical studies presented in this section was obtained from the probabilistic data analysis studies conducted in Chapter 3 Section 3.4. As already noted, ultrasonic minimum wall thickness measurements on a randomly selected sample of 1050 turbine blades was analysed using the PCA and FFT techniques. This study resulted in a set of 18 thicknesses for 42 sets of reconstructed blade shapes capturing the effects of manufacturing drift with time and the blade to blade manufacturing error. The measurement locations for these 18 thickness values have already been discussed in Section 3.4. Volume meshes on these 42 reconstructed blades were required in order to conduct a detailed lifing, thermal and stress analysis of the probable manufactured turbine blade shapes. It was necessary therefore to recreate the perturbed geometries from the limited number of measurements available per blade.

As discussed in Section 4.6, it was observed that the effects of variations due to the manufacturing processes are mostly borne by the internal core shape, while the external airfoil surface remains relatively unchanged. Therefore, it seemed appropriate to deform the nominal core surface mesh in order to characterize the 3-d geometric variations resulting due to the presence of manufacturing variability. The challenge now is to use only 18 measurements available per blade for predicting the variations in shape of the entire core. According to the methodology proposed in Section 4.6, the surface mesh for the nominal core was extracted from the turbine blade volume mesh using the FEA tool. The Sederberg and Parry FFD approach [14] was implemented on the extracted core mesh, such that, $\alpha = 2$, $\beta = 1$ and $\gamma = 7$ control point planes were selected along the X, Y and Z-axis respectively. This creates 3 control point planes along the X-axis, 2 along the Y-axis, and 8 along the Z-axis. The resulting *lattice* of control points enclosing the core is shown in Figure 4.3. The analogy of selecting 6 control points along each cross-section may be compared to that of 6 measurement locations along the Tip, Mid and Root sections. Numbering the latticial planes as 1-8 from bottom to top of the core along the Z-axis, the control points on planes 4-7 were displaced in the x- and y-directions by the optimization

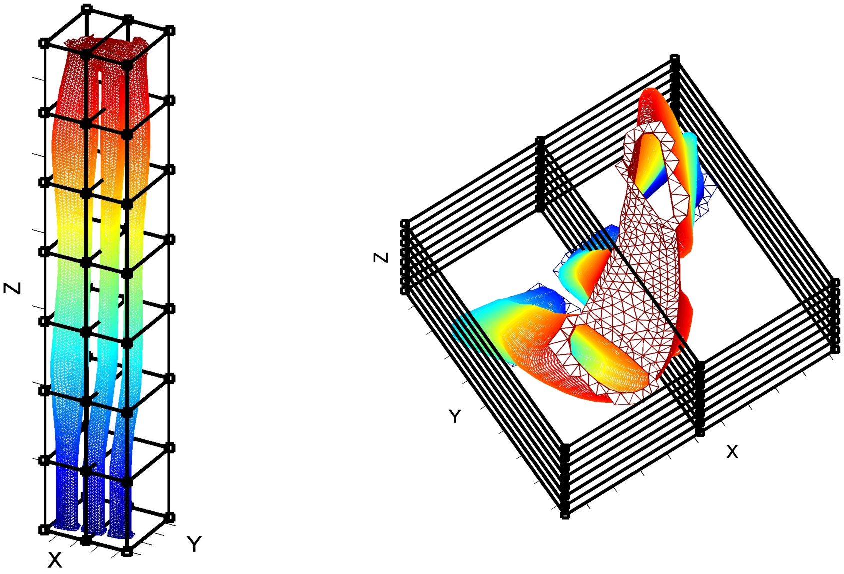

(a) (b)

Figure 4.3: (a) Front view of the core, and (b) cross-sectional view of the core, showing the FFD lattice of control points.

process keeping all the remaining control points fixed. This was done since planes 4-7 are closest to the Tip, Mid and Root cross-sections along which measurements were available. Therefore, it was decided to restrict the deformations to the surface around these cross-sections rather than deforming the core along its entire length where no measurements were available and the nature of deformations was uncertain.

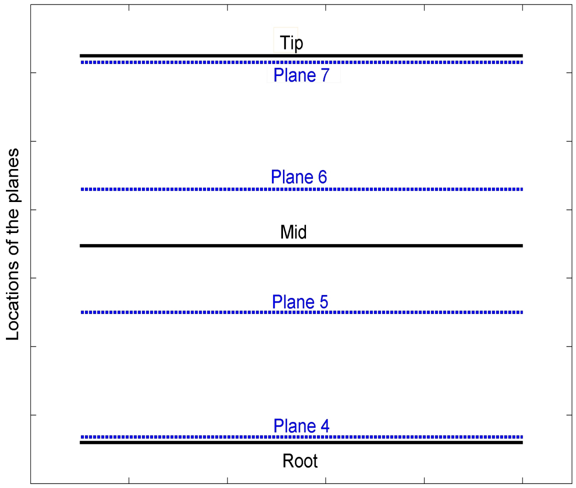

Figure 4.4: Locations of planes 4–7 along Z-axis relative to the Tip, Mid and Root measurement cross-sections.

The positions of planes 4-7 along the Z-axis relative to the Tip, Mid and Root measurement cross-sections is shown in Figure 4.4. It may be noted in Figure 4.4 that plane 7 is very close to the Tip, plane 4 is very close to the Root, but, planes 5 and 6 are almost at equal distances around the Mid section. The latticial planes are not located directly on the Tip, Mid and Root planes because the Sederberg and Parry

FFD technique [14] allows the placement of only equidistant planes along the three axis. This limitation may be overcome by using the NURBS based FFD [64] approach that allows the selection of non-equidistant latticial planes. However, we adopted the Sederberg and Parry FFD [14] technique for its mathematical simplicity and ease of implementation. Also, selection of a balanced number of planes in the region of interest helps ensure smooth deformations of the core surface.

It may be noted here that the flexibility of the FFD process is closely related to the number of control point planes selected for implementing the deformations. For example, in the present case, selecting a large number of closely spaced control point planes along the Z-axis may result in localized deformations. Conversely, selecting a smaller number of well spaced-out planes results in deformations that are more global in nature. For the present case, measurement data was available only across the Tip, Mid and Root cross-sections. This data may not be sufficient to predict if there are any localized deformations observed on the manufactured core shapes. In order to understand the exact nature of deformations, i.e. whether they are global or local in nature, it would be useful to conduct 3-d X-ray CT scans on a few randomly selected turbine blade samples. Understanding the exact nature of these deformations may enable a better selection of the number and location of the control point planes that should be displaced for implementing realistic deformations. However, for the purpose of the present research, selecting four control point planes along the length of the core for deforming the nominal geometry was considered appropriate due to the lack of availability of further information.

Some examples of deformed cores obtained from the proposed application of the FFD approach are shown in Figure 4.5. Figure 4.5(a) shows a nominal core with no deformation. Figure 4.5(b) shows a core with increased leg thickness obtained by moving the control points away from the core surface. Placement of this core in the nominal turbine blade model will decrease the minimum blade wall thicknesses. Figure 4.5(c) shows a core with reduced leg thickness obtained by moving the control points towards the core surface. Placement of this core in the nominal turbine blade model will increase the minimum blade wall thickness values.

In order to deform the nominal mesh on the core surface to the desired manufactured core shapes, an optimization process was performed in conjunction with FFD such that the 6 control points along the planes numbered 4-7 were displaced along the x- and y-directions. This resulted in a total of $2 \times (4 \times 6) = 48$ variables for the optimization process and one objective

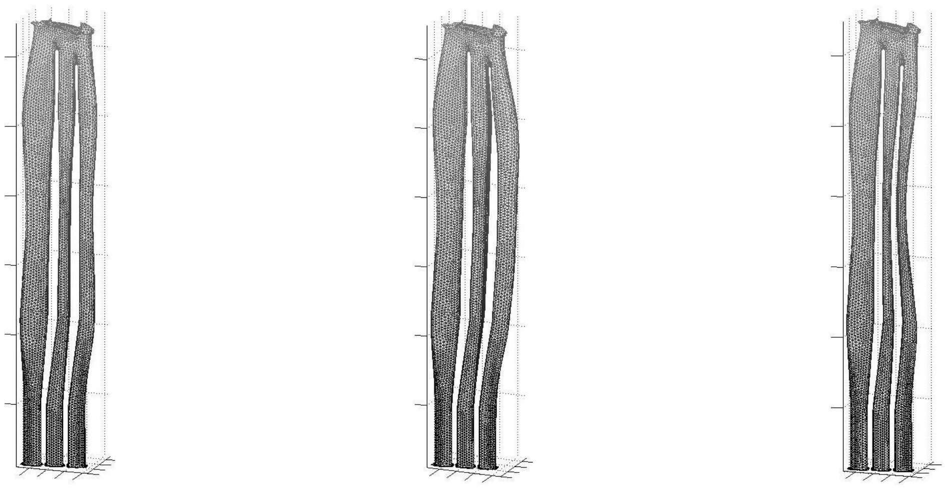

(a) (b) (c)

Figure 4.5: (a) Nominal core with no deformation. (b) Deformed core with increased leg thickness obtained by moving the control points away from the core. (c) Deformed core with decreased leg thickness obtained by moving the control points towards the core.

function as defined in equation (4.5). Various optimizers available in iSIGHT 9.0 [15] were tried for the present problem, but the best value of $f(\mathbf{x_g}, \mathbf{y_g}) = 0.006$ was obtained from an iSIGHT advisory optimization plan that used a combination of two non-linear optimizers - Step1 : LSGRG2 (a Generalized Reduced Gradient based optimizer), and Step2: NLPQL (a Sequential Quadratic Programming based optimizer). These techniques have been well-established and widely accepted over time and relevant details can be found in any standard textbook on optimization [78, 79]. The solution was attained after 4118 evaluations in approximately 3 hours. The resultant plot of the objective function vs. number of evaluations is shown in Figure 4.6. It was noticed that most of the time in iSIGHT was consumed for reading the input from, and writing the output into, '.txt' files, which was highly undesirable. Hence, it was preferred to use the built-in optimizers available in MATLAB since the input and output variables were internally available within the program that initiated the optimization process. Hence, a Sequential Quadratic Programming based constrained non-linear optimizer available in MATLAB, called '*fmincon*', was selected for this purpose. '$fmincon$' attempts to find a constrained minimum of a scalar nonlinear function of several variables starting at an initial estimate. Further details on this technique are readily available in the cited literature [80, 81, 82, 83, 84, 85, 86]. It was observed that '*fmincon*' produced the best results giving

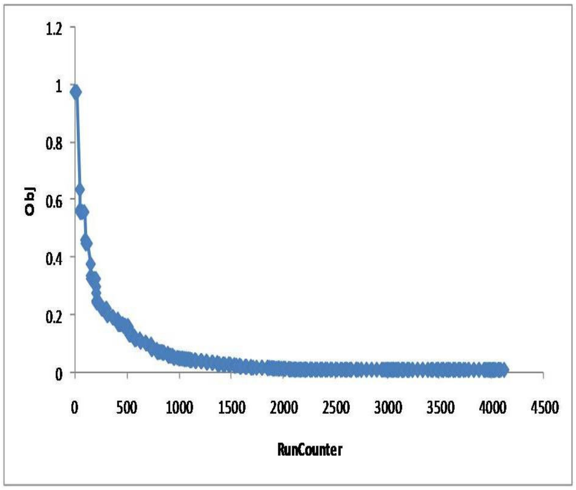

Figure 4.6: Plot of objective function vs. number of evaluations obtained from iSIGHT.

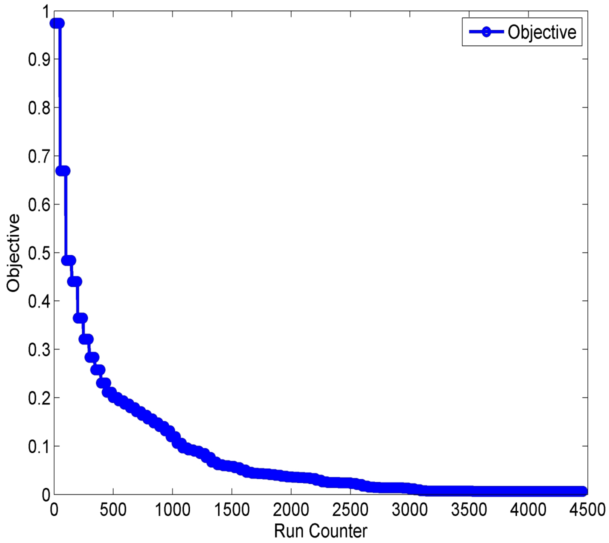

Figure 4.7: Plot of objective function vs. number of evaluations obtained from MATLAB.

the same value of $f(\mathbf{x_g}, \mathbf{y_g}) = 0.006$ as obtained from iSIGHT, but, in merely 5-7 seconds and around 4500 evaluations. A plot of the convergence history of the objective function obtained from this analysis is shown in Figure 4.7. Thus, the MATLAB optimizer definitely offered a much quicker solution to the same problem with the same precision and hence was preferred over iSIGHT.

Once the optimization studies were completed, it was desired to explore the capabilities of the linear least-squares solution approach for the given problem, as discussed in Section 4.5. There were $n = 18$ equations and $v = 48$ unknowns for the present case along each of the X, Y and Z-axis. A built in linear least-squares solver available in MATLAB, called '*lsqlin*', was employed for this purpose, first in its unconstrained form as discussed in Section 4.5.1. Details on this technique are available in the cited literature [87, 86]. Using the unconstrained formulation of '*lsqlin*', a value of $f(\mathbf{x_g}, \mathbf{y_g}) = 0.0005$ was obtained in 3-5 seconds. Although the present problem does not have any constraints, yet it is *underdetermined* in nature with the number of equations (18) less than the number of unknowns (48). Consequently, it appeared more appropriate to use the constrained linear least-squares approach for obtaining the displaced coordinates of the control points. However, the constrained form of linear least-squares approach could not be implemented without prior knowledge of the control point coordinates that satisfied the inequality constraint given in expression (4.17) and as discussed in Section

4.5.2. These coordinates were needed as inputs for the initial estimate of the vector $\mathbf{x_g}$. Since finding a suitable vector for the initial estimate of $\mathbf{x_g}$ was relatively more complicated, it was replaced by the end result for $\mathbf{x_g}$ obtained from the unconstrained formulation of the linear least-squares problem.

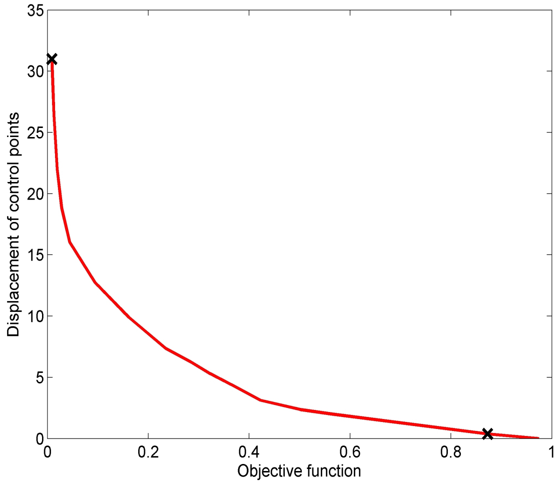

Figure 4.8: Displacement of control points ($\|\Delta\mathbf{x_g}\|_2 + \|\Delta\mathbf{y_g}\|_2$) vs. objective function ($\|\mathbf{Cx_g} - \mathbf{d}\|_2^2 + \|\mathbf{Cy_g} - \mathbf{d}\|_2^2$) plot obtained from constrained linear least-squares solution.

Following this, the value of $\boldsymbol{\delta}$ was increased in steps from 0.016 to 0.5 and the results obtained for $\|\Delta\mathbf{x_g}\|_2 + \|\Delta\mathbf{y_g}\|_2$ and $\|\mathbf{Cx_g} - \mathbf{d}\|_2^2 + \|\mathbf{Cy_g} - \mathbf{d}\|_2^2$ were noted. The resultant plot of the displacement of control points ($\|\Delta\mathbf{x_g}\|_2 + \|\Delta\mathbf{y_g}\|_2$) vs. objective function ($\|\mathbf{Cx_g} - \mathbf{d}\|_2^2 + \|\mathbf{Cy_g} - \mathbf{d}\|_2^2$) is shown in Figure 4.8. It may be observed that this curve looks similar to the expected curve in Figure 4.1. The value of $\|\mathbf{Cx_g} - \mathbf{d}\|_2^2 + \|\mathbf{Cy_g} - \mathbf{d}\|_2^2$ decreases as the displacement of control points from the base position increases. For a value of $\|\Delta\mathbf{x_g}\|_2 + \|\Delta\mathbf{y_g}\|_2 = 30.99$, $\|\mathbf{Cx_g} - \mathbf{d}\|_2^2 + \|\mathbf{Cy_g} - \mathbf{d}\|_2^2 = 0.008$ and for $\|\Delta\mathbf{x_g}\|_2 + \|\Delta\mathbf{y_g}\|_2 = 0.37$, $\|\mathbf{Cx_g} - \mathbf{d}\|_2^2 + \|\mathbf{Cy_g} - \mathbf{d}\|_2^2 = 0.87$. Looking at the curve, it appears that the best solution is obtained for a value of $\|\Delta\mathbf{x_g}\|_2 + \|\Delta\mathbf{y_g}\|_2 = 30.99$ with the value of objective function equal to 0.008. This is comparable with the results obtained from the optimizer based approaches discussed previously in this section. However, the problem of estimating the value of the starting point for a constrained linear least-squares solution remains unsolved.

The option that appeared better than non-linear optimization was the unconstrained linear-least squares (LLS) solution. Not only did it result in a lower value of the objective function, it also took relatively less time for convergence as compared to the optimization process. However, it was observed that the application of unconstrained LLS solver to the present problem resulted in relatively greater distortions in the core shapes from the nominal core geometry. In comparison, the core shapes obtained from non-linear optimization were more regularized. This is demonstrated in Table 4.1 which compares the percentage displacements in the x- and y-coordinates of the FFD control points relative to their nominal positions, obtained for the same set of expected measurements from the two competing techniques. As we can observe in the table, the LLS solution results in greater displacements from the nominal for most of the coordinate positions. Relatively, there a smaller number of coordinates for which the optimizer has resulted in greater displacements than the LLS solution. For a few coordinate positions, the same amount of displacements can be seen from both the techniques. The average values of percentage displacements indicate that the unconstrained LLS solution resulted in almost double the amount of deformations from the nominal core in both **X** and **Y** directions as compared to the non-linear optimization process. However, feeding in the gradient information to the optimizer resulted in the same solution as given by the linear least-squares approach. As stated before, the constrained LLS solution may help in this case since it allows a trade-off between the displacements of control points and the objective function values, provided, the starting point satisfying the inequality constraints is known in advance. This information was, however, not easily available for the current problem. For the present case, the deformed geometries were not expected to deviate a lot from their nominal shape. Hence, a more regularized solution from the optimization problem was sought. This led to the selection of '*fmincon*' as the final optimizer to be used in conjunction with FFD for obtaining the deformed core shapes that would capture the effects of manufacturing variability.

According to the methodology proposed in Section 4.6, FFD aided by optimization was applied to the nominal core surface mesh using the reconstructed measurements available on the 42 blades. As already discussed in Section 4.6, the coordinates of the measurement locations for the base core were calculated using the embedded script available in the nominal turbine blade CAD model. These 18 (x,y,z) coordinates were mapped onto the base core surface mesh extracted from the turbine blade volume mesh. It was assumed that the measurement locations remain unchanged for all the deformed geometries. The deformed Tip, Mid and Root cross-sections obtained from the application of the proposed methodology on the nominal core mesh are shown in Figure 4.9. The figure also compares the deformed cross-sections with the nominal for two out of the 42 reconstructed blades. It can be observed that the deformed cross-sections, for both blade 1 and blade 2, agree to a good extent with each other. This is desirable because the blades coming out of the manufacturing process are expected to be similar to each other. Also, the surfaces at the Tip section suction side almost overlap the nominal surface for both the deformed cores. This is interesting to note since the suction side at Tip section is the

Table 4.1: Comparison of percentage displacements in the FFD control point coordinates relative to their nominal positions, obtained from the non-linear optimization and unconstrained LLS solution.

i Coordinate no.	$x_{g,i}$ (Optimization)	$x_{g,i}$ (LLS solution)	$y_{g,i}$ (Optimization)	$y_{g,i}$ (LLS solution)
1	79.40%	78.38%	82.90%	82.90%
2	1.67%	37.92%	22.35%	82.90%
3	45.36%	81.67%	48.45%	82.90%
4	6.35%	12.49%	27.58%	40.08%
5	81.69%	81.69%	47.10%	161.17%
6	20.12%	1.94%	71.15%	79.66%
7	58.99%	81.69%	22.97%	204.72%
8	18.01%	17.81%	91.92%	184.88%
9	550.45%	742.00%	41.13%	36.59%
10	207.76%	565.75%	24.94%	82.90%
11	157.25%	737.99%	10.70%	14.16%
12	395.74%	367.16%	48.67%	82.90%
13	543.73%	687.53%	54.41%	63.07%
14	97.28%	78.85%	108.60%	204.72%
15	371.59%	742.01%	82.65%	109.43%
16	94.22%	191.43%	159.06%	204.72%
17	28.60%	14.16%	52.29%	21.95%
18	85.54%	104.75%	6.12%	82.90%
19	39.42%	23.01%	34.70%	48.66%
20	104.75%	104.75%	6.43%	38.28%
21	5.96%	82.66%	15.92%	4.29%
22	3.27%	104.75%	64.29%	54.18%
23	7.56%	47.36%	51.33%	204.72%
24	7.99%	29.42%	73.84%	166.75%
Average =	125.53%	209.05%	52.06%	97.48%

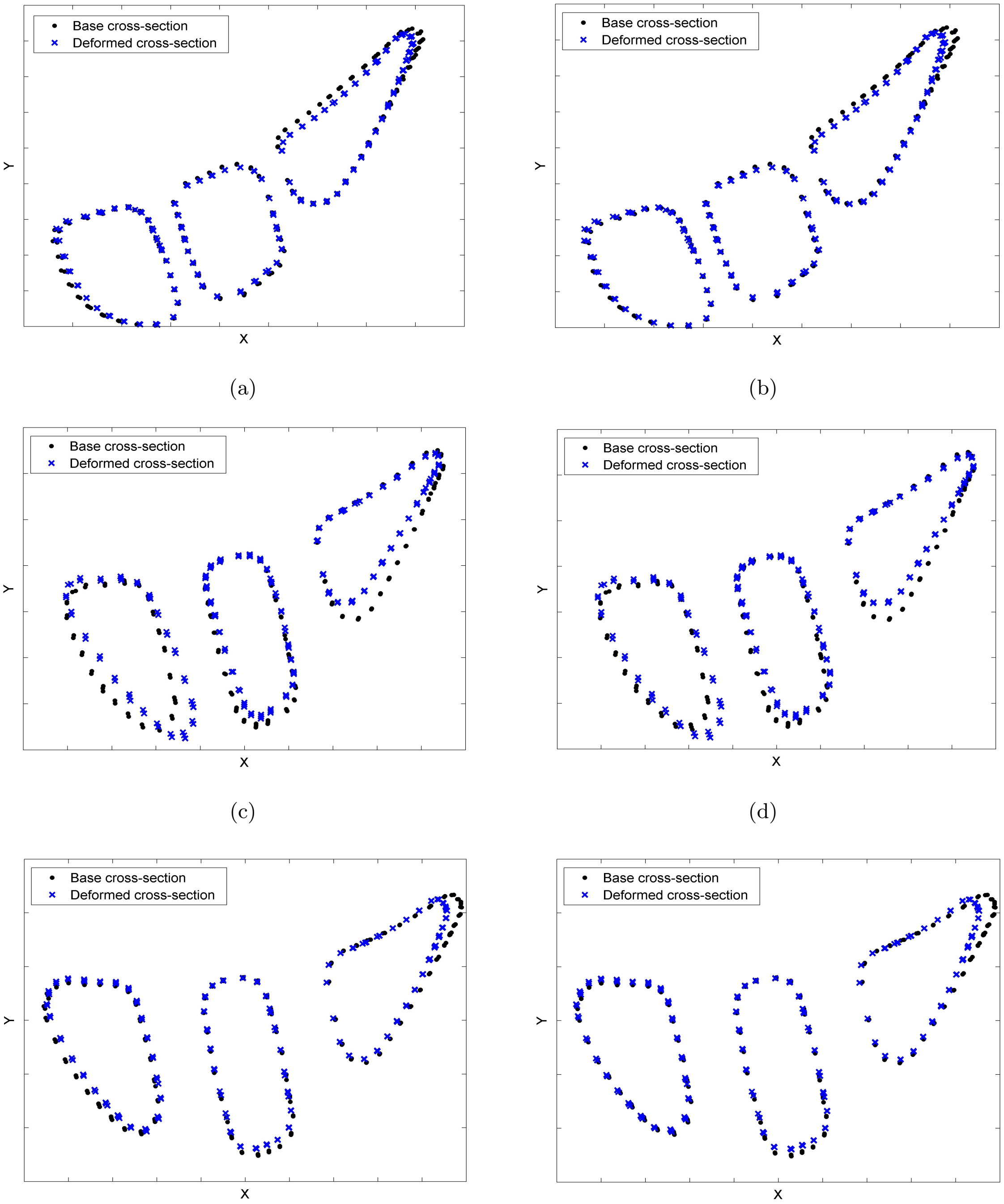

(a) (b)

(c) (d)

(e) (f)

Figure 4.9: Deformed Tip plane compared with nominal for (a) blade 1, and (b) blade 2. Deformed Mid plane compared with nominal for (c) blade 1, and (d) blade 2. Deformed ROOT plane compared with nominal for (e) blade 1, and (f) blade 2.

critical region for blade failure. Therefore, special care is taken while manufacturing to ensure that this region meets the design specifications. These observations indicate that the proposed methodology for characterizing 3-d geometric variability from the limited number of available measurements seems to work fairly well for the present problem. The deformed core meshes obtained from this study may be used further for generating morphed volume meshes for the probable manufactured turbine blade shapes. These volume meshes may then be used for lifing calculations, thermal and stress analysis.

4.8 Summary

In this chapter, a methodology was proposed for characterizing 3-d geometric variability from the limited number of available measurements, and, its application demonstrated on hollow turbine blades. A Free-Form Deformation based approach was implemented for generating the deformed core meshes for a sample of 42 reconstructed blades capturing the effects of manufacturing variability. Measurement data on each of these blades was available in the form of minimum wall thickness measurements across 18 locations per blade. The necessity of using an optimization process in conjunction with FFD for obtaining the best match to the probable manufactured core shape was also discussed. Various non-linear optimizers avaiable in different packages were tried for the present problem and the best solutions were obtained from a combination of LSGRG2 and NLPQL in iSIGHT, and '*fmincon*' in MATLAB. While iSIGHT 9.0 returned a value of the objective function equal to 0.006 in 4118 evaluations and approximately 3 hours, '*fmincon*' required only 5-7 seconds to converge to the same value of objective function in around 4500 evaluations. Alternative approaches to non-linear optimization, i.e., constrained and unconstrained forms of linear least-squares solution, were also explored. It was observed that although the linear least-squares approach may prove to be useful for a variety of problems, the non-linear optimizer was better suited for obtaining more regularized geometries which was desirable for the present study.

Finally, the non-linear optimization process was used in conjunction with FFD in order to obtain the deformed core geometries for the probable manufactured blade shapes. The Tip, Mid and Root cross-sections of the resultant core geometries were compared with the nominal cross-sections. It was observed that the deformations in the reconstructed geometries seemed to agree to a good extent with each other. This is desirable since the shapes of the turbine blades manufactured at the shop floor are expected to be similar to each other. It was also observed that the suction side surfaces at the Tip section for the deformed models overlapped the nominal model. Since this region is critical to blade failure, it is particularly ensured during the manufacturing process that this surface meets the design specifications. These observations indicate that the proposed approach for characterizing 3-d geometric variability from limited measurements seems appropriate for obtaining fair estimates of the manufactured shapes. The deformed core meshes obtained from this analysis can then be used further for generating 3-d volume meshes in FEA ready form for the probable manufactured turbine blades.

Chapter 5

Lifing Analysis and Linear Elasticity based Mesh Morphing

This chapter proposes the application of a linear elasticity based mesh morphing approach for obtaining morphed volume meshes on the turbine blade models in FEA ready form. The methodology implemented for mesh morphing is more commonly used in the study of fluid-structure interactions and has found some recent applications in medical engineering. However, its usage is still being explored for problems involving structural analysis. The chapter also gives a detailed explanation of the boundary conditions applied for lifing analysis and the results obtained from this analysis on the morphed meshes representing the probable turbine blade shapes manufactured at the shop floor. In addition, results from a mesh convergence study are also presented in order to determine the most appropriate mesh density for FE analysis.

The chapter is organized as follows : Section 5.1 discusses the need for mesh morphing algorithms and conducting a FE analysis for determining the effects of manufacturing variability. Section 5.2 describes in detail the boundary conditions applied for estimating life on the probable turbine blade shapes. It also presents the mathematical formulations for lifing calculations. This is followed by Section 5.3, which presents the results from the mesh convergence study in detail. Section 5.4 discusses the application of the linear elasticity based mesh morphing approach for the present case. Following this, Section 5.5 presents the results obtained from the numerical studies conducted for the present problem. In the end, Section 5.6 concludes this chapter discussing its main contributions and results.

5.1 Need for Mesh Morphing and Lifing Analysis

In Chapter 3, turbine blade inspection data taken on blades manufactured over a year was analysed to capture the effects of manufacturing drift with time and the blade to blade manufacturing error. The probable values of actual blade thicknesses so obtained were used in Chapter 4 for characterizing 3-d geometric variability in turbine blade shapes due to the presence of manufacturing variability. It was observed that the brunt of manufacturing variability is borne by the internal core shapes, whereas the external blade airfoils showed negligible changes in their profiles. Geometric variability in the internal core shapes was estimated using a FFD based approach that was used to deform the surface mesh for the nominal core to produce deformed meshes representing the probable manufactured core shapes. However, manufacturing variability analysis is incomplete without determining its effects on the blade life or performance in operating conditions. This leads to the need for generating FE meshes on the probable turbine blade shapes for lifing, thermal and stress analysis.

One approach to solving this problem is creating 3-d CAD models representing the different turbine blade shapes, exporting these models to the FEA tool, and meshing each model separately. However, this process is time consuming and labour intensive, hence, best avoided. Moreover, following this procedure for complicated shapes, such as turbine blades with both external and internal design features, may lead to additional complexity involved in the transfer of clean deformed geometries from the CAD package to the FEA tools. Therefore, a preferable solution to this problem is the usage of mesh morphing techniques which are available in abundance in the literature [88, 89, 90, 91, 92, 93]. Morphing the nominal mesh to produce representations of the probable manufactured turbine blades results in volume meshes in FEA ready form. These meshes may then be analysed for understanding the effects of geometric variations on turbine blade properties and performance. The focus of the present study is on estimating the effects of geometric variations, caused due to the presence of manufacturing variability, on the low cycle fatigue (LCF) life of turbine blades.

5.2 Boundary Conditions and Mathematical Formulations for Lifing Analysis

The aim of the present study is to estimate the effects of manufacturing variability on the LCF life of turbine blades at maximum take-off (MTO) conditions. Low cycle fatigue damage results from the application of cyclic stresses with high stress amplitudes at low frequencies usually resulting in a life of less than 1000 cycles. The MTO condition occurs only once per flight cycle, hence, for the MTO analysis, the number of cycles actually represents the life of turbine blades in terms of the number of flight cycles. This section presents the mathematical formulations and boundary conditions applied for a 3-d stress analysis of turbine blades for calculating the reserve factor (*Rfact*) which gives an indication of the LCF life, such that,

$$N_{life} = N_{critical\ life} * Rfact. \tag{5.1}$$

Here, $N_{critical\ life}$ represents the number of flight cycles for which the turbine blades are designed. In equation (5.1) above, the value of $Rfact$ is given as,

$$Rfact = \left| \frac{material\ fatigue\ strength}{worst\ principal\ stress} \right| \text{at temperature } T_0. \tag{5.2}$$

It is clear from equation (5.1) that *Rfact* is equal to the normalized value of life. Therefore, *Rfact* will be referred to as the normalized turbine blade life in the subsequent discussions.

The fatigue strength for the material at different temperatures was obtained from a test specimen and the worst principal stress was calculated from FE analysis. For obtaining the material fatigue strength at different temperatures (T_0), different test specimens made from the same material were subjected to cyclic stresses with different amplitudes at different temperatures. The number of cycles after which the blade failed due to elasto-plastic and creep deformations were recorded indicating the relationship between the stress amplitudes and blade life at different temperatures. Now, the stress amplitudes that the blade is able to withstand as the temperature varies were recorded for a value of life equal to $N_{critical\ life}$. These stresses indicate the values of *material fatigue strength* at different temperatures for the designed value of life. If the value of $Rfact = 1$, the blade life is equal to the designed life. If $Rfact>1$, the blade has a greater life than the designed life and if $Rfact<1$, the blade indicates a lesser life than the life for which it is designed. The value of the *worst principal stress* in equation (5.2) is the value of first principal stress (σ_1) since the tensile stresses are responsible for fatigue failure in the single crystal turbine blades.

A typical turbine blade volume mesh and the contour plots of the analysis temperature applied for the present problem are shown in Figure 5.1. The values (contour key) of the analysis temperature have not been shown due to the proprietary nature of this information. The temperatures increase as the contour colours change from blue to green to yellow to red. The temperature profile for the MTO condition was interpolated from a thermal analysis results file. The temperatures on the blade profile were predicted by a thermal FE analysis, the results of this analysis were validated by engine tests. The mapped values of the temperatures (*tmap*) at different nodes of the blade model were applied using a parameter *bldt* defined as,

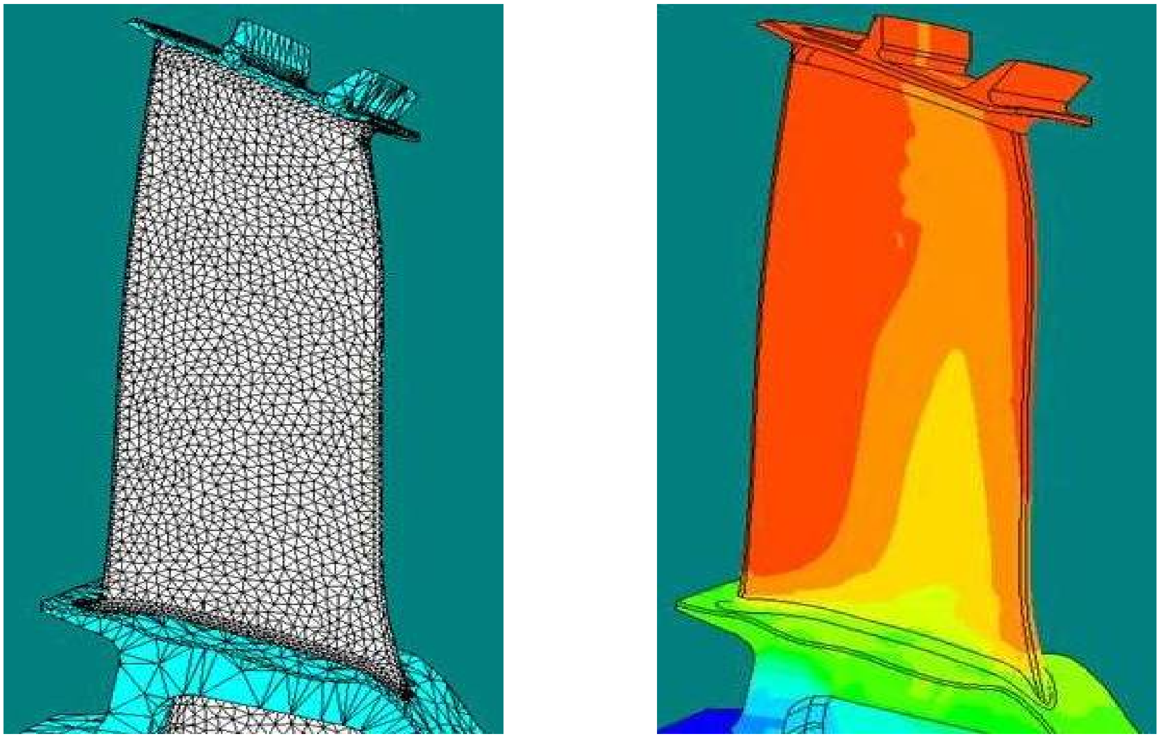
(a) (b)

Figure 5.1: (a) A typical turbine blade volume mesh. (b) Contour plots for the analysis temperature.

$$bldt = tmap \times thot, \tag{5.3}$$

in degrees Kelvin (K). *thot* is a scaling factor for engine running conditions. For MTO conditions, $thot = 1$. The gas loads acting on the pressure and suction side airfoil surfaces and the fillets present between the airfoil and adjoining features (i.e. the shroud and the platform), were also available in their scaled form in the form of data files. These loads were applied to

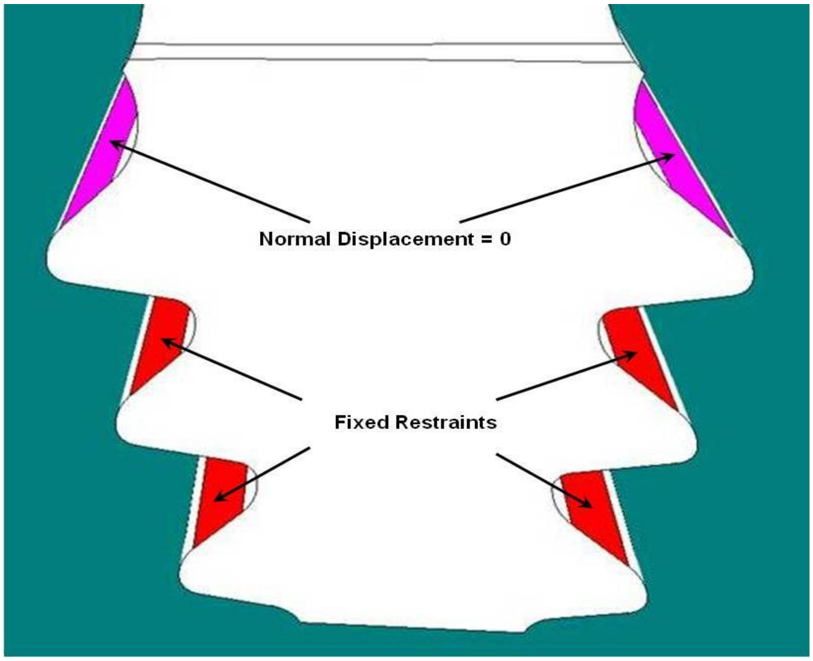

Figure 5.2: Normal and fixed restraints applied to the firtree faces of a typical turbine blade model.

the turbine blade models using a scaling factor $pf = 3.27$. The shaft speed was specified using a scaling factor $nf = 1$. Note that the actual values of the pressure loads and shaft speed applied for the present problem have not been discussed due to the proprietary nature of this information. The purpose of the scaling factors is to simulate different engine running conditions. The values of scaling factors stated above were used for simulating the MTO condition. These values can be changed to represent different engine running conditions that need to be considered for the stress analysis. Normal and fixed restraints were applied to the firtree faces as shown in Figure 5.2. Once the boundary conditions were applied as stated above, the FEA models were ready for fatigue life analysis. The results obtained from the lifing analysis with different meshes are presented further in Sections 5.3 and 5.5.

5.3 Mesh Convergence Study

Before proceeding with the FEA studies, it was essential to estimate the appropriate mesh size needed on the turbine blade models in order to achieve acceptable accuracy in the results. It is well-known that in FE modeling, a finer mesh typically results in a more accurate solution but requires larger computation time. Therefore, one always faces the problem of looking for a trade-off between solution accuracy and the required computation time. A typical mesh on a turbine blade model is shown in Figure 5.1(a). In order to conduct a mesh sensitivity analysis, five different *10 node tetrahedral* volume meshes were generated on the nominal turbine blade model, such that :

- Mesh 1 consisted of 49,934 elements with 85,592 nodes.
- Mesh 2 consisted of 76,642 elements with 125,872 nodes.
- Mesh 3 consisted of 80,271 elements with 131,207 nodes.
- Mesh 4 consisted of 124,540 elements with 201,017 nodes.
- Mesh 5 consisted of 127,661 elements with 205,891 nodes.

Boundary conditions, as stated before in Section 5.2, were applied on each of these meshes and a FEA conducted for obtaining the values of nominal life. Figure 5.3(a) shows the plot of normalized nominal turbine blade life vs. mesh size, and, Figure 5.3(b) shows a plot of the average percentage of stress error in the critical region vs. mesh size. As we can observe in Figure 5.3(a), the nominal life for Mesh 1 = 1.41, Mesh 2 = 1.44, Mesh 3 = 1.45, Mesh 4 = 1.45 and Mesh 5 = 1.45. Therefore, the value of Rfact seems to have converged for meshes 3,

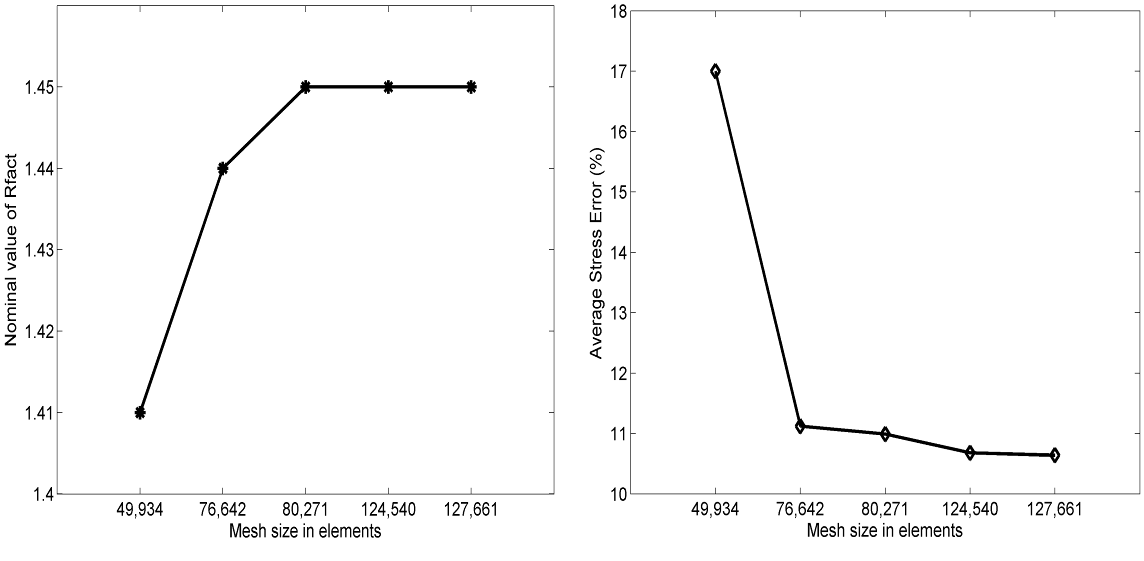

(a) (b)

Figure 5.3: Plots of (a) nominal life vs. mesh size , and (b) average stress error vs. mesh size.

4 and 5. Observing Figure 5.3(b), the average percentage of stress error around the critical region for Mesh 1 = 17%, Mesh2 = 11.12%, Mesh 3 = 10.99%, Mesh 4 = 10.68% and Mesh 5 = 10.64%. The percentage of stress error was calculated using the formula,

$$Percentage\ Stress\ Error\ (\%) = \left| \frac{stress\ error}{worst\ principal\ stress} \right| * 100. \tag{5.4}$$

According to turbine blade manufacturing company guidelines, the maximum acceptable stress error in the blade volume mesh is around 10%. The stress error represents the mesh discretization error and is a measure of the skewness of the elements constituting the FE mesh. The stresses on the nodes of a FE mesh can be represented in two forms - 1) The average stress based on the surrounding elements so that the stress contour is continuous across elements, or, 2) The non-averaged stress where the stress reported on each element is only based on the displacement of its own nodes. The difference between these two types of stresses accounts for the mesh discretization error. If the mesh is fine enough such that two neighboring elements have perfectly continuous stress contours, the averaged and non-averaged stresses will become equal and the stress error at each node will be zero. In Figure 5.3, since the solution has already converged for Mesh 3, it is not worth considering meshes 4 and 5 for the FE analysis. Selecting any of the meshes 4 or 5 will only add to the required computational time without affecting the accuracy of results. Now, the choice is to be made between meshes 1, 2 and 3. The average stress error for Mesh 1 is unacceptably high as compared to the acceptable stress error value of around 10%. However, the average stress error observed for Mesh 2 is around 11.12% which is fairly close to the threshold value. The nominal life calculations for meshes 2 and 3 were conducted using a single node of a computer cluster with Intel quad core processors, 2.8 GHz clock rate and 32GB RAM/node using 8 processes in parallel. The time taken for the entire FE analysis on Mesh 2 was around 17 minutes and on Mesh 3 was approximately 18 minutes. Finally, Mesh 3 was found to be most appropriate for the present study. The solution had already converged for this mesh, it took about the same computation time as Mesh 2, and, it also demonstrated an acceptable value of stress errors. Therefore, this mesh was used further for the variability analysis in turbine blade lives.

5.4 Linear Elasticity based approach for Mesh Morphing

As discussed earlier in Section 5.1, the analysis of manufacturing variability is incomplete without being able to determine its effects on the component's life, performance, etc. Going back to the CAD packages and creating multiple models for complicated geometries representing the different manufactured shapes may require months of effort, even by experienced users. Therefore, it is desirable to morph the nominal mesh multiple times for generating the desired shapes and obtaining 3-d meshes in FEA ready form for lifing, thermal and stress analysis.

For the present case, it was observed that most of the geometric changes due to manufacturing variations are observed in the internal core shapes and the external blade surface remains relatively unchanged. This information was employed in Chapter 4 for characterizing 3-d geometric variability in the turbine blade shapes by deforming the nominal core using a FFD based approach. Multiple representations of the deformed cores were obtained in the form of core surface meshes representing their probable manufactured shapes. It is now desirable to be able to use this information for morphing the volume mesh on the nominal turbine blade model to obtain 3-d volume meshes for the probable turbine blade shapes. For this, the linear elasticity based mesh morphing approach proposed by Stein et al. [89] was implemented. Although many alternative mesh morphing techniques are readily available in the literature [90, 91, 92, 93] for solving similar problems, this technique was preferred for its simplicity and ease of implementation.

5.4.1 Mathematical Formulations

The linear elasticity based mesh morphing approach is widely used in the study of fluid-structure interactions [89, 94, 95] and has also found some recent applications in medical engineering [96]. It attempts to find the displaced positions of the internal nodes in a FE volume mesh such that the displacements applied to the external surface act as boundary conditions. The motion of the internal nodes is governed by the linear elasticity equations [89] such that the connectivity of the mesh remains unchanged. The equilibrium equation governing the displacements of the internal nodes in the blade volume mesh is given as,

$$\boldsymbol{\nabla}.\boldsymbol{\sigma}^{\mathbf{T}} + \mathbf{f} = 0, \tag{5.5}$$

where, $\mathbf{f}$ is the external body force applied and $\boldsymbol{\sigma}$ is the Cauchy stress tensor defined as,

$$\boldsymbol{\sigma} = \mathrm{L}_1(\mathrm{tr}\boldsymbol{\epsilon})\mathbf{I}_t + 2\mathrm{L}_2\boldsymbol{\epsilon}. \tag{5.6}$$

In equation (5.6) above, L_1 and L_2 are the Lamé constants. L_1 is also called the Lamé's first parameter and simplifies the stiffness matrix in Hooke's law. L_2, also called the Lamé's second parameter, is the shear modulus. Relationships between the Lamé parameters, Young's modulus (E) and Poisson's ratio (ν) are given by the expressions :

$$\mathrm{L}_1 = \frac{E\nu}{(1+\nu)(1-2\nu)} \quad \text{and} \quad \mathrm{L}_2 = \frac{E}{2(1+\nu)}. \tag{5.7}$$

In expression (5.6), $\mathbf{I}_t$ is the identity tensor and tr is the trace of $\boldsymbol{\epsilon}$, where $\boldsymbol{\epsilon}$ is given by the strain-displacement equation,

$$\boldsymbol{\epsilon} = \frac{1}{2}\left[\boldsymbol{\nabla}\mathbf{w} + (\boldsymbol{\nabla}\mathbf{w})^{\mathbf{T}}\right]. \tag{5.8}$$

In the equation above, $\mathbf{w}$ is the displacement field. For the present problem, all nodes on the external blade surface are fixed with zero displacements in the x-, y- and z-directions. The displacements for the nodes on the core surface are defined as the difference between the nodal coordinates of the nominal core and the deformed core obtained from the FFD solution as discussed in Chapter 4.

The basic idea of this discussion is just to give an introduction to the mesh morphing strategy implemented for the present problem. The proposed mesh morphing technique can easily be applied on structural components using any standard FEA tools. Further details on this technique and the linear elasticity theory can be found in the cited literature [89, 94, 95, 96, 97, 98]. Alternative mesh morphing techniques are excluded from the scope of the presented research.

5.4.2 Mesh Morphing Methodology

A flowchart representation of the methodology implemented for morphing the turbine blade volume mesh is shown in Figure 5.4. As depicted in the figure, a volume mesh on the nominal turbine blade model is generated in the FEA tool. Surface meshes on the core and external blade surface are extracted from the nominal mesh. Fixed restraints are applied to the nodes on the external blade surface. The nominal core surface mesh is deformed using a FFD based approach as discussed in Chapter 4. This mesh is deformed multiple times in order to generate the different probable manufactured core geometries.

For each of the deformed core geometries, differences between the nodal (x,y,z) coordinates of the deformed surface mesh and the nominal core mesh are calculated. These delta values are applied as nodal displacements on the core surface of the nominal blade volume mesh. This is followed by a linear elasticity analysis for each of the deformed cores resulting in multiple morphed volume meshes representing the probable manufactured turbine blades. The resultant morphed meshes may then be used for estimating the effects of manufacturing variability on turbine blade properties.

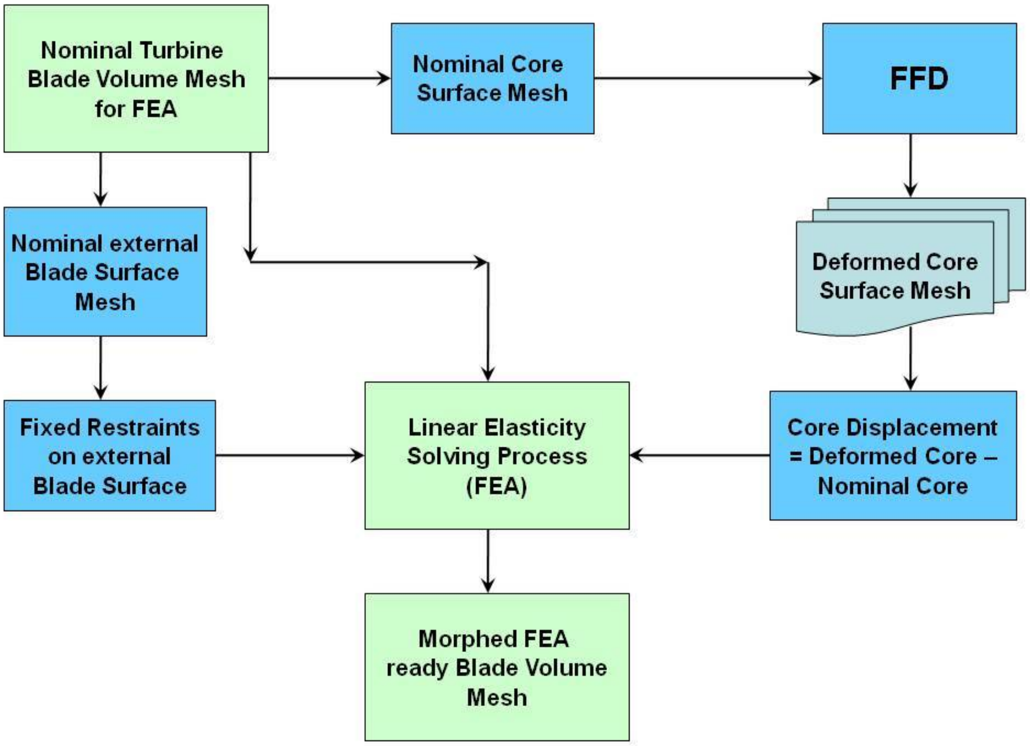

Figure 5.4: Flowchart representation of the methodology implemented for mesh morphing of the turbine blade volume meshes for FEA.

For example, in order to conduct a lifing analysis, boundary conditions are applied to each of these morphed meshes according to the description in Section 5.2. Then, a 3-d stress analysis is conducted on each mesh in order to calculate the value of $Rfact$ for the different probable turbine blade shapes. Calculating the mean and standard deviation for the values of $Rfact$ obtained from all the morphed meshes aids in estimating the variability in turbine blade life due to manufacturing variations.

5.5 Turbine Blade Lifing Analysis

This section discusses the numerical studies conducted for determining the effects of the manufacturing variations on turbine blade life. The input data for lifing analysis was obtained in the form of 42 deformed cores as a result of the studies conducted in Chapter 4. As stated before

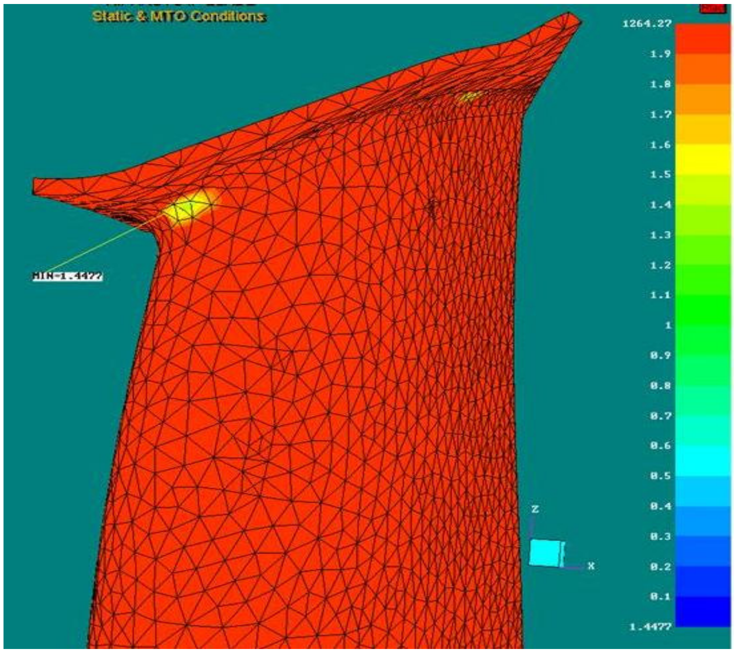

Figure 5.5: Critical region of blade failure.

in Section 5.3, a 10 node tetrahedral volume mesh with a mesh size of 80,271 elements and 131,207 nodes was generated on the nominal turbine blade model for FE analysis. Boundary conditions were applied on this mesh in accordance with the description in Section 5.2, followed by a 3-d stress analysis for MTO conditions. The FE analysis resulted in a normalized value of 1.448 for the nominal life. The critical region of blade failure obtained from this analysis is shown in Figure 5.5. As seen in the figure, possible failure due to fatigue stress is observed at the fillet joining the airfoil section to the shroud on the suction side leading edge.

In the next step, the surface mesh for the core was extracted from the nominal turbine blade volume mesh. The core surface mesh had 19,116 nodes. Displacements for these nodes were obtained by calculating the difference between the nodal (x,y,z) coordinates for each of the 42 deformed core meshes and the nominal core mesh. This was followed by extracting the external blade surface mesh from the nominal turbine blade volume mesh. The extracted surface mesh for the external shape of the blade consisted of 33,691 nodes. Fixed restraints were applied to all these nodes in order to restrict any shifting of the external surface during mesh morphing.

Following this, the nominal turbine blade volume mesh was taken and morphed 42 times by fixing the external blade surface nodes and moving the internal core surface nodes by the prescribed displacements. The linear elasticity solver available within the FEA tool was used for this purpose. The entire procedure of loading the nominal blade volume mesh, applying fixed restraints on the external blade surface, applying nodal displacements on the internal core surface and executing the linear elasticity solution for obtaining morphed meshes took around 32-37 minutes on a single node of a computer cluster with Intel quad core processors, using 8 processes in parallel at 2.8 GHz clock rate and 32GB RAM/node. To speed up the analysis, 42 runs were sent in parallel for the deformed geometries on different nodes of the computer cluster which resulted in generating all the morphed meshes in around the same time.

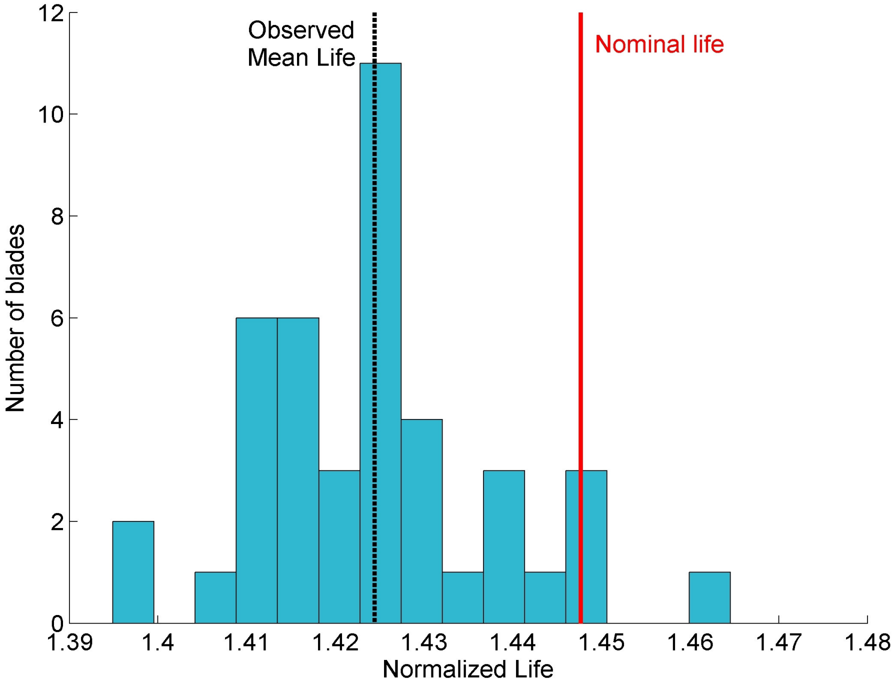

Figure 5.6: Histogram indicating the effect of manufacturing variability on normalized turbine blade life.

The morphed meshes obtained from the linear elasticity solving process were subsequently analysed using FEA for obtaining estimations of life for the probable manufactured turbine blades. Figure 5.6 shows the results obtained from the lifing analysis on the 42 meshes. It can be observed that the geometric variations introduced by replacing the nominal core with the deformed cores has resulted in reducing the turbine blade life in most cases due to the presence of manufacturing variability. This meets our expectations because although the nominal life is expected to be within the range of the maximum and minimum lives, most of the manufacturing variations are expected to reduce the blade life in comparison to its designed life. The figure also shows that for a couple of blades, the presence of manufacturing variations have demonstrated a positive effect by improving the blade life. On a normalized scale, these blades were designed for an average life of 1.448, but the mean life of the probable manufactured blades is observed to be 1.424 which is around 1.7% lower relative to the designed life. Also, the normalized value of life for the reconstructed blades varies between 1.395 and 1.465, the former being approximately 3.7% lower relative to the nominal life. The standard deviation in life for these blades was calculated as 0.0138.

5.6 Summary

In this chapter, a linear elasticity based mesh morphing approach was used in order to obtain morphed volume meshes for different turbine blade shapes in FEA ready form. Information obtained from FFD analysis in the form of deformed core surface meshes was used for generating 3-d volume meshes representing the probable manufactured turbine blade shapes. A mesh convergence study was conducted to explore the reliability of the results obtained from different meshes generated on the nominal turbine blade model. A 10 node tetrahedral mesh comprising 80,271 elements was selected as the preferred mesh size for the present problem. A 3-d stress analysis at MTO conditions was conducted on the 42 morphed meshes obtained from the linear elasticity solves. The results indicated that the mean life of the probable manufactured blade shapes was around 1.7% lower relative to the designed life, with, a maximum relative reduction of around 3.7% for turbine blades manufactured over a span of one year. The calculated value of standard deviation for the 42 analysed shapes was around 0.0138.

Chapter 6

Response Surface Models for Lifing Predictions

This chapter explores the application of response surface modeling techniques as a replacement during optimization for the computationally expensive FE calculations for the turbine blade lifing analysis problem. Here, the LP$_\tau$ DOE technique is used for generating the initial set of design points that are employed for generating RSM or surrogate models using the kriging approach. The organization of the chapter is as follows : Section 6.1 discusses the need for generating surrogate models in view of the problem at hand. Sections 6.2 and 6.3 give a concise introduction to the LP$_\tau$ technique and kriging, respectively. Section 6.4 briefly discusses the various model validation techniques that may be used for testing the reliability of response surface models (RSMs). This is followed by a detailed discussion in Section 6.5 of the numerical studies conducted for the current problem. The results and conclusions from the numerical studies are summarized in Section 6.6.

6.1 Need for Response Surface Models (RSMs)

Chapter 5 presented the effects of manufacturing variations on turbine blade lifing properties. The volume mesh on the nominal turbine blade model was morphed 42 times in order to generate representations of the probable manufactured turbine blades. A FE analysis was conducted on each of these morphed meshes resulting in estimations of the probable mean life and standard deviation in life. In order to reduce meshing errors in the lifing predictions, a mesh size of approximately 80,271 elements was used for each of the 42 morphed meshes. FE calculations on these meshes were run in parallel on 42 different nodes of a computer cluster with Intel quad core processors, 2.8 GHz clock rate and 32GB RAM/node using 8 processes in parallel. Due to the parallel runs, the wait time required by the user was around 37 minutes. However, the total computation time consumed for the entire analysis was around $37 \times 42 = 1554$ minutes, i.e., around 1 day and 2 hours.

Given that a methodology for estimating the mean and standard deviation in life is available, it is desirable to use this information for robust design studies with the objective of improving the mean life and minimizing the standard deviation in life. A detailed explanation of the robust design methodology is provided later in Chapter 7. If we decide to follow the mesh morphing approach discussed in Chapter 5, implementation of the robust design study would involve repeated FEA calculations on each of the new nominal designs for estimating the mean value of life and its standard deviation. Since these values will need to be calculated over and over for possibly thousands of designs, the process becomes computationally very expensive. This leads to the desire to use response surface models (RSMs) if at all possible.

Response surface or surrogate modeling techniques provide approximate or meta- models as computationally cheap alternatives to the original high-fidelity models, i.e., FEA models in our case. These methods generate approximations of the high-fidelity models by analysing an initial set of design points, together with the output/response values obtained for these points from the computational studies. This makes it very important to efficiently sample the parameter space for producing the initial design point dataset from which information is extracted for the surrogate models.

6.2 Design Space Sampling

Many efficient design space sampling techniques, commonly referred to as the design of experiments (DOE) techniques, are available in the literature [99, 100, 79]. These DOE techniques are broadly divided into two categories: 1) *classical* DOE approaches, and 2) *modern* DOE methods. Classical DOE approaches tend to generate design points at the extremes of the parameter space and offer more reliable trend extraction in the presence of randomness and non-repeatability [99]. Some examples of these techniques include, the central composite design, full- and fractional-factorial design, etc. On the other hand, modern DOE methods produce space filling design points since they are designed for use with deterministic computer simulations for which the non-repeatability component can be ignored [99]. Some examples of modern DOE techniques are, the quasi-Monte Carlo sampling, orthogonal array sampling, Latin hypercube sampling, etc.

A very popular technique in quasi-Monte Carlo sampling is the LP_τ sequence. LP_τ was first introduced by Sobol in 1967 [101]. It is a good example of quasi-random low-discrepancy sequences. "The term *discrepancy* refers to a quantitative measure of how much the distribution of samples deviates from an ideal uniform distribution" [99, 79]. Thus, low-discrepancy sequences try to sample the parameter space such that the design points are close to a uniform distribution. Quasi-random techniques use deterministic algorithms to generate the design points in a n-dimensional space [99, 79, 1]. Figure 6.1 shows an example of 100 design points generated in a 2-dimensional space using the LP_τ algorithm. A detailed exposition of this technique can be found in the cited literature [101, 102, 103, 104, 105].

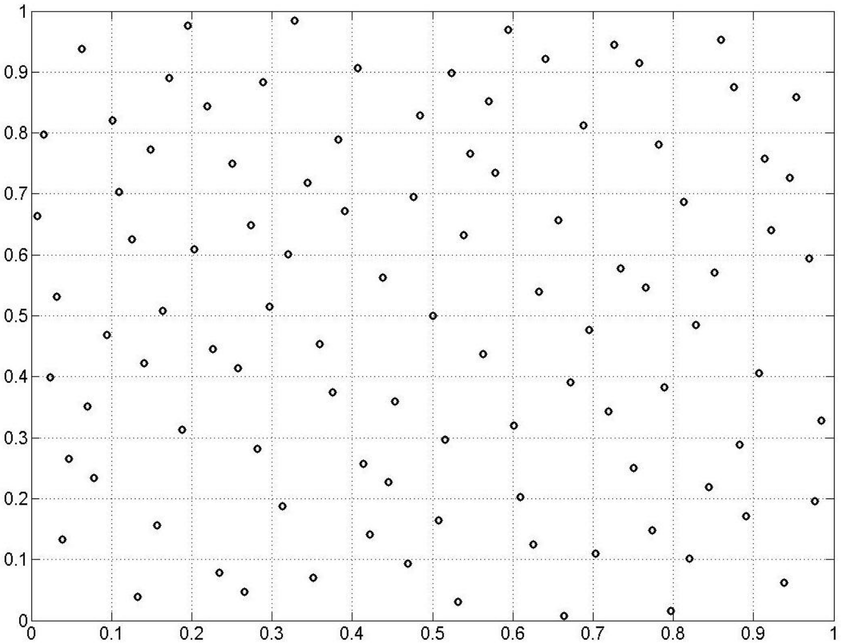

Figure 6.1: A sequence of 100 design points generated in 2-dimensional space using the LP_τ technique.

It was considered desirable to use the LP_τ approach for the present problem, not only because it gives a good coverage of the design space, but also because it allows additional points to be added to the existing design points without the need for repositioning the existing points [79]. This was considered important for the turbine blade problem because of the high probability of meshing errors at different design points leading to failure in lifing predictions. Further details on this analysis will be presented in Section 6.5.

6.3 Kriging

Kriging is a popular surrogate modeling technique developed by the French mathematician, Georges Matheron [106], based on the work of D.G. Krige [107]. The application of kriging for constructing approximations of computer models was first demonstrated by Sacks et al. [108] in 1989. Kriging has been used widely in conjunction with space filling DOE techniques for aerospace design optimization studies [1, 109, 110, 111, 79]. A detailed explanation of this technique can easily be found in the existing literature [112, 113, 114, 115, 111]. The mathematical description of Kriging that follows is based on the work of Jones et al. [113].

Let us assume, we have evaluated the output values for a dataset consisting of n variables at m different design points using the full computational model. Denote each design point by $\mathbf{x}^{(i)} = (x_1^{(i)}, \cdots, x_n^{(i)})$, the associated function value may be written as $y^{(i)} = y(\mathbf{x}^{(i)})$, where $i = 1, \cdots, m$ are the m samples. The model used to predict the response at any value $\mathbf{x}$ is then given as,

$$y(\mathbf{x}^{(i)}) = \mu + \varepsilon(\mathbf{x}^{(i)}), \quad i = 1, \cdots, m. \tag{6.1}$$

In the equation above, μ is the mean of the stochastic process and $\varepsilon(\mathbf{x}^{(i)})$'s are normally distributed "error" terms with zero mean and variance σ^2. The correlation between the "errors" at points $\mathbf{x}^{(i)}$ and $\mathbf{x}^{(j)}$ is given as,

$$\text{Corr}\left[\varepsilon(\mathbf{x}^{(i)}), \varepsilon(\mathbf{x}^{(j)})\right] = \exp\left[-d(\mathbf{x}^{(i)}, \mathbf{x}^{(j)})\right], \tag{6.2}$$

where, $d(\mathbf{x}^{(i)}, \mathbf{x}^{(j)})$ represents the weighted distance formula, such that,

$$d(\mathbf{x}^{(i)}, \mathbf{x}^{(j)}) = \sum_{h=1}^{n} \theta_h \left| x_h^{(i)} - x_h^{(j)} \right|^{p_h}. \tag{6.3}$$

In equation (6.3) above, θ_h and p_h are hyperparameters that are tuned using the input-output data available on the existing design points. The parameter θ_h measures the importance or 'activity' of the variable x_h. A large value of θ_h implies that x_h exercises more influence on the response variable, and vice-versa. The exponent p_h is related to the smoothness of the function in the h coordinate direction. Values of p_h near 1 imply less smoothness, and $p_h = 2$

corresponds to smooth functions. It can be observed in equation (6.2), that the correlation becomes near 1 as the distance between $\mathbf{x}^{(i)}$ and $\mathbf{x}^{(j)}$ becomes very small. Similarly, the correlation will approach zero when the distance between the two points becomes very large.

The Kriging model has $2n+2$ parameters, i.e., μ, σ^2, $\theta_1, \cdots, \theta_n$ and $p_1, \cdots, p_n$. These parameters are estimated by maximizing the likelihood of the sample. If $\mathbf{y} = (y^1, \cdots, y^m)^T$ denotes the vector of observed function values, $\mathbf{R}$ denotes the $m \times m$ matrix whose $(i,j)^{th}$ entry is Corr $\left[\varepsilon(\mathbf{x}^{(i)}), \varepsilon(\mathbf{x}^{(j)})\right]$, and $\mathbf{1}$ denotes the m-vector of ones, then the likelihood function is given as :

$$\frac{1}{(2\pi)^{n/2}(\sigma^2)^{n/2}\,|\mathbf{R}|^{\frac{1}{2}}}\exp\left[-\frac{(\mathbf{y}-\mathbf{1}\mu)^T\mathbf{R}^{-1}(\mathbf{y}-\mathbf{1}\mu)}{2\sigma^2}\right]. \tag{6.4}$$

In the expression above, the estimates of μ and σ^2 are given by the equations,

$$\hat{\mu} = \frac{\mathbf{1}^T\mathbf{R}^{-1}\mathbf{y}}{\mathbf{1}^T\mathbf{R}^{-1}\mathbf{1}}, \tag{6.5}$$

and

$$\hat{\sigma^2} = \frac{(\mathbf{y}-\mathbf{1}\hat{\mu})^T\mathbf{R}^{-1}(\mathbf{y}-\mathbf{1}\hat{\mu})}{m}. \tag{6.6}$$

By substituting equations (6.5) and (6.6) into expression (6.4), the ‘concentrated likelihood function’ is obtained that depends only on the hyperparameters θ_h and p_h, where $h = 1, \cdots, n$. This function is maximized to estimate the values of θ_h and p_h for the given data. Equations (6.5) and (6.6) are then used to obtain the estimates $\hat{\mu}$ and $\hat{\sigma^2}$. For the present problem, the hyperparameters were tuned using the entire set of initial design points. Hyperparameter tuning and generation of the kriging based RSMs was implemented using the OPTIONS design exploration system [116]. Application of this approach to the current problem is discussed further in Section 6.5.

6.4 Model Validation

Once the RSM has been constructed, the next step involves assessing the quality of the surrogate model through model validation studies. There are various ways of validating metamodels :

- Separate ‘training’ and ‘testing’ datasets may be created on which the responses are already known. The ‘training’ dataset is used for generating the RSM. The points in the ‘testing’ dataset may then be employed for comparing the predictions made by the RSM with the known outputs.

- The leave-one-out cross-validation procedure may be used which involves leaving one observation out of the initial set of design points and using the remaining points for generating the RSM. The response predicted by this RSM at the ‘left-out’ design point is then compared with the known output value. This process is repeated for every point in the initial dataset to assess the quality of the approximate models. Normally, the hyperparameters used are fixed at those obtained for the full dataset.

- The k-fold cross-validation procedure may be used which is essentially the same as leave-one-out procedure except that k instead of 1 design points are ‘left-out’. This test is thought to be more rigorous than the leave-one-out type of cross-validation.

For the present problem, the leave-one-out cross-validation procedure was preferred over the other two because of the limitation in terms of the number of available initial design points. Details of this study will be presented in Section 6.5 that follows.

6.5 RSMs for the Turbine Blade Problem

The methodologies used for perturbing the nominal mesh, and using FEA for estimating the mean and standard deviation in life, have already been presented in Chapters 4 and 5 respectively. It was now desired to perform robust design optimization studies in search of a new nominal turbine blade model which not only resulted in a better mean life, but also reduced the standard deviation in life due to manufacturing variations. This meant that thousands of new nominal designs were to be explored for their nominal and mean lives, and standard deviation. As discussed before in Section 6.1, the computation time required for mesh morphing and lifing calculations on each blade was around 37 minutes. This meant that a total computation time of around 1 day and 2 hours was required for conducting the lifing analysis on the entire set of 42 perturbed geometries per nominal design. This was undesirable because of the high cost and time associated with each run. Therefore, it was considered more appropriate to generate RSMs which would give reliable predictions of the blade life for a given set of 18 thicknesses that defined its geometric properties. The positioning of these 18 thickness values on the turbine blade model has already been discussed in Chapter 3, Section 3.4.

The probabilistic studies conducted in Chapter 3 left us with 42 sets of 18 thicknesses capturing the probable effects of manufacturing variations. This data consisted of an inappropriate number of design points for generating surrogate models because we were looking at an

18-dimensional parameter space with only 42 design points. As a rule of thumb, the number of initial design points needed for generating approximate models are around 10 times the number of dimensions [113]. This led to the addition of 158 design points to the existing dataset of 42 blades using the LP$_\tau$ DOE technique. The lower and upper thickness specification limits used during the blade inspection process were used as the lower and upper bounds for randomly generating a set of 500 points, in 5 steps of 100 points each. One may wonder here of the need for 500 points when only 158 additional points are required. This was done to make up for the lack of knowledge of the design feasibility in the existing parameter space. For example, in the present case, the FE tool was able to successfully perform lifing calculations for only 100 out of the first 230 design points. All the remaining 130 design points failed due to meshing errors. Such failures are unavoidable when automated mesh generation tools are dealing with significant shape changes and highly complicated geometries.

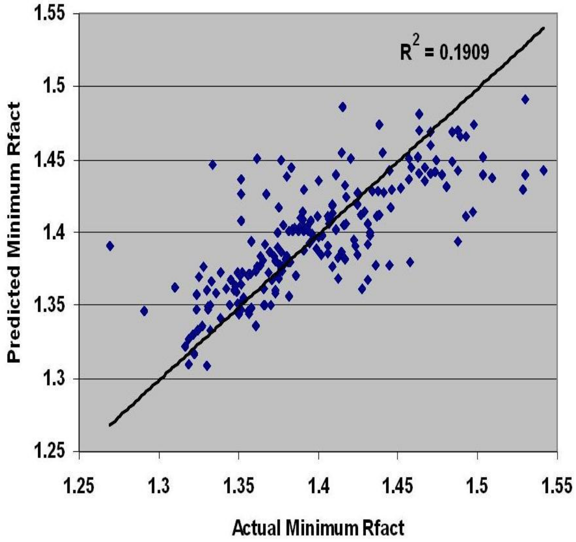

Figure 6.2: Correlation plot for the predicted vs. actual values of $Rfact$ for the 18 variables - 200 blade data.

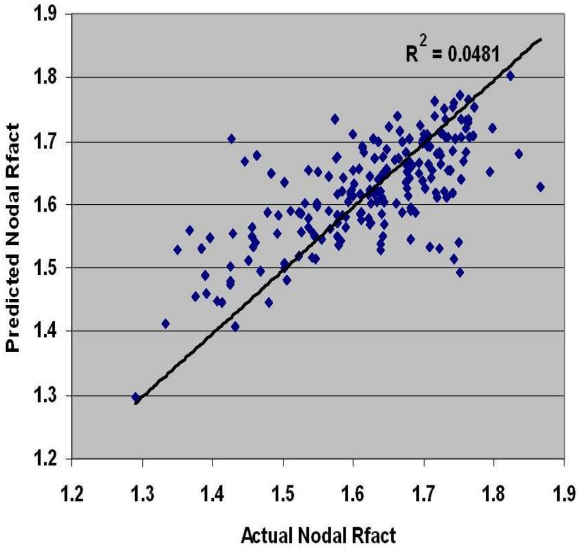

Figure 6.3: Correlation plot for the predicted vs. actual values of nodal $Rfact$ for the 18 variables - 200 blade data.

The final dataset consisting of 200 design points (each design point consisted of a vector of 18 variables), and the value of $Rfact$ for each of these points, was used for generating a surrogate model using the kriging approach. As discussed before in Section 6.4, the leave-one-out cross-validation procedure was used in the present case for assessing the reliability of the RSM. A correlation plot of the predicted vs. actual values of $Rfact$ for this data is shown in

Figure 6.2. As we can observe in the figure, the surrogate model is not modeling the data very well and shows a squared correlation coefficient (R^2) value of 0.1909. Values of R^2 closer to 1 indicate excellent reliability and those closer to zero indicate very poor reliability of the RSM.

Even though, in general, the critical region of the turbine blade does not change from blade to blade, the node indicating the minimum value of life may change from one model to another. This variability in the nodal positions may add to the complexity of modeling the data. In order to make the problem simpler, a trial was conducted to model this data such that the value of $Rfact$ at the same selected node was to be predicted. If this worked, the idea was to create multiple RSMs, different RSMs predicting $Rfact$ for different nodes in the critical region, and take the minimum of these predicted values for estimating life. The correlation plot of the predicted vs. actual values of $Rfact$ at a selected node for the previously generated 200-blade dataset is shown in Figure 6.3. It is surprising to see that the approximate model produced from this data is slightly more unreliable, with $R^2 = 0.0481$, as compared to Figure 6.2. Following this, an attempt was made to simplify the problem further by trying to model the worst principal stress at a selected node as a response for the different input values of 18 thicknesses. Parallel RSMs could then be used for predicting the worst principal stress at different nodes in the critical region. According to the formula in equation (5.2), the maximum of these values could then be used to predict the life for a particular design point. The correlation plot for this data is shown in Figure 6.4 where the same 200 design points were used to model a RSM for stress predictions. The R^2 value in this case is not any better than those observed in Figures 6.2 and 6.3.

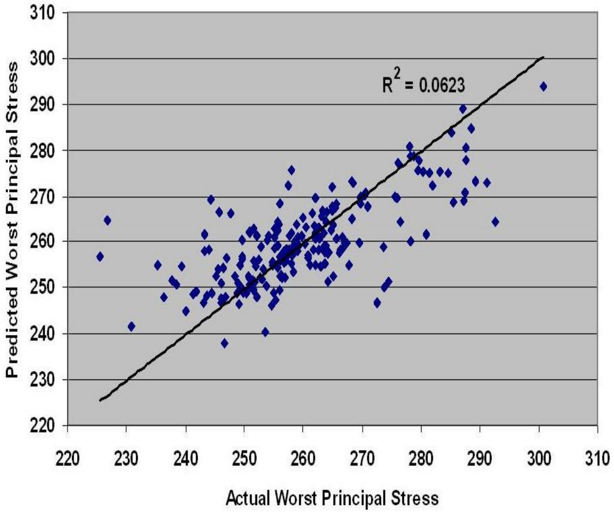

Figure 6.4: Correlation plot for the predicted vs. actual values of nodal worst principal stress for the 18 variables - 200 blade data.

The unreliability of the surrogate models for the 200-blade data may be explained because it is an attempt to model a series of complicated processes. A simplified flowchart representation of these processes and the order in which they are executed is shown in Figure 6.5. As seen in the flowchart, 18 thicknesses representing the geometric variations are used to calculate the expected FFD control point positions for the deformed core model. These expected control point coordinates are fed into the FFD process which works in conjunction with optimization to result in the final optimized positions for the control points. The optimal control point coordinates are then employed by FFD to regenerate the 3-d core geometry. Details of this methodology have already been presented in Chapter 4. Nodal displacements calculated from the deformed core geometries are used for mesh morphing in the FEA tool using linear elasticity based approach. FE lifing calculations are then performed on the morphed volume meshes resulting in the worst principal stress and $Rfact$ values. This study has also been discussed in detail previously in Chapter 5.

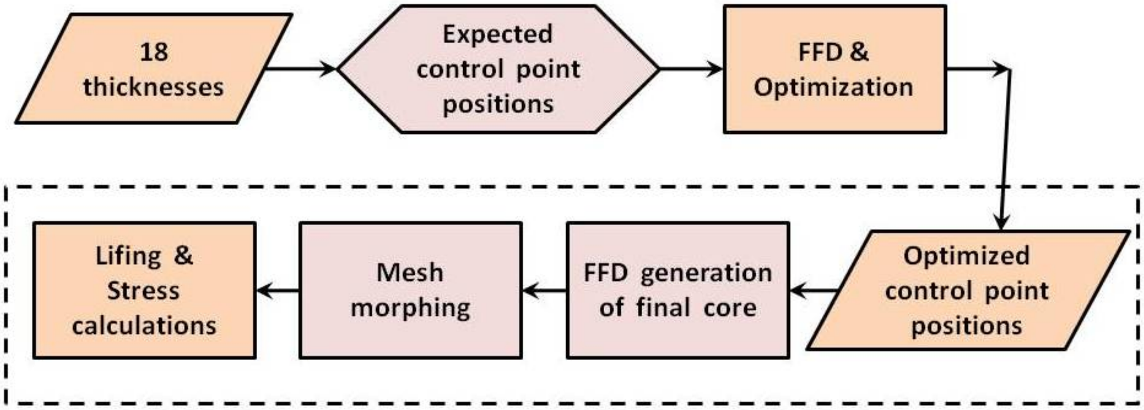

Figure 6.5: Simplified flowchart representation of the processes being modeled by kriging.

Until now, our expectation from kriging was to model these entire series of complex processes and relate the 18 thickness values to the output $Rfact$ or worst principal stress values, which may be too much to ask. Following this realization, it was considered more appropriate to use the optimized values of FFD control points as inputs ($\mathbf{x}$) and then try to generate surrogates for life or stress predictions. The dashed box in Figure 6.5 encloses the truncated series of processes to be modeled by kriging in this fresh attempt. It would still be beneficial if the RSMs in this case proved to be reliable since the majority of the computation time was consumed by the FE calculations involved in mesh morphing and lifing estimations. The time consumed by the FFD and optimization methodology was not more than 2-3 minutes per design point. However, the number of FFD control points used for core deformations still posed a major problem.

As noted before in Chapter 4 Section 4.7, 24 control points were moved in the x- and y-coordinate directions to deform the nominal core. This converted into 48 variables that were involved in the optimization and free-form deformation process. It is commonly found that it is difficult to set up surrogate models using kriging for more than 10-20 variables and the approach also becomes numerically expensive for more than a few hundred data points [109]. Moreover, the generation of 480 initial design points needed in this case meant analysis of around 1100 random points for estimating the required output values from the computational model. This was practically infeasible. In order to overcome this problem, it was decided to analyse the effect of geometric changes around each variable plane in the FFD process (refer Figure 4.4) on the output life. The idea now was to model the effects on life due to the geometric changes introduced by varying the control points on each of the variable Planes 4-7, separately. This would result in generating 4 different RSMs, one for each latticial plane. These 4 RSMs could be run in parallel to predict the value of life. An average of the values of lives predicted by these 4 surrogate models could give us an estimation of the expected life for the whole turbine blade model.

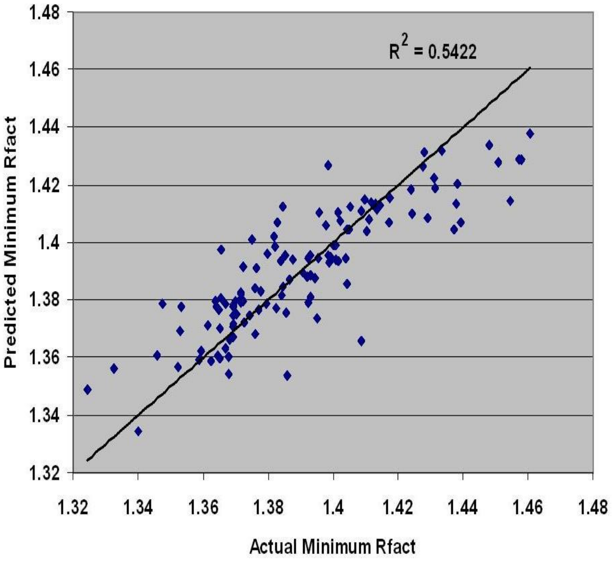

Figure 6.6: Correlation plot for the predicted vs. actual values of $Rfact$ for the 12 variables - 120 blade data.

To start with, the FFD process was modified such that only the control points on Plane 7 (refer Figure 4.4), which was closest to the Tip section, were allowed to vary and all the remaining latticial planes were fixed. A new 120-blade dataset was produced consisting of the output values, i.e. $Rfact$, and their corresponding 12-variable input vectors. One of the challenges faced while creating this initial design data was that the lower and upper bounds of the control points were not known. Thus, LP_{τ} could not be used directly to generate the initial design points. Instead, the 500 design point data produced previously using the lower and upper design specifications on the 18 thickness values was used to overcome this problem. Using the same values of expected thicknesses as generated for the 500 point data, FFD was employed such that only the 6 control points on Plane 7 were moved by the optimization process. Since the remaining 18 control points on Planes 4-6 were fixed, the converged value of objective function for each design point was much greater now. However, this helped in obtaining fair estimations of the control point positions and hence of the 12 variables in each case. The reduced deformation due to limited movement of control points also improved the success rate of FEA. Output values for 120 design points were obtained only from the first 134 points in the parameter space. A correlation plot obtained from the leave-one-out validation of the RSM generated from this data is shown in Figure 6.6. As seen in the figure, kriging is still not modeling the data very well with a squared correlation coefficient value of only 0.5422.

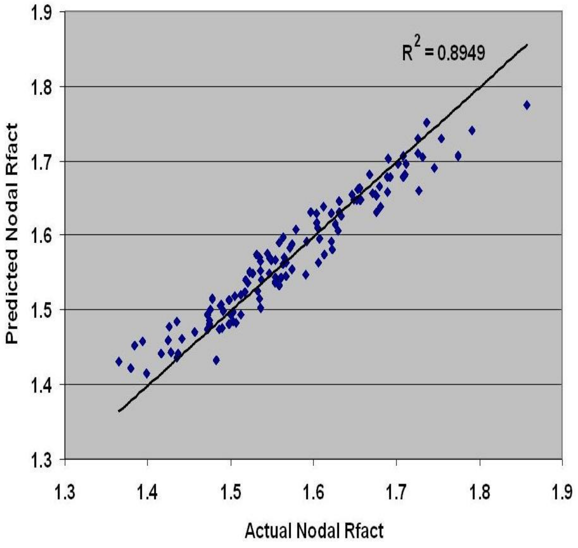

Figure 6.7: Correlation plot for the predicted vs. actual values of nodal $Rfact$ for the 12 variables - 120 blade data.

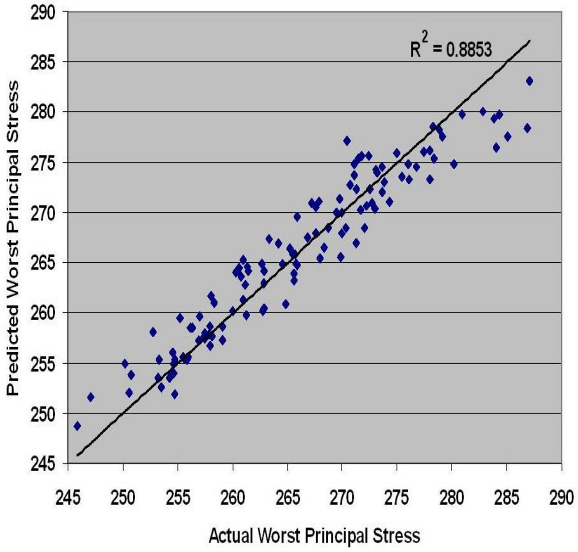

Figure 6.8: Correlation plot for the predicted vs. actual values of nodal worst principal stress for the 12 variables - 120 blade data.

Going back to the simplifications adopted for the 18-variable 200-blade data, surrogates were generated for predicting the nodal life and nodal worst principal stresses. Correlation plots obtained from these metamodels are shown in Figures 6.7 and 6.8. Even though the R^2 values look much better for these plots, the scatter in the points is still not acceptable especially because the variations sought in $Rfact$ are very small in magnitude. Referring back to Chapter 5, it was observed that the mean life of the probable manufactured turbine blades was 1.424 which is around 1.7% lower relative to the nominal life of 1.448 for which these blades were designed. Looking at the scatter of points in Figures 6.7 and 6.8, prediction errors of this magnitude are highly undesirable especially when accuracy upto the third decimal place is sought.

There is no doubt that if the RSMs had given more reliable predictions for the turbine blade problem, it would have saved a lot of computational effort and time. However, the use of multiple surrogates has the following disadvantages :

- Errors from the four different RSMs predicting the effects of control point movements in Planes 4-7 on the output would have accumulated in the final calculated response value adding to the unreliability of the surrogate models.
- Executing free-form deformations on the core by moving the control points on one plane at a time would not have accounted for the interaction effects observed when moving all the control points together. As noted before in Chapter 4 Section 4.3, displacement of the control point at one plane may also result in some form of relatively lesser deformation of the core at the adjacent plane. This, however, may not apply to cases where the control point planes are sufficiently far apart (which is not true for our problem). For such cases, the proposed approach may actually prove useful subject to the condition that a reliable RSM is produced.
- Due to the high dimensionality of the present problem (further reduction in dimensionality being impractical), the large number of the initial design points required for kriging was undesirable. 134 points were explored to generate the first set of 120 design points. If the effects of movements in Planes 5-7 were also to be explored, similar datasets would be required for each plane separately adding to the computational costs.

A detailed description of the various reasons due to which it may become difficult to generate RSMs for complicated problems is given in the recent work of Loeppky, Sacks and Welch [117]. Failure of the various RSM techniques for predicting fatigue life has been noticed before in the work of Rao [118]. The probable causes of failure to generate surrogate models for the present problem may be the high dimensionality of the problem and the erratic behaviour of the code in the design space. It has already been stated before that in order to obtain the output values for 200 design points, around 500 points were sampled from the design space due to the low success rate of the code. This implies that the design space is not uniformly sampled since the regions where the code fails remain unexplored. In such cases, it may be extremely difficult to generate reliable RSMs even when large sample sizes are used for generating the surrogate models.

In the end, the response surface modeling studies presented in this section lead to the conclusion that for the present problem, it is better to stick to the full computational model for a more realistic representation and more accurate estimation of the desired output values. A summary of this discussion is presented in the following section.

6.6 Summary

Kriging in combination with the LP$_\tau$ DOE technique was used for generating RSMs for the turbine blade problem. In addition to the original more complicated problem of modeling the relationship between the 18 thickness values and the output values of life, simpler variants of this problem were tried with the objective of obtaining more reliable surrogate models. Cross-validation using the leave-one-out method indicated that kriging was not able to model the data very well, resulting in unacceptable scatter in the correlation plots. The studies conducted in this chapter help us conclude that realistic and more accurate solutions for the present problem would be obtained by using the computational models directly while replacing them with RSMs is not helpful in this case.

Chapter 7

Robust Design of Turbine Blades against Manufacturing Variability

This chapter presents a detailed description of the methodology used for the direct robust design optimization of turbine blades against manufacturing variability. The series of methodologies proposed in Chapters 3, 4 and 5 are all knitted together and integrated into an iSIGHT workflow that takes a nominal design and returns the mean life and standard deviation in life for this design. This workflow is further integrated with an existing iSIGHT workflow that changes the basic core design of the turbine blades with aid from the CAD and FEA tools and performs a deterministic analysis to predict the nominal life for each new design. The overall integrated workflow uses a combination of design and analysis tools, including, CAD, MATLAB, FFD, CADFIX, FEA and JAVA. The driver of this workflow is the nondominated sorting genetic algorithm (NSGA-II) which is used to implement a tri-objective optimization with the aim of maximizing the nominal and mean lives and minimizing the standard deviation in life. The results obtained from the multiobjective optimization are analysed using 3-d Pareto front plots and the selected robust-optimal solution is compared with the optimal deterministic design and the starting/base geometry.

The organization of this chapter is as follows : Section 7.1 expresses the need for robust design studies in aerospace design engineering. Section 7.2 gives a brief overview of the existing robust design approaches and formulates the current problem as a multiobjective robust design optimization problem. Section 7.3 discusses the application of NSGA-II for multiobjective optimization. Section 7.4 presents a detailed description of the methodology implemented for seeking a robust solution in the context of the current problem. A detailed description of the iSIGHT workflow used for the present problem and the results of the robust design study are presented in Section 7.5. The main inferences from the study are summarized in Section 7.6.

7.1 Need for Robust Design

Traditional procedures for aerospace design are based on a combination of factors of safety and knockdown factors. These procedures have several shortcomings, e.g., they are difficult to apply to new designs with unconventional configurations, they do not provide any measures of consistency in performance, they usually lead to overdesigning of the components resulting in excessive weight, etc. [6]. One of the early approaches designed to improve manufacturing processes and eliminate defects was the *Six Sigma* method which has been widely employed by many companies including Motorola, General Electric (GE), Honeywell, etc. [119]. Most of the existing design optimization procedures in the aerospace industry are focused on improving the nominal performance of the system using deterministic design. This may lead to optimized solutions that have good nominal performance but poor off-design characteristics.

It has been repeatedly discussed in the previous chapters that manufacturing variability inevitably leads to geometric variations in the manufactured parts from their design intent. This geometric variability may lead to inappropriate lifing characteristics during operation, subsequently leading to company losses. The earlier we are able to quantify and reduce the effects of these variations in the design cycle, the better. The estimation of these variations and relative insensitivity to their presence becomes even more important for aircraft engine manufacturing companies because of the huge amounts of money involved in each new engine design and manufacture. This leads to the need for the inclusion of *robust design* methodologies in the current design process. The robust design approach seeks a design that is relatively insensitive to uncontrollable sources of variation present in the system's environment [120]. Although robust design methods are recently gaining popularity in the aerospace design community [6, 121, 79, 122, 123], they are not always used in the industry due to the following reasons :

- the industry feels more comfortable with traditional deterministic design approaches,
- robust design methods are quite complex and computationally expensive, and

- techniques for obtaining realistic estimations of manufacturing variability are still in their development stages [6].

However, if realistic estimates of the sources and nature of manufacturing variations, and, simulation models with acceptable accuracy, are available, the benefits of robust design methodologies can be realized in :

- minimizing the variations in overall performance and lifing characteristics,
- reducing the maintenance costs during operation,
- increasing the confidence in design analysis tools, and
- reducing the design cycle time and cost [6].

In the present problem, probabilistic estimates of the effects of manufacturing variability on turbine blade life were available. The methodologies used for estimating the probable mean life and standard deviation in life for blades manufactured over a year have already been presented in Chapters 3, 4 and 5. It was, therefore, desirable to apply these techniques for robust design studies in search of a better turbine blade design with improved mean and nominal lives and reduced value of standard deviation in life. The methodology implemented for robust design optimization is discussed in detail in Section 7.4 and its benefits with respect to the current problem are highlighted in Section 7.5.

7.2 Robust Design Methods

7.2.1 Overview

The term *robust parameter design* was coined by Genichi Taguchi to describe an approach to industrial problem solving that may be employed for reducing product variability in the presence of environmental sources of variation [124]. Taguchi envisioned a three-stage process of, *system design*, *parameter design* and *tolerance design*, for design optimization [125]. System design is used to determine the feasible design space for the optimization problem. The parameter design stage involves reduction of variability in the product performance by choosing levels of the control factors (design variables) that make the product relatively insensitive to changes in the noise factors [124]. *Noise factors* represent the effects of various sources of variation that are difficult or expensive to control, e.g., changes in the surrounding temperature and humidity levels, wear and tear of tools in the manufacturing process, changes in properties of raw materials, etc. *Control factors* represent the design variables that the designer is free to manipulate [79]. The parameter design stage is also popularly known as *robust design* optimization. The optimal design obtained from this stage can be fine-tuned by the application of *tolerance design* approaches such that the desired performance requirements are met by adjusting the lower and upper design tolerance values. Some examples of the application of tolerance design to turbine and fan blades are available in the cited literature [2, 126]. Eliminating products which fail to meet the tolerance design specifications is carried out at the production stage, and hence, is relatively expensive. This leads to the gaining popularity of robust design methods.

Although Taguchi's design philosophy is widely applied and appreciated [120, 123, 127], the benefits and efficacy of his techniques have always been a subject of debate [128, 129, 125]. Welch et al. [130] pointed out that the number of experimental runs required for Taguchi's "inner-outer" array experiment are prohibitively expensive and proposed a "combined array" approach to overcome this limitation. Shoemaker et al. [129] also supported the combined array approach and highlighted that Taguchi's "product array" approach requires a large number of runs, is unable to perform well for non-linear functions, and does not allow estimation of control factor interactions. Box and Jones [131] and Myers et al. [132] suggested the use of response surface modeling techniques as alternatives to the Taguchi parameter design approach. These techniques, are however, only as accurate as the response surface models. This was followed by the application of statistical approaches for robust design optimization. Huyse and Lewis [133] identified the risk associated with a particular design as the expected value of the perceived loss, and the best design was chosen such that the overall risk was minimized. Ben-Tal and Nemirovski [134] proposed the optimal minmax approach which minimizes the worst-case compliance. It was subsequently argued that the minmax optimization methods are too conservative because they are formulated to prevent against the worst-case scenarios [125]. In contrast, the Bayes' decision principle used by Huyse and Lewis [133] is essentially concerned with the average-case performance since only the mean objective is minimized [79]. Recently, the concept of probabilistic robustness has been introduced that takes the probability distribution and probability density into account in order to search for the optimal solution that satisfies the design requirements in maximal probability [135]. A comprehensive survey of the state-of-the-art in robust design optimization can be found in the recent work of Beyer and Sendhoff [136].

7.2.2 Robust Design using Multiobjective Optimization

A central issue in robust design study is choosing the objectives, or robustness metrics, to be used during the optimization process. Early attempts at finding robust solutions were aimed at minimizing only one objective, i.e., either the expectation of the output function in its neighbourhood (mean value) [137, 138], or the variance in the output function [139]. Garzon [10] explored two approaches for obtaining robust optimal solutions. In the first approach, he minimized the mean value of the loss function. The target of the second approach was to minimize the variability in loss function with mean loss as a constraint. Das [140] pointed out the drawbacks of choosing only the mean or only the variance of a function as the robustness metric. Choosing only the mean may result in cancelling the positive and negative deviations in the value of the function around a target value and hence result in a non-robust solution. Choosing only the variance may lead to a design with reduced variability but poor performance characteristics. Therefore, Das [140] proposed bi-objective formulations for the robust optimization problems such that trade-offs between 'optimality' and 'robustness' could be achieved. The three possible combinations of objective functions that he suggested are:

- expectation of the function (mean) and variance,
- expectation of the function (mean) and its original value (nominal), and
- original value of the function (nominal) and variance.

Das [140] himself preferred to use the combination of mean and nominal values of the output function for trade-off analysis. Many recent works have used the mean and standard deviation as objective functions for robust design problems [141, 142, 143, 144]. Keane [110] compares several optimization strategies for robust design of turbine blade airfoils. He demonstrates that although using the mean value of the output function yields better results than the deterministic optimal solution, the results obtained from a bi-objective optimization of standard deviation vs. mean lead to significantly more robust solutions.

In the present research, two robustness metrics,i.e., mean life and standard deviation in life were traded-off against nominal life. The usage of three objectives for trade-off analysis has been employed before in the work of Das [140] where violation of soft inequalities was used as the third objective along with the mean and nominal function values. Since the beginning of our discussion on the present problem, it has been argued that the nominal life may not represent the actual life of the components coming out of the manufacturing process. (Note: A probabilistic representation of the lifing distribution for the manufactured blades under consideration is shown in Chapter 5, Figure 5.6.) However, the value of nominal life holds great importance from an industrial perspective since most of the design specifications are based on this value. Out of our three objective functions, the interest of the design and manufacturing engineers is captured more by the nominal life since most of their assumptions are based on the deterministic analysis of new designs. Besides, using the mean function value may (in some cases) lead to slightly incorrect estimations. For example, in the present case, the value of mean life may be underestimated if any of the 42 perturbations due to manufacturing variability fail during the FEA. This may also lead to underestimating the standard deviation, however, this can be countered by adding a penalty value for every failed mesh when the designs are studied. Therefore, it becomes clear that using the nominal value for robust design optimization provides with at least one consistent robustness metric. At the same time, the value of mean life cannot be ignored since it represents the probable actual value of average life for the turbine blades. Assuming that most of the 42 perturbed geometries considered here are successful through the FEA process, a design for which the mean life deviates too much from the nominal life may not be preferable. Also, leaving out the standard deviation may not be recommended when the aim is to obtain significant improvements in robustness. Using three objectives for the robust design search was considered even more desirable for the present problem since the tri-objective formulation did not add to the computational cost. Even if the nominal life was not set up as an objective function, the nominal designs were still required for computing the mean and standard deviation (*std*). In addition, a check on the nominal life was imposed in the integrated iSIGHT workflow, such that, the mean and standard deviation in life were calculated only for the designs that satisfied a minimum acceptability criterion. A detailed description of this analysis and its results will be presented further in Sections 7.4 and 7.5, respectively.

The concept of trade-off between mean, nominal and *std* can be explained in more detail with the help of Figure 7.1. Let us assume that $\mathbf{x}$ is a vector of design variables that varies in the range $\Delta\mathbf{x}$ due to the associated noise. Now, let $\mathrm{f}(\mathbf{x})$ be our output function of interest, defined by the curve shown in Figure 7.1, such that a maximum value of this function is desirable.

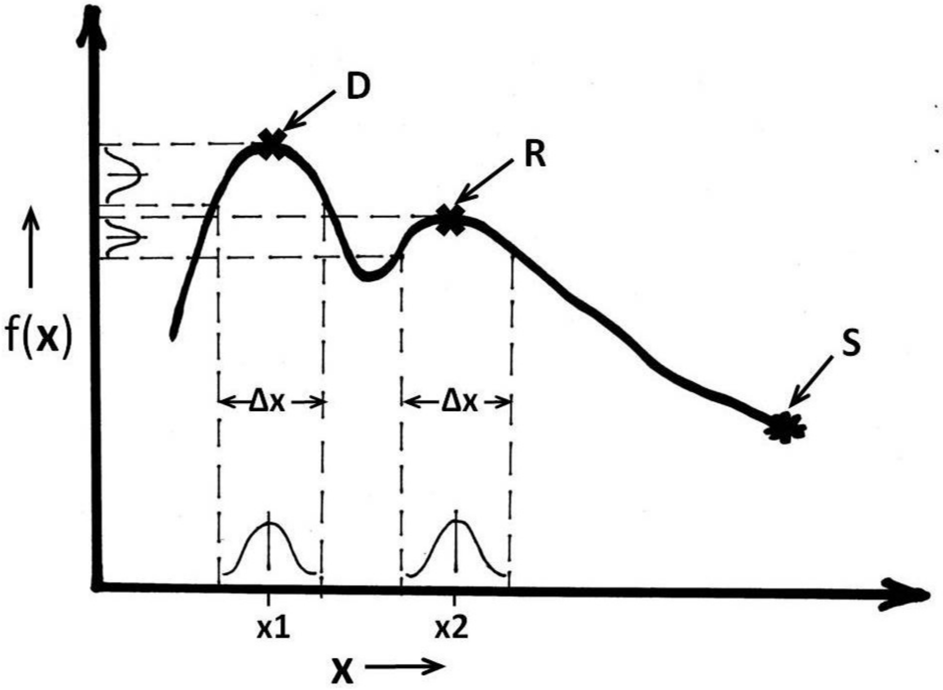

Figure 7.1: A comparison of robust design (Point R) with the optimal deterministic design (Point D).

Point S in the figure represents the starting point, Point D represents the deterministic optimal solution obtained by maximizing the nominal value of f($\mathbf{x}$), and, Point R represents the optimal robust solution. As we can see in the figure, the best mean and nominal values of f($\mathbf{x}$) are observed at point D. But, any noise in the parameter values at **x1** result in much larger variability in the function f($\mathbf{x}$) at this point, which is highly undesirable. In contrast, a slight compromise in the mean and nominal values of f($\mathbf{x}$) by selecting the parameter setting at **x2** may result in a more robust solution at Point R with reduced variability in the output function. Note that in the example shown in Figure 7.1, the nominal value of f($\mathbf{x}$) is assumed to be a part of the observed distribution of f($\mathbf{x}$) when the effects of noise factors are added. Thus, mean and nominal values do not appear to be in much competition. However, this was done for ease of illustration, and in reality, this may or may not be true. Noticeable differences between the mean and nominal values of a function may be observed in cases where the noise factors lead to either positive or negative shifts in the output distribution as a whole, or, in cases where the distribution is skewed or asymmetric.

7.3 Nondominated Sorting Genetic Algorithm (NSGA-II)

The preceding section discussed the formulation of the robust design problem as a multiobjective optimization problem. The presence of multiple objectives in a problem give rise to multiple solutions, also known as the Pareto-optimal set. By Pareto-optimal set, we mean a set of solutions where no one solution is superior to any other, i.e., all solutions are *non-dominated.* In other words, for a point that lies on the Pareto front, improvement in the value of one objective function cannot be attained without worsening the value of atleast one of the remaining objective functions.

One of the classical methods used for multiobjective optimization is the weighted-sum approach. According to this approach, a weighted sum of all the objectives is minimized using single objective optimization and the optimal solution, thus obtained, becomes a part of the Pareto set. This process is repeated for different settings of the weights until a sufficient number of Pareto-optimal points are generated. The major drawbacks of this method are :

- it is computationally expensive,
- it succeeds in getting points from the Pareto front only when the Pareto curve is convex, and
- even for a convex Pareto curve, an even spread of weights does not produce an even spread of points on the curve [145].

In contrast, genetic algorithms (GAs) work with a population of solutions. Therefore, a single run of a multiobjective GA may result in capturing a number of Pareto-optimal solutions. This property of GAs makes them naturally suited to solving multiobjective optimization problems [146]. Schaffer [147] was probably the first to recognize the possibility of using GAs in search of multiple non-dominated solutions and proposed an approach called the Vector Evaluated Genetic Algorithm (VEGA). However, VEGA usually leads to finding the extreme points on the Pareto front for which one objective function is optimal at a time[148]. Following the VEGA approach, several multiobjective evolutionary algorithms were developed, e.g., Multiple Objective Genetic Algorithms (MOGA) [149], Niched Pareto Genetic Algorithm (NPGA) [148], Nondominated Sorting Genetic Algorithm (NSGA) [18], etc. An overview of these techniques can be found in the cited literature [150, 151, 79].

The elitism based Nondominated Sorting Genetic Algorithm (NSGA-II) proposed by Deb et al. in 2002 [18] is used for the present problem. The NSGA-II uses a fast nondominated sorting procedure that requires $O(MN^2)$ computations, where M is the number of objectives and N is the population size. In addition, it replaces the sharing function approach with a crowded-comparison approach that does not require any user-defined parameter for maintaining diversity among population members. Numerous instances of the successful application of NSGA-II for robust design studies are available in the literature [1, 79, 110, 118, 152].

7.4 Methodology

A simplistic flowchart representation of the methodology adopted for the robust design optimization of turbine blades is shown in Figure 7.2. As discussed before in Section 7.3, the NSGA-II optimizer is employed for the present problem with the objective of maximizing the nominal life and mean life and minimizing the standard deviation (*std*) in life. With no changes to the external blade geometry, a combination of CAD and FFD tools is employed for modifying the core shape and position in order to changing the design of the turbine blade. The position of the core is allowed four degrees of freedom in the form of translation and rotation

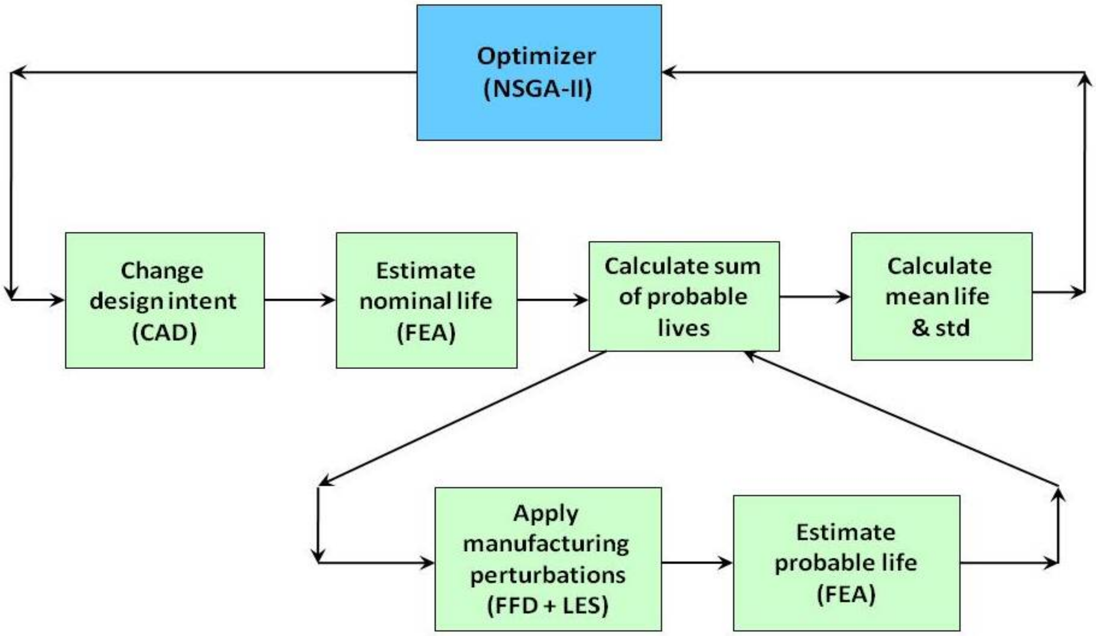

Figure 7.2: A simplistic flowchart representation of the robust design methodology adopted for the turbine blade problem.

around the X- and Y-axis. The shape of the core is governed by a further set of 18 FFD control points that are allowed to move in the **X** and **Y** directions. This results in $18 \times 2 = 36$ variables controlling the core shape. In combination, we have a total of $36 + 4 = 40$ variables defining the core position and shape for each new nominal design.

The effects of translating the core in the positive and negative directions along the X- and Y-axis are shown in Figure 7.3. As can be observed in Figure 7.3(a), translating the core in the positive **X** direction shifts it towards the trailing edge (TE), and translating the core in the negative **X** direction produces a shift towards the leading edge (LE). Figure 7.3(b) shows that a translation along the positive **Y** direction shifts the core towards the pressure surface (PS), and, translating the core in the negative **Y** direction produces a shift towards the suction surface (SS). Similarly, rotating the core around the X-axis in the positive direction causes an incremental shift in the core towards the SS, while rotating the core in the negative **X** direction

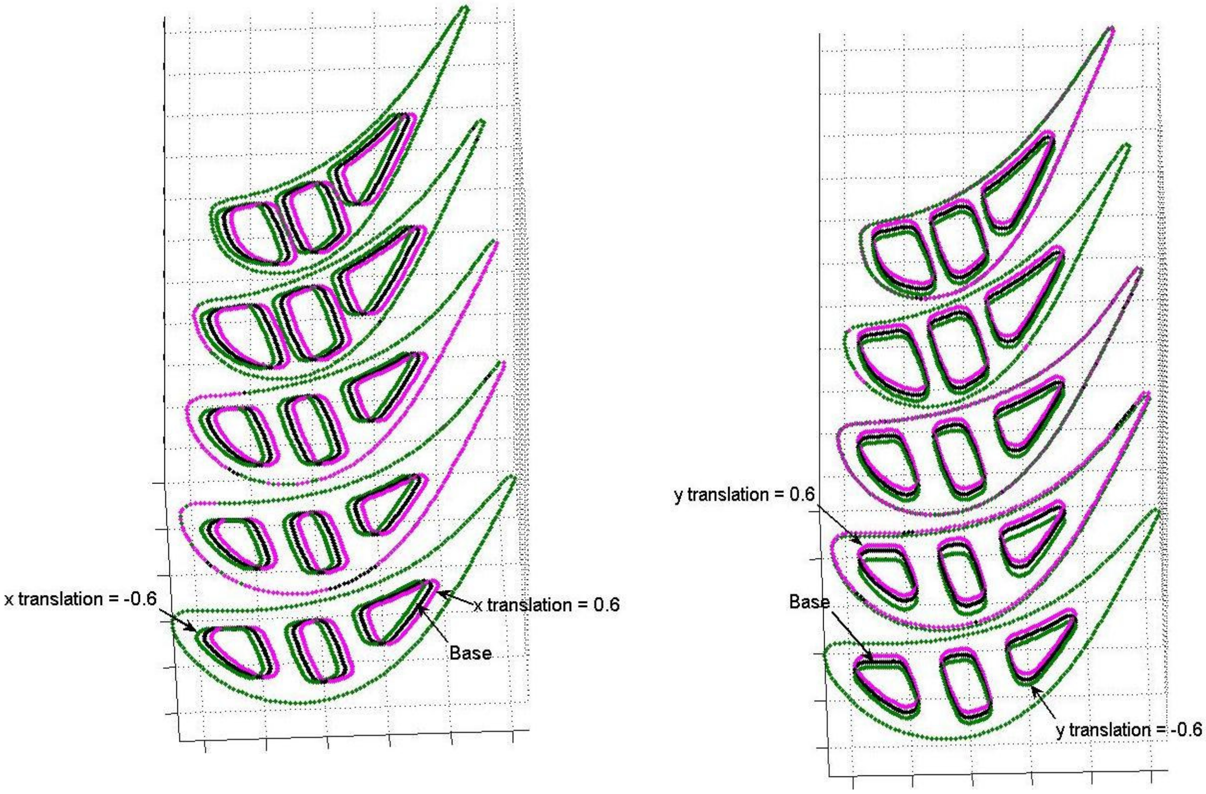

(a) (b)

Figure 7.3: Shift in the core position relative to the base design when the core is translated along the (a) X-axis, and (b) Y-axis, by ±0.6 units.

causes the core to shift towards the PS. A positive rotation around the Y-axis results in an incremental shift in the core towards the TE, while a negative rotation causes the core to shift towards the LE. The term incremental shift has been used because the deviations of the core from the base profile increase from the top (Tip) end towards the bottom (Root) end since the centre of rotation is located at the tip of the blade. This is done in alliance with the fact that the tip end of the blade is fixed when the molten metal is pumped into the casts during blade manufacture (refer Chapter2, Section 2.1).

The effects of changing the core shape using FFD control points have already been discussed in great detail in Chapter 4. However, the major difference while using FFD for changing the design as opposed to modeling manufacturing variations is that the base core is enclosed by 5 lattice control point (lcp) planes along the Z-axis. Out of these 5 planes, the control points on the 3 central planes are allowed to move along the X- and Y-axis. This introduces relatively more global deformations as compared to the 8 lattice control point structure that was used in Chapter 4 for simulating the effects of manufacturing variations.

The 40 variables defining the core shape and position are repeatedly altered by the optimizer to produce a new nominal design for each run of the integrated workflow. A volume mesh on this nominal design is created by the FEA tool and analysed for estimating the nominal life. This mesh is then transferred to a subflow that applies the FFD based deformations and LES based mesh morphing repeatedly to the nominal mesh in order to generate the 42 probable manufactured blade shapes for which the probable values of life are calculated. The mean of these probable lives represents the mean life and the standard deviation of these values is a representative of the blade life variability. Detailed descriptions of the application of FFD and LES based methodologies for simulating the effects of manufacturing variability have already been provided in Chapters 4 and 5, respectively. Here, an important point to note is that while the core is enclosed by 5 FFD lcp planes along the Z-axis to change the design intent, 8 lcp planes are used along the same axis for applying the manufacturing perturbations. As stated before, this ensures that the deformations involved in changing the nominal design are relatively more global in nature as compared to the effects of manufacturing variations. The delta values of the manufacturing perturbations to be applied on each new nominal design are obtained by calculating the difference between the nominal thicknesses for the original nominal design considered in Chapter 5 and the 42 sets of thickness values obtained from the measurement data analysis. In the end, the mean and standard deviation of the 42 probable lives are passed on to the optimizer along with the value of nominal life for the optimization process. Finally, the entire set of designs explored by the NSGA-II algorithm are plotted in the objective function space and the Pareto-optimal set is identified for trade-off analysis.

7.5 Robust Design Optimization of Turbine Blades

This section presents a detailed description of the numerical studies conducted for the present problem. The integrated workflow used for robust design optimization of turbine blades is presented in Section 7.5.1. Parts of the workflow are zoomed in and details of the working of each component are explained in Appendix C, Sections C.1 and C.2. The results of the deterministic optimization are presented in Section 7.5.2. In the end, the results of the robust design study are plotted in the objective function space and the Pareto-optimal designs are identified in Section 7.5.3. The geometric differences between the base design, the optimal deterministic design and the Pareto-optimal designs are also analysed. The selected robust solution is compared with the base design for any shifts in the critical region or changes in the stress distribution.

In the discussions that follow, the *base* design refers to the nominal turbine blade design that is used as the starting point for the robust design study. The design of the blade is changed by modifying the core shape and position for this base design in order to produce new *nominal* designs for each run. The term *std* refers to the standard deviation in blade life due to the effects of manufacturing variability on each of the new nominal designs.

7.5.1 Integrated Robust Design Workflow

As per the methodology discussed in Section 7.4, the integrated robust design workflow (IRDW) employed for the turbine blade problem is shown in Figure 7.4. The zoomed in views of the IRDW can be seen in Apppendix C, Figures C.1 and C.2. This workflow was created in iSIGHT version 3.5-1 [15]. The NSGA-II optimizer available in the OPTIONS package [116] was used for multiobjective optimization. As discussed before in Sections 7.3 and 7.4, the aim of the optimizaton process was to maximize the mean and nominal lives and minimize the standard deviation. The OPTIONS-NSGA2 package is formulated, such that it minimizes all the objectives in a multiobjective optimization loop. Therefore, negative values of the nominal and mean lives were passed onto the optimizer as objective function values and it was set to

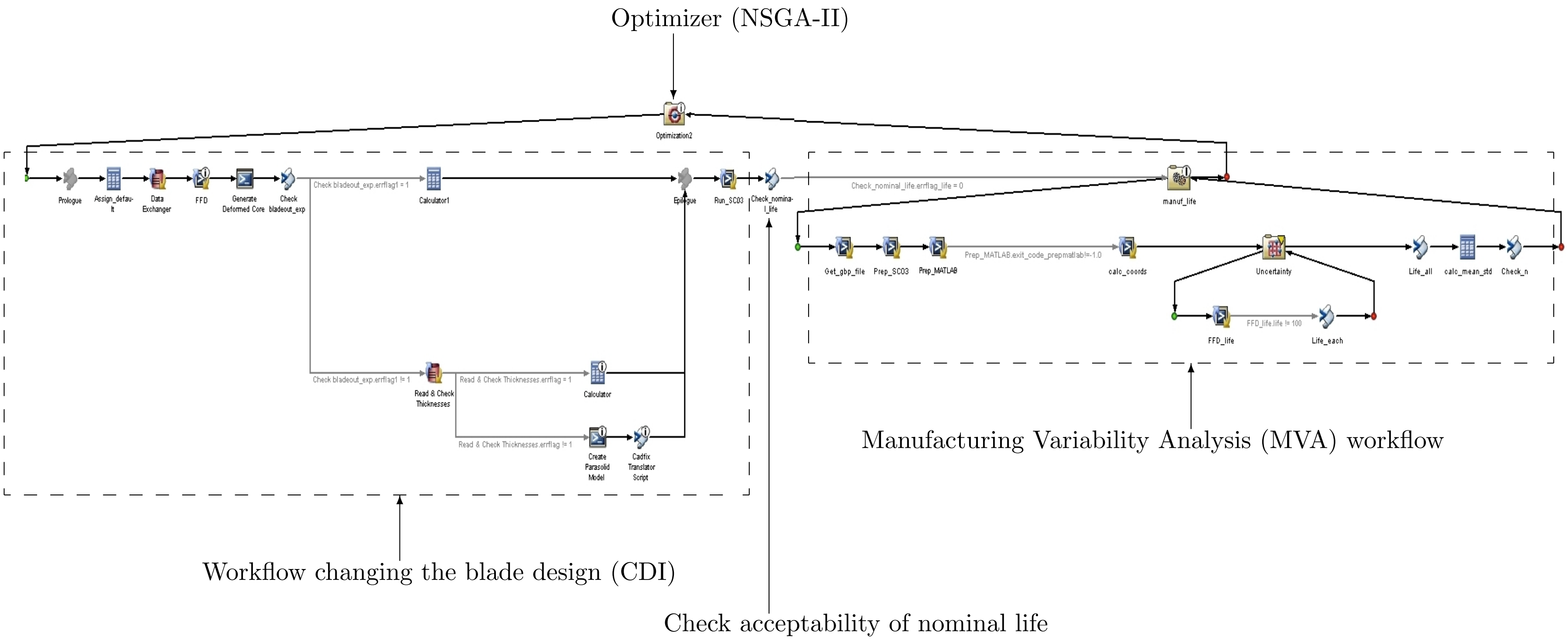

Figure 7.4: Integrated workflow changing the design intent of the turbine blade and estimating the effects of manufacturing variability for robust design optimization.

minimize all the three objective functions.

In Figure 7.4, dashed boxes have been used to demarcate the parts of the integrated workflow changing the design (CDI), and that performing the manufacturing variability analysis (MVA). The FE analysis for generating the mesh on the nominal turbine blade and estimating the value of life for this blade was executed on a single node of a computer cluster with dual Intel quad core processors, 2.8 GHz clock rate and 32GB RAM/node using 8 processes in parallel. Similarly, the FE runs for the LES based mesh morphing and lifing calculations on the 42 perturbed geometries were executed on the same computer cluster using 42 nodes in parallel. All the remaining components of the workflow were executed on a Intel 2 Quad Core machine with 2.8 GHz clock rate and 8GB RAM. Adding up the total time taken for the execution of all these processes, each run of the IRDW for a new design took around 35-40 minutes using a 10 node tetrahedral mesh size of around 45,351 elements and 76,841 nodes. Note that, a coarser mesh was used for the present study in order to save the computation time required for each run. An example of this mesh is shown in Figure 7.5. It has already been discussed in Chapter 5 Section 5.3, that a mesh size of around 80,000 elements is more appropriate for obtaining more accurate results on the turbine blade models. However, it was considered impractical to use larger mesh sizes for the robust design study because an increase in the mesh size would make the computational time prohibitively expensive. The main purpose of the present study was to prove that the proposed robust design methodology works for the turbine blade problem. Hence, a trade-off between accuracy and computational time was deemed necessary. It was also discussed in Chapter 6 that it is much more desirable to use RSMs in order to save the computational cost. However,

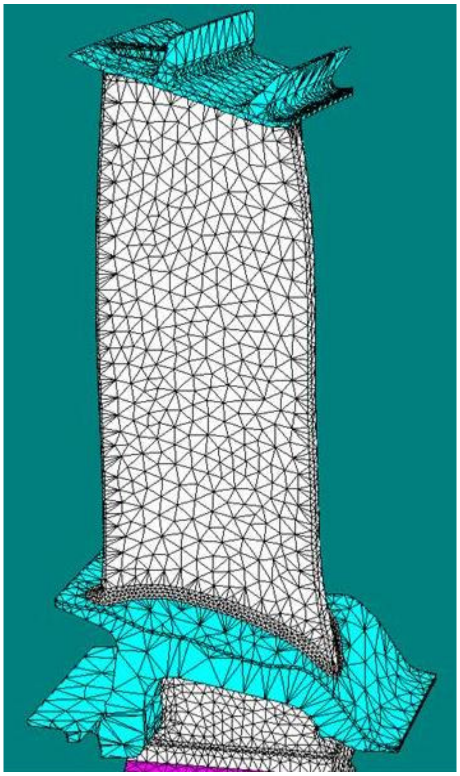

Figure 7.5: A 45,351 element 10 node tetrahedral mesh created on the turbine blade model.

the results of the RSM studies presented in Section 6.5 clearly indicated that using RSMs in lieu of FE models was not an option in the present case.

A check was imposed upon the nominal life of the turbine blade model between the CDI and MVA workflows. The component implementing this check is marked in Figure 7.4. Only those designs that possessed a value of $Rfact \geq 1.2$ were allowed to pass on to the MVA workflow. This check was imposed in order to avoid unnecessary computations on uninteresting designs. The nominal life for the base design estimated from the coarser mesh was around 1.282. Any designs that demonstrated a value of $Rfact$ a lot worse that this value were assumed to be uninteresting for the designer. A detailed description of the working of each component in the CDI and MVA workflows is given in Appendix C, Sections C.1 and C.2.

7.5.2 Optimal Deterministic Design

Before moving on to the robust design study, it is essential to understand the benefits offered by a standard design optimization strategy wherein only the nominal performance is optimized. Since the effect of manufacturing perturbations is not taken into account during deterministic optimization, it is expected that the optimal design obtained from this study may lead to poor off-design characteristics. In order to investigate this further, a single objective optimization was performed for the turbine blade problem using negative values of nominal life as objective function values. The negative values were sent to the optimizer with the aim of minimizing the objective function which in turn would lead to maximizing the nominal life. The genetic algorithm (GA) available in the OPTIONS package [116] was employed as the optimizer for the present study. The CDI workflow was set to run for 10 generations, with a population size of 101 in each generation. However, convergence in the objective function values was observed much before the completion of the scheduled 10 generations. Although the workflow was stopped at the beginning of its eighth generation, the best values of nominal life were observed in the fourth generation itself. A plot showing the nominal $Rfact$ vs. the explored design number obtained from GA is shown in Figure 7.6. The point showing the best nominal life is marked as *Optimum point* in the figure. The nominal life for the base design, which was also used as the starting point for the present study, was around 1.282. The nominal life observed for the optimal deterministic design was approximately 1.342, which implies an improvement of about 4.68% relative to the base design. This was highly desirable. However, it was observed that 17 out of the 42 perturbations failed for the *Optimum point* because the core protruded

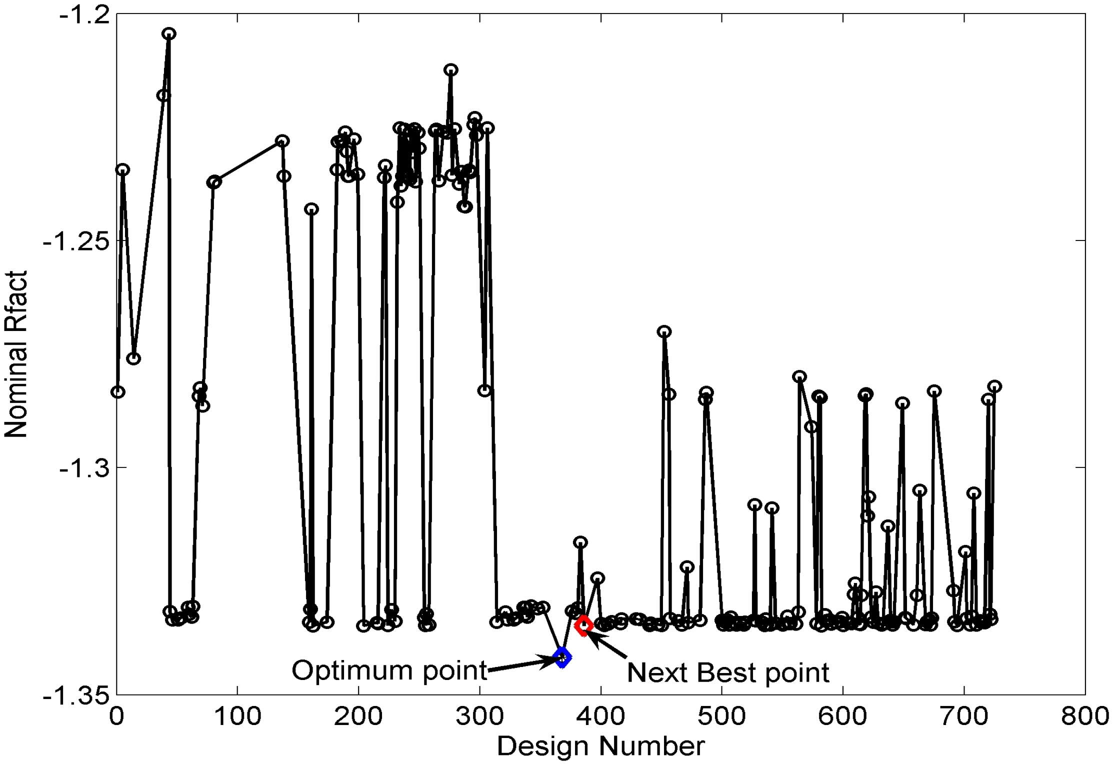

Figure 7.6: A plot showing the nominal life vs. explored design number obtained from GA.

out of the blade surface for these perturbations. Hence, a comparison between the *std* for the base design, and, the value of *std* calculated only from the 25 successful perturbations of the *Optimum point*, was not justified. The fact that most of the cores in the perturbed geometries protruded out of the blade was an indication that the nominal core for the *Optimum point* was too close to the blade surface. This is demonstrated in Figure 7.7(a), which compares the geometries for the base design and the optimal deterministic design. As we can observe in the figure, the core for the optimal deterministic design has moved dangerously close to the external blade airfoil surface at the trailing edge, especially between the Tip and Mid sections.

Following this analysis, the optimal point was rejected and the next best point obtained from the optimization results was considered for comparison. This point is marked in Figure 7.6 as the *next best point* and the geometry for this point is compared with the base design in Figure 7.7(b). As we can observe in Figure 7.7(b), the geometry for the *next best point* looks much more realistic than that for the *Optimum point*. The nominal life obtained from this geometry was around 1.335, which indicates an improvement of around 4.13% relative to the base geometry. The *std* for the base design, without adding any penalties, was around 0.02543.

The *std* calculated for the *next best point* was approximately 0.01026, with 39 out of the 42 perturbed geometries successful through the FEA. Hence, the *std* for the *next best point* was reduced by around 59.65% relative to the base design which was promising.

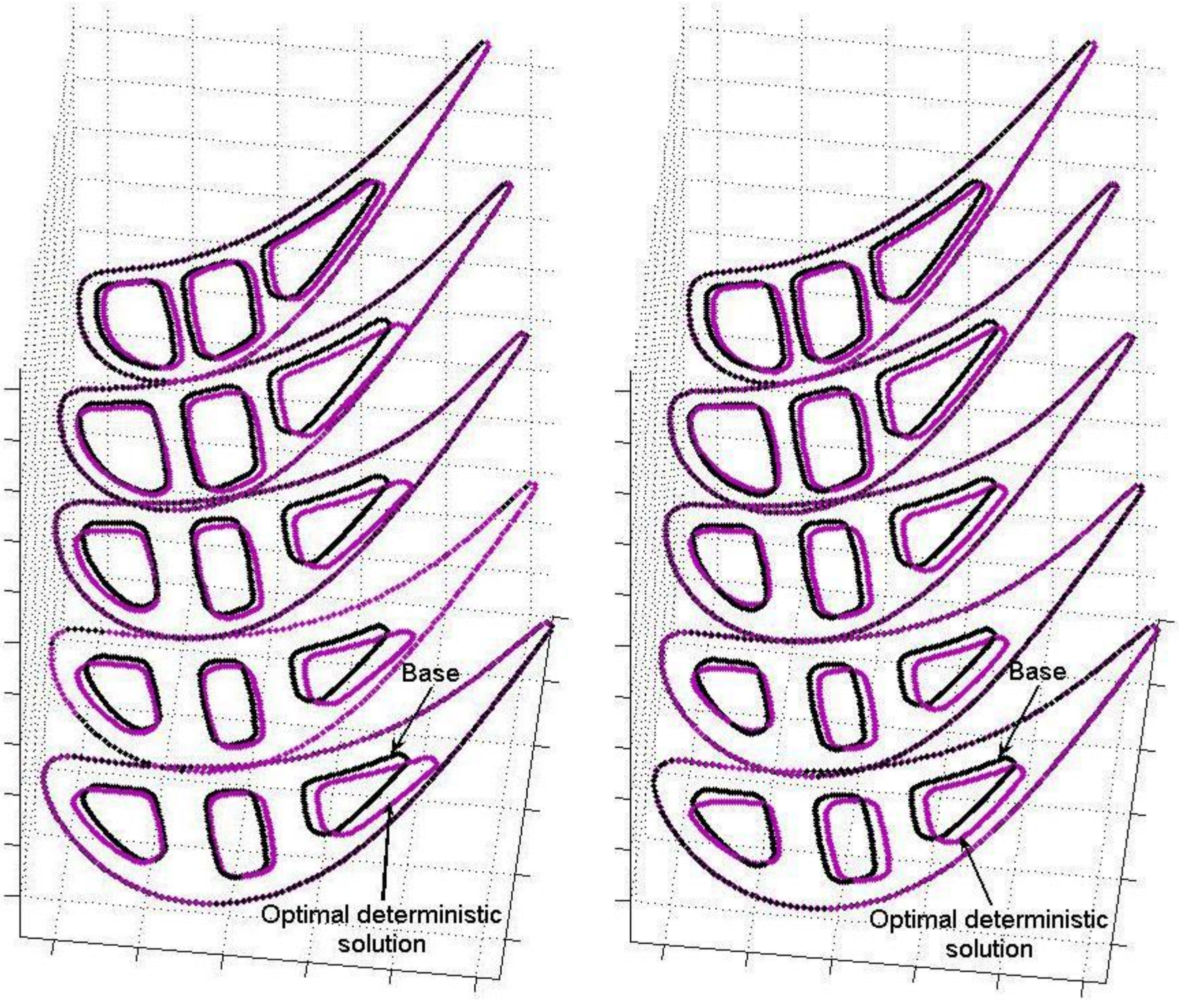

(a) (b)

Figure 7.7: Comparison of the (a) *Optimum point*, and (b) the *next best point*, with the base design.

From the results of the deterministic optimization study, we can conclude that the geometry showing the best nominal life may not necessarily be the best design. In fact, in the present study, the optimal design obtained from the deterministic optimization of turbine blades was most undesirable due to the core deviating too close to the blade surface. As a result, this design could not withstand the perturbations introduced by manufacturing variability. However, the next best design point obtained from the optimization study did show some promise with a good improvement in the nominal life, and, reduced variations in the probable values of life due to manufacturing perturbations. Next, it is appropriate to explore whether the robust design optimization can prove to be of greater benefit for the present problem.

7.5.3 Pareto-optimal Solutions

For the robust design study, the IRDW was set to run for 35 generations with a population size of 101 in each generation. The Pareto-optimal set of points obtained at every generation were compared to check for convergence of the objective function values. The workflow was stopped when no improvements in the Pareto-optimal points were observed. As a result of this study, around 2367 design points were explored by the optimizer. However, due to the high failure rate of the runs, only 741 design points were successful through the entire workflow.

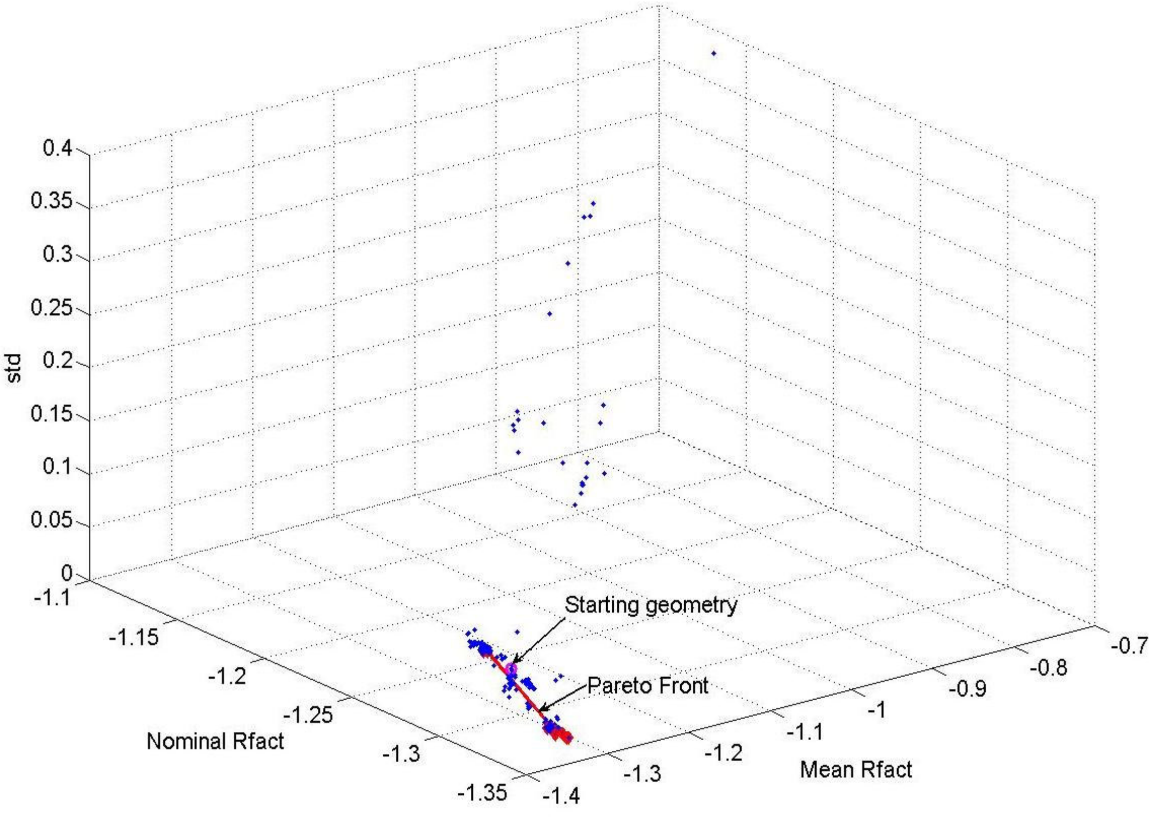

Figure 7.8: A 3-d plot of the successful design points plotted in the objective function space showing the Pareto front.

Most of the design points failed because the automated meshing routine was very sensitive to changes in the nominal geometry, and, because the large deviations in the core resulted in protrusions of the core geometry from the blade surface. The objective function values for the 741 successful design points are plotted in Figure 7.8. A zoomed in view of this plot in the region of interest is shown in Figure 7.9. For ease of trade-off analysis, 2-d views of Figure 7.9 are plotted in Figure 7.10. It was discussed in Section 7.5.1, that the aim of the robust design study was to maximize the mean and nominal lives and minimize the standard deviation in life (*std*). However, the NSGA-II optimizer in the OPTIONS package [116] is formulated, such that, it minimizes all the objectives in a multiobjective optimization process. Therefore, negative values of mean and nominal lives were passed on to the optimizer as objective function values. Hence, the plots in Figures 7.8, 7.9 and 7.10 show the mean and nominal values of $Rfact$ plotted on a negative scale. The more negative these values are, the better are the mean

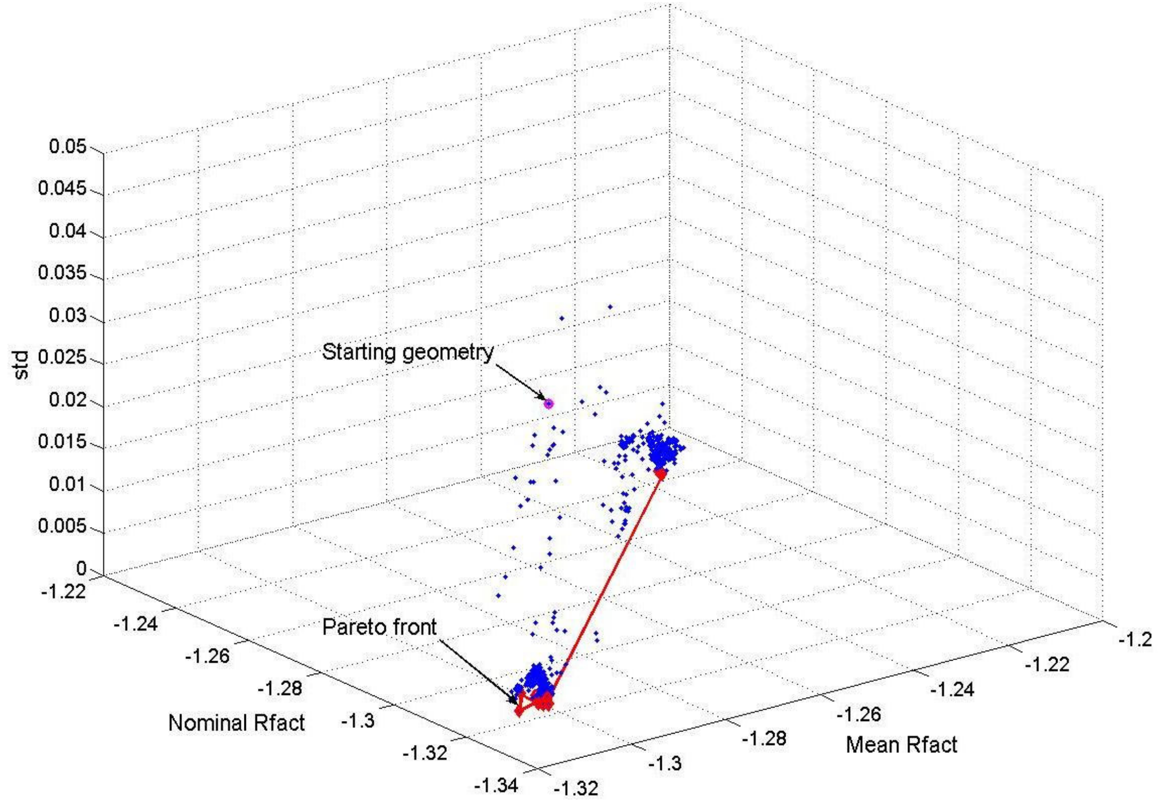

Figure 7.9: A zoomed in view of the plot shown in Figure 7.8 focusing on the region of interest.

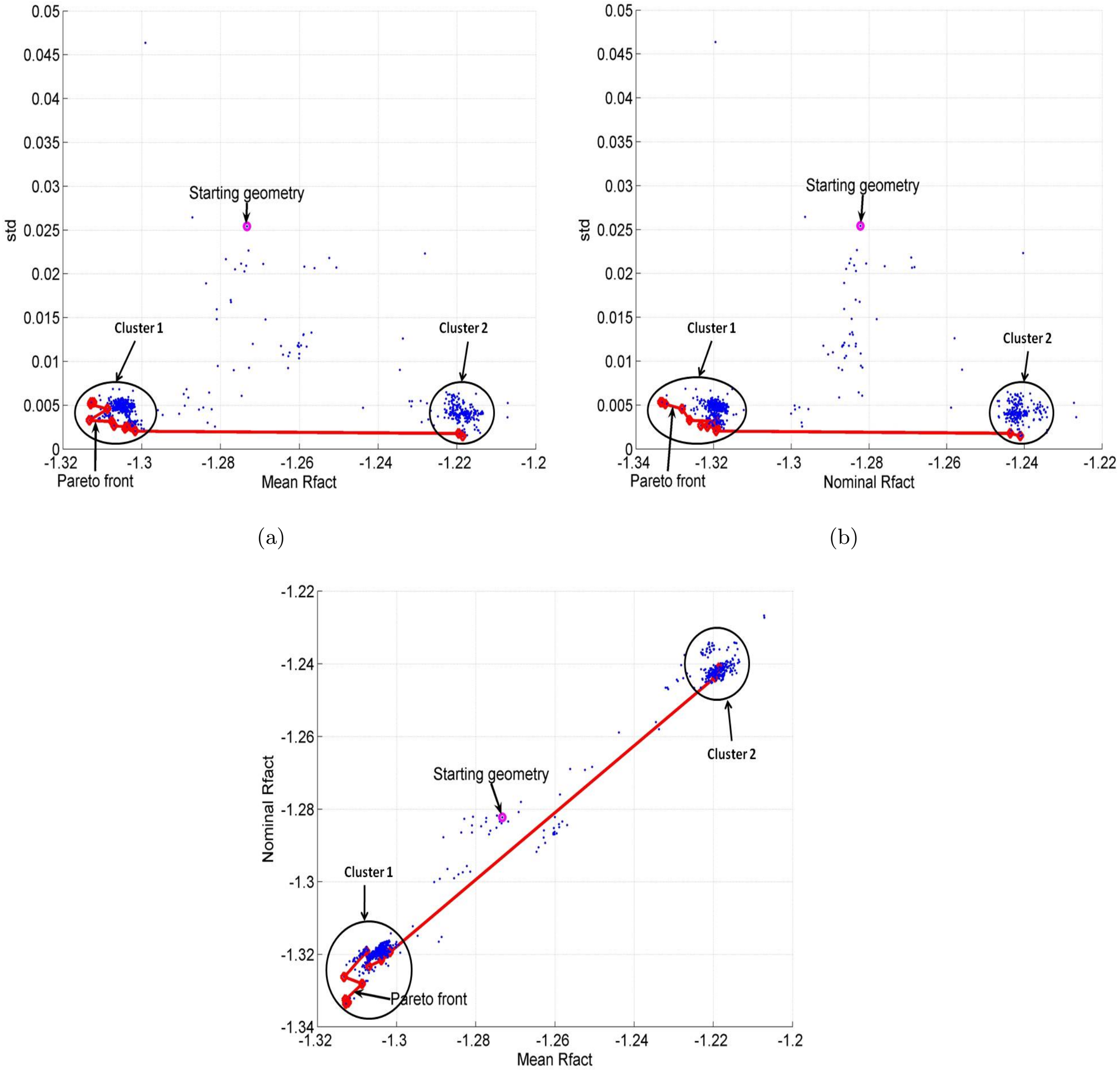

(a)

(b)

(c)

Figure 7.10: Plot of (a) standard deviation vs. mean life, (b) standard deviation vs. nominal life, and (c) nominal life vs. mean life, showing the explored design points along with the Pareto front.

life and nominal life.

Figures 7.9 and 7.10 show that there are two prominent clusters of points in the objective function space. These clusters are marked as Cluster 1 and Cluster 2. The figures also indicate the starting/base design point for the optimization process. The design points constituting both the clusters show marked improvements in standard deviation as compared to the starting geometry. The standard deviation in life for the base design is around 0.02543, whereas, the average value of *std* for the two clusters is around 0.004 which implies an improvement of around 84% relative to the starting design point. Cluster 1 shows much better values of mean and nominal life as compared to the base geometry. On the other hand, the points in Cluster 2 show worse values of mean and nominal life relative to the starting point. The nominal and mean lives for the base geometry were around 1.282 and 1.273, respectively. From Figure 7.10, the points in Cluster 1 show an average mean life of around 1.305 and an average nominal life of around 1.320. On the other hand, Cluster 2 shows an average mean life of around 1.215 and an average nominal life of approximately 1.245.

The observations made so far give an indication that the base geometry can possibly be modified into two new sets of geometries, both giving considerable improvements in standard deviation. One of these sets will improve the nominal and mean lives, whereas, the other set will worsen these values. It is expected that the geometries belonging to the same set will show similar deviations from the base design. However, designs from Cluster 1 when compared with Cluster 2 will be different. This was analysed by picking up a few de-

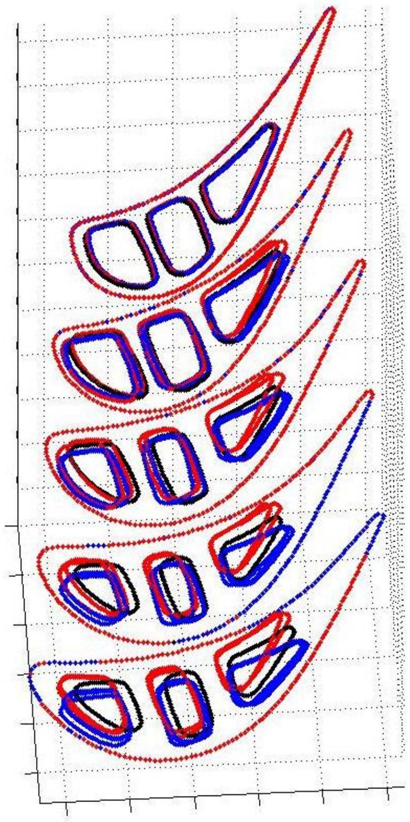

Figure 7.11: A comparison of the nominal designs picked up from Cluster 1 and Cluster 2 with the base geometry.

signs on the Pareto front from both the clusters and comparing them with the starting geometry. It has been discussed before in Section 7.4, that only the core shape and position were modified to bring changes to the nominal design while the external blade geometry was left unchanged. The deviations in the core shape for the designs picked up from the two clusters are compared with the base design in Figure 7.11. The black cross-sections define the base geometry, the blue curves represent the nominal designs picked up from the Pareto front in Cluster 1, and, the red cross-sectional curves mark the nominal geometries picked up from the Pareto front in Cluster 2. As we can observe in the figure, the Tip section for these geometries remains unchanged while significant differences can be noticed at the remaining cross-sections. The core geometries from Cluster 1 tend to drift more towards the suction surface and LE, whereas, the cores from Cluster 2 tend to deviate more towards the pressure surface. The cores

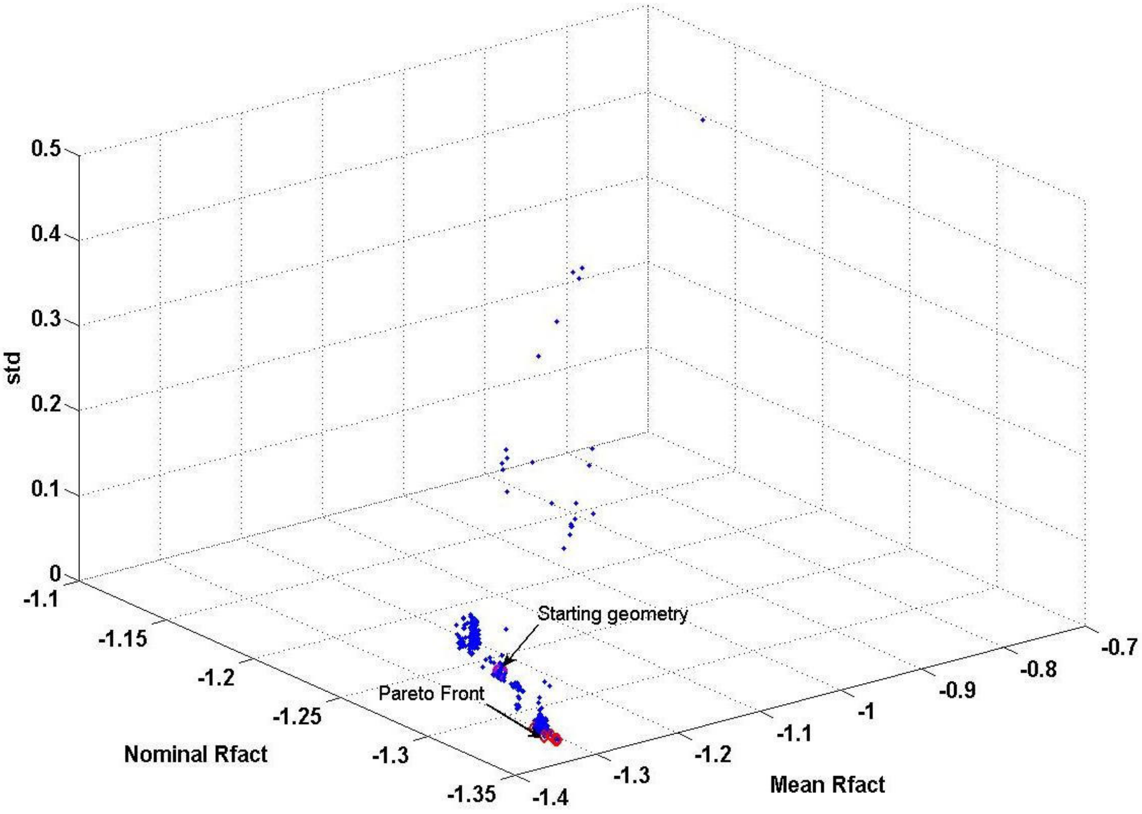

Figure 7.12: A plot of the successful design points explored by the optimizer with penalties added to standard deviation.

constituting Cluster 2 also drift towards the LE but to a relatively lesser degree as compared to the geometries from Cluster 1. However, one source of problem that can be easily noticed is that the red cross-sections have drifted very close to the external blade airfoil geometry. This means that there is a high possibility that the core will protrude out of the blade surface due to the effects of manufacturing variability. If this is true, then most of the perturbed geometries for these designs should have failed in the MVA workflow. Following this realization, the number of perturbed geometries that passed through the MVA workflow for the nominal designs picked up from Cluster 2 were analysed. It was observed that for most of these designs, only 5-12 morphed geometries did not fail during the FEA. This explains why the nominal designs from Cluster 2 indicated a low value of standard deviation. Hence, it was considered essential to add a penalty value to the *std* for each new design, in accordance with the number of failed

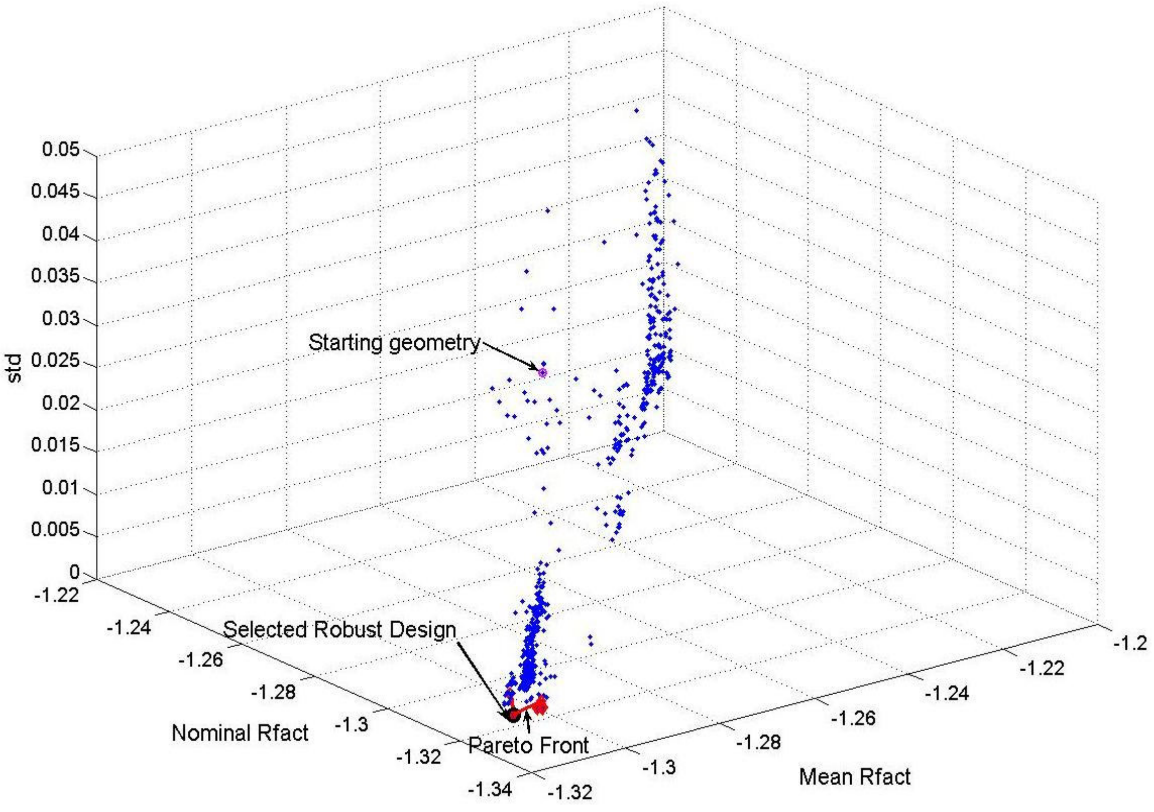

Figure 7.13: A zoomed in view of the plot shown in Figure 7.12 focusing on the region of interest.

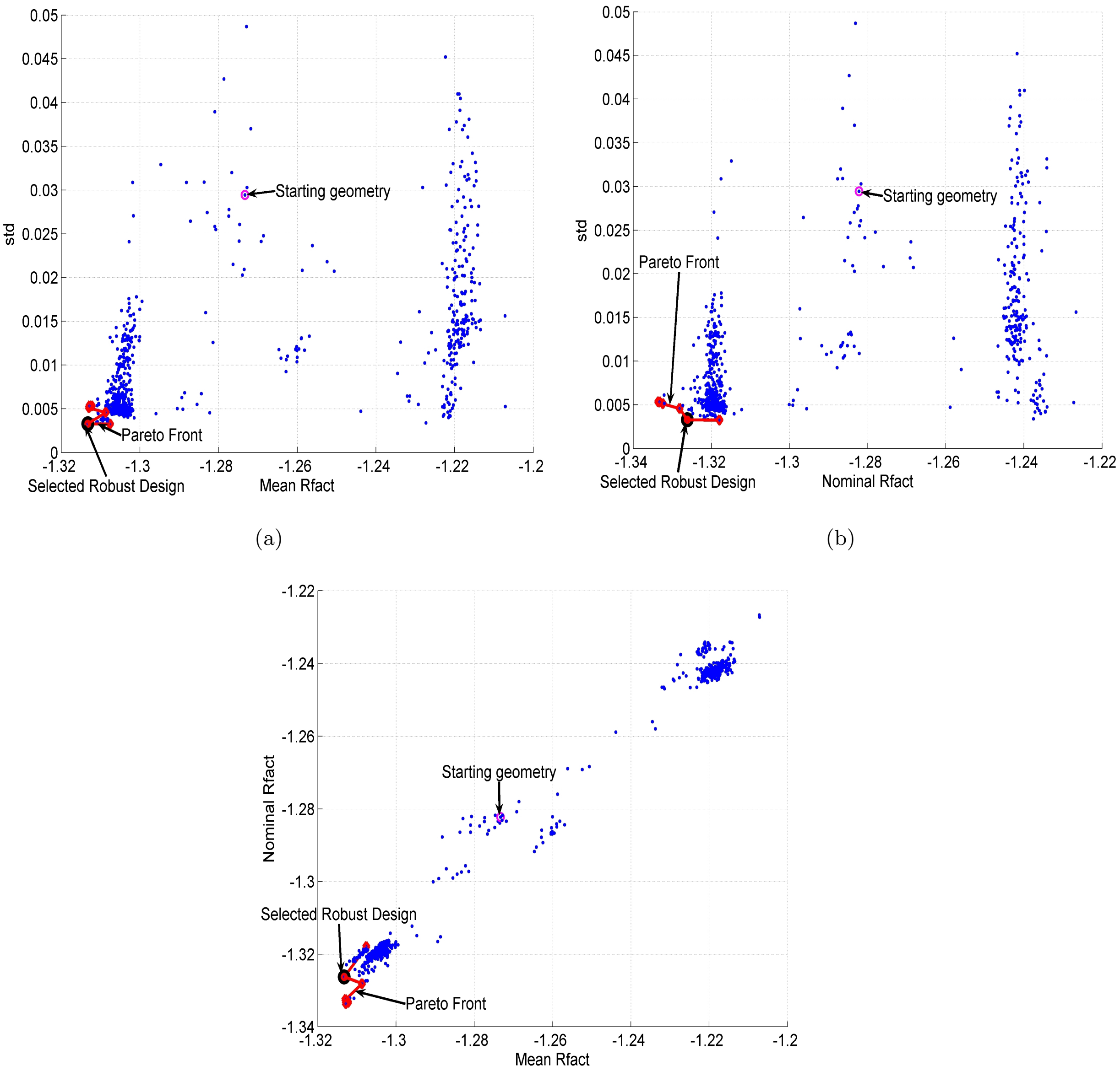

(a)

(b)

(c)

Figure 7.14: Plot of (a) standard deviation vs. mean life, (b) standard deviation vs. nominal life, and (c) nominal life vs. mean life, showing the explored design points and the Pareto front with penalties added to *std*.

perturbations for that design in the MVA workflow.

In order to add the penalties, first, the current 741 design points were taken. Then, a penalty value of 0.001 per failed manufacturing perturbation was added to the *std* calculated for these points. This penalty value would need to be different for different problems based on experience and the problem at hand. For the present case, a penalty value of 0.001 was considered appropriate. Following this, the IRDW was modified to add this penalty value to the calculated value of *std* for each new nominal design. Then, the IRDW was re-run from the 24th generation onwards, for 5 more generations, with the same population size of 101 for each generation. A total of 505 new designs were explored with no improvement in the Pareto-optimal solutions. Hence, it was assumed that our optimization problem has already converged to the best possible results. The resultant plot of the explored design points and the Pareto front obtained from these points is shown in Figure 7.12. A zoomed in view of this plot in the region of interest in shown in Figure 7.13. For ease of trade-off analysis, 2-d views of Figure 7.13 are shown in Figure 7.14. Adding the penalty values to the *std* ensured that only those designs, for which most of the morphed geometries passed through the MVA workflow, were ranked higher in the objective function space. All the designs on the Pareto front in Figures 7.13 and 7.14 demonstrated a success rate of 100% through the MVA workflow, i.e., all the 42 perturbed geometries

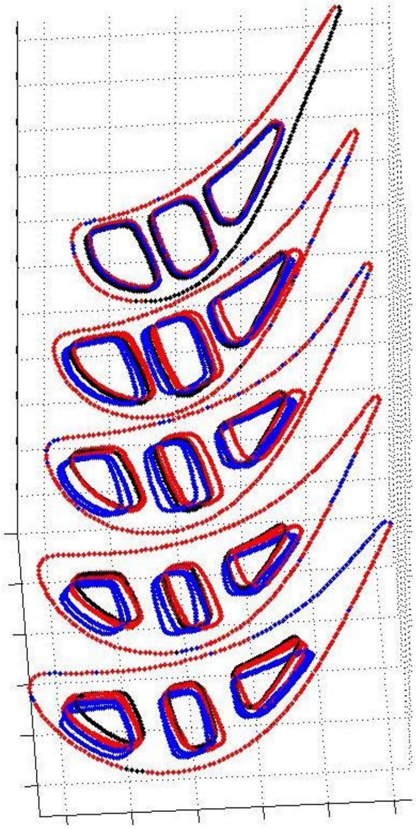

Figure 7.15: A comparison of the nominal designs, all of which indicated a 100% success through the MVA workflow. The black cross-sections represent the starting geometry, the blue curves represent the designs on the new Pareto front, and, the red cross-sections represent the geometries that were originally a part of Cluster 2.

were successful through the FEA for these designs. Still, there were a couple of designs that were originally a part of Cluster 2 and indicated a 100% success through the MVA workflow. These designs, however, had higher values of *std* as compared to the Pareto-optimal solutions. A couple of these designs are compared with the Pareto-optimal solutions and the base geometry in Figure 7.15. As we can observe in the figure, the differences between the red and blue core geometries are slightly similar to what was seen before in Figure 7.11. The blue cross-sections have drifted towards the suction surface and LE resulting in better mean and nominal lives as compared to the starting geometry. On the other hand, the red cross-sections tend to shift towards the pressure surface and TE leading to relatively good values of *std*, but, much worse mean and nominal lives when compared with the base design. Also, the Tip section for all geometries remains unchanged, while, noticeable differences can be observed at the remaining geometric sections. This time, the red cross-sections do not drift very close to the external blade surface, which explains the 100% success rate observed through the MVA workflow.

The final selected robust-optimal solution for the present problem is marked in Figures 7.13 and 7.14. This design indicates the best values of *std* and mean life and a relatively good improvement in nominal life as well. Although, three more designs on the Pareto front show better values of nominal life, their *std* is almost double than that of the selected design. Table 7.1 compares the nominal life, mean life and *std* for the starting geometry, the best solution from deterministic optimization (*next best point*), and the selected robust-optimal solution. The approximate percentage improvements relative to the base design in the nominal life, mean life and *std* for the selected deterministic solution and the robust-optimal design are shown in Table 7.2. Looking at the values in these tables, it becomes clear that while the selected deterministic design gives us better improvements in life, a slight compromise on these values may result in a relatively much lower value of *std*. The variability in life observed for the robust optimal solution is around 27.5% lesser than that for the selected deterministic solution. Also, it may be recalled that the deterministic optimization procedure actually leads to a design that indicated the best value of nominal life observed so far, but, was unable to withstand the effects of manufacturing variability due to the core deviating too close to the blade surface. This risk can be avoided in robust design optimization by including the variability in life as the objective function. Of course, other options on the Pareto front are also available for the designer if one objective function is considered more important than the

Table 7.1: Values of nominal life, mean life and *std* (without penalties) for the base geometry, the selected deterministic solution and the robust-optimal solution.

Blade geometry	Nominal Life	Mean Life	*std*
Base design	1.282	1.273	0.02543
Selected deterministic solution	1.335	1.320	0.01026
Optimal robust solution	1.326	1.313	0.00327

Table 7.2: Improvement in the nominal life, mean life and *std* of the selected deterministic design and the optimal robust design relative to the base geometry.

Blade geometry	Nominal Life	Mean Life	*std*
Selected deterministic solution	4.13%	3.69%	59.65%
Optimal robust solution	3.43%	3.14%	87.14%

other. For example, in the present scenario, if the point indicating the best value of nominal life is selected from the Pareto front, it leads to an improvement of around 4.06% in the nominal life, 3.14% improvement in the mean life and 79% reduction in *std* relative to the base design. This results in a value of nominal life closer to the selected deterministic solution, but a lesser improvement in *std* relative to the selected optimal robust design. It is this property of Pareto-optimal solutions that makes them highly desirable. Any solution from the Pareto front can be selected depending upon the weight given to each objective function. All the designs on the Pareto front may be considered as good designs.

It was discussed before in Section 7.5.1, that coarser meshes were used for FEA during the blade design optimization studies in order to save the computational costs. The average mesh size used was around 45,000 elements, whereas, the mesh convergence study indicated that meshes with around 80,000 elements resulted in more accurate solutions for the turbine blade models. Once the optimal deterministic and robust design solutions were obtained, it was desired to analyse these geometries using finer meshes and compare the results for more accurate estimations of the possible gains from the robust-optimal solution. Therefore, meshes with around 80,000 elements were created on the base design, the selected deterministic solution and the robust-optimal design and analysed for the effects of manufacturing variability using the same FEA codes. The results of this study are presented in Table 7.3 and the percentage gains in the mean life, nominal life and *std* are shown in Table 7.4. As we can observe in these tables, the percentage gains that can be expected in the mean life, nominal life and standard deviation have reduced as compared to the observations made from the coarser meshes. However, these results still support the fact that the robust design optimization process can lead to around 28.51% further reduction in the *std* for the turbine blade models under study as compared to the traditional approach of deterministic design optimization. The gains in the nominal and mean lives obtained from the two designs are also similar. Note that the base design used here is different from the nominal design analysed in Chapter 5, Section 5.5. The starting geometry used for optimization studies was obtained by modifying the original CAD model to introduce parametric changes required for the implementation of the FFD process for blade design changes. This accounts for the differences in results obtained from the lifing analysis of the two geometries. The purpose of the study presented in this section was to prove that the proposed approach for robust design optimization works for the present problem and this is demonstrated in the results presented in Tables 7.3 and 7.4.

Table 7.3: Values of nominal life, mean life and *std* (without penalties) for the base design, the selected deterministic design and the robust-optimal solution obtained from a mesh of around 80,000 elements.

Blade geometry	Nominal Life	Mean Life	*std*
Base design	1.371	1.348	0.00981
Selected deterministic solution	1.404	1.391	0.00699
Optimal robust solution	1.399	1.389	0.00419

Table 7.4: Improvement in the nominal life, mean life and *std* of the selected deterministic design and the optimal robust solution relative to the base geometry obtained from a FEA of the finer meshes.

Blade geometry	Nominal Life	Mean Life	*std*
Selected deterministic solution	2.41%	3.13%	28.72%
Optimal robust solution	2.05%	3.03%	57.23%

The geometries for the robust-optimal design, the selected deterministic solution and the base design are compared in Figure 7.16. In agreement with our observations in Figures 7.11 and 7.15, the core for the robust design has drifted towards the suction surface and LE resulting in improving the nominal and mean lives and reducing the value of *std*. By comparison, the core geometry for the deterministic design also tends to deviate towards the suction surface improving the nominal and mean lives, but, the drift in its shape towards the TE appears to affect the standard deviation. Some conclusions that we can make from our observations in Figures 7.11, 7.15 and 7.16 are : 1) moving the core towards the suction surface improves the nominal and mean lives, 2) moving the core towards the leading edge reduces the standard deviation in life, 3) moving the core towards the pressure surface reduces the nominal and mean lives, and 4) moving the core towards the trailing edge increases the standard deviation in life, even though it is much better than the standard deviation for the base design. It can also be deduced from the observations so far that the nominal life and mean life are not much in competition with each other for the turbine blade problem as might be expected.

Finally, it is worth checking whether there are any shifts in the critical region for the base geometry and the robust-optimal solution. It is also interesting to observe the changes in the stress distribution for the two blades. Figures 7.17(a) and 7.18(a) show the critical region of blade failure for the base design and the robust design, respectively. The yellow coloured contours in these two figures indicate the location of

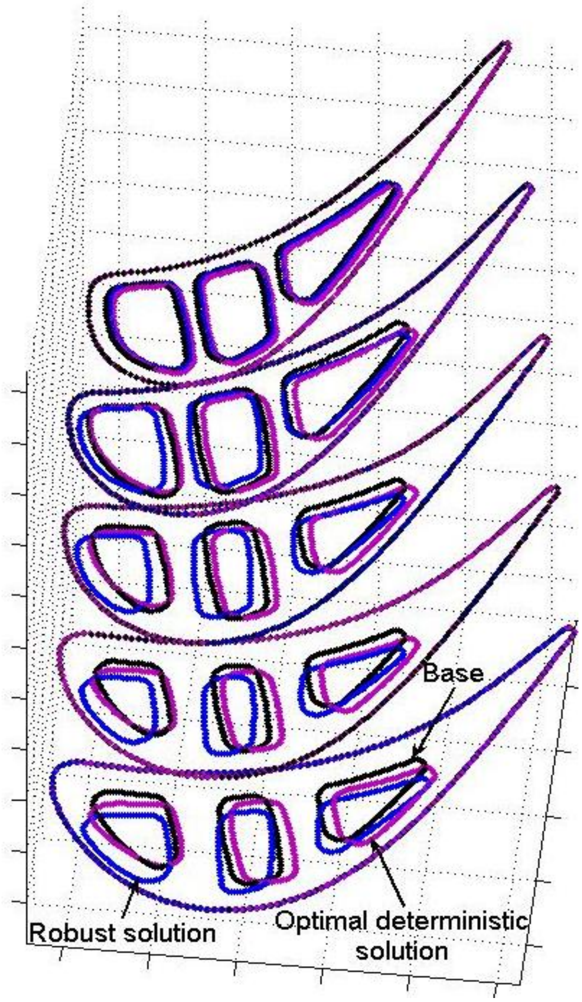

Figure 7.16: A comparison of the robust-optimal design and the selected deterministic design with the base geometry.

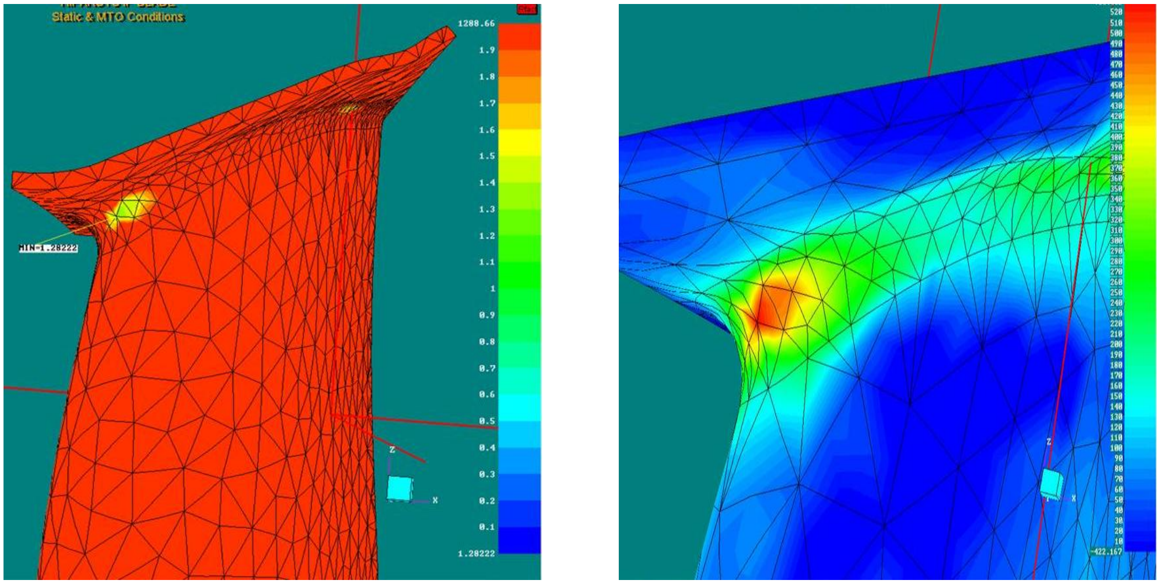

(a) (b)

Figure 7.17: (a) Contour plots for the value of $Rfact$, and (b) contour plots for the worst principal stress distribution in the critical region, on the base turbine blade design.

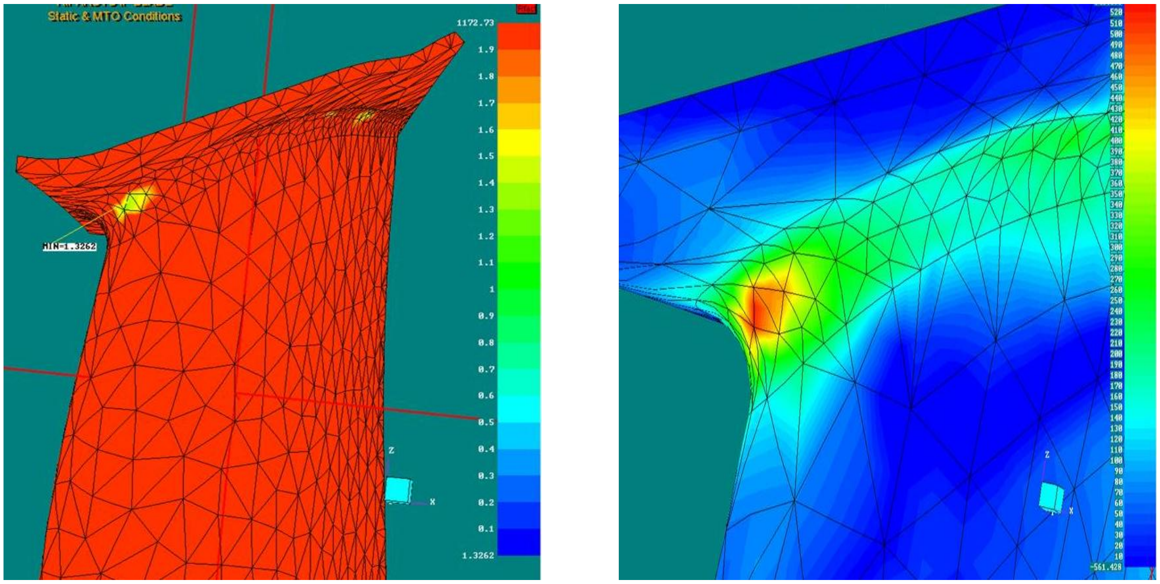

(a) (b)

Figure 7.18: (a) Contour plots for the value of $Rfact$, and (b) contour plots for the worst principal stress distribution in the critical region, on the selected robust turbine blade design.

the critical region. It is observed that there is no shift in the critical region for the robust turbine blade design. If anything, this region has only become slightly smaller for the robust-optimal solution as compared to the base design. The stress distribution for the two designs in the critical region is shown in Figures 7.17(b) and 7.18(b). The value of worst principal stress increases as the contours change their color from dark blue to dark red. It can be observed in Figure 7.17(b), that the value of the stress in the critical region is higher and more concentrated for the base turbine blade design. On the other hand, the contour plots for Figure 7.18(b) show that the worst principal stress in the critical region is lower and more distributed as compared to Figure 7.17(b). These figures indicate that the robust turbine blade design improves its nominal life and reduces its variability in life by distributing the stress from the critical region to the adjacent blade volume. The worst principal stress for the nominal design is higher and more concentrated in and around the critical region resulting in early blade failure and increased variability in life as compared to the robust solution.

7.6 Summary

In this chapter, a robust design study of hollow turbine blade was conducted with the aim of improving the nominal and mean lives and reducing the variability in life in the presence of manufacturing variability. A workflow was created in iSIGHT that used a combination of FFD, MATLAB, JAVA, LES solvers and FEA solvers for estimating the mean life and standard deviation in life for manufacturing variability analysis. This workflow was integrated with an existing iSIGHT workflow that employed CAD tools and FFD for changing the design. In the end, the integrated workflow was used for the robust design optimization of turbine blades. The design of the blade was changed for each new run of the workflow, and the effects of manufacturing variability were estimated by calculating the values of mean life and standard deviation in life.

A separate study was conducted in which a deterministic optimal solution for the turbine blade problem was sought. Results of the deterministic optimization study indicated that the design with best value of nominal life may not always be the best solution. For example, in the present case, the optimal deterministic solution resulted in a 4.68% improvement in life relative to the base design. However, this design was unable to withstand the effects of manufacturing variability since the core protruded out of the blade surface for 17 out of the 42 perturbed designs considered. The next best solution from the deterministic optimization showed some promise, with an improvement of around 4.13% in the nominal life, and a reduction of around 59.65% in the standard deviation relative to to the base design.

The robust design study resulted in an optimal solution that had an improvement of around 3.43% in the nominal life, a 3.14% improvement in the mean life and a reduction of around 87.14% in the standard deviation relative to the base design. This meant that a slight compromise in the values of mean and nominal lives could lead to a further reduction of around 27.5% in the standard deviation if the robust design was preferred over the selected deterministic design. More accurate predictions of the nominal life, mean life and standard deviation in life were obtained by a finite element analysis of the finer meshes generated on the base geometry, the next best design from the deterministic design optimization, and the robust-optimal solution. These results indicated that the improvements in nominal and mean lives obtained from the selected deterministic design and the optimal robust design were not very different. However, the robust solution still resulted in a further reduction of around 28.5% in the blade life variability as compared to the selected deterministic design. It was also noted that there were no shifts in the critical region for the robust turbine blade geometry. The stress profile plots indicated that the base geometry showed a lower value of life because the stress in the critical region was high and more concentrated. In comparison, the robust solution indicated a reduced variability and improved value of nominal life since the stress in the critical region was relatively less and more distributed to the adjacent blade volume.

A detailed analysis of the different geometries obtained from the robust design study and the deterministic optimization indicated the following :

- Deviations in the core towards the suction surface tend to improve the nominal and mean lives.
- Moving the core towards the leading edge reduces the standard deviation in life.
- Drifts in the core towards the pressure surface reduce the nominal and mean lives.
- Moving the core towards the trailing edge increases the standard deviation in life, but, this value is usually observed to be much better than the standard deviation for the base design.

Chapter 8

Conclusions and Future Research

This chapter concludes this thesis with a brief synopsis of the inferences derived from the present research, and its contributions to the field of uncertainty analysis and robust design. A brief description of the probable directions for future research, in continuation with the present analysis, is also presented.

8.1 Research Summary

The purpose of the present research work was to estimate the effects of manufacturing variability on hollow turbine blades from the measurement data available on a randomly selected sample of these blades. A methodology based on the application of existing probabilistic techniques, i.e., PCA and FFT, was proposed to filter out measurement error from the measurement dataset and capture the effects of manufacturing variability in terms of the manufacturing drift with time, and the blade to blade manufacturing variations. Once the probable values of actual variations were obtained, it was possible to use this data for characterizing the 3-d effects of manufacturing variability on turbine blade shapes. It was found that the variations due to manufacturing processes had negligible effects on the external blade airfoil geometry. Hence, a FFD based methodology that worked in conjunction with non-linear optimization was proposed in order to produce probable manufactured core shapes from the limited number of available measurements. Information obtained from FFD on the deformed core geometries was then used to morph the nominal blade volume mesh resulting in 3-d representations of the probable manufactured turbine blades. These morphed volume meshes were used for lifing and stress calculations using FEA tools to quantify the effects of manufacturing variability on turbine blade life.

The results from the probabilistic measurement data analysis were used to calculate the delta perturbations affecting the nominal geometry due to variations in the casting process. These perturbations were used for a robust design optimization study by using a combination of FFD and mesh morphing methodologies. The designed shape of the turbine blade was changed by modifying the core shape and position and the effects of manufacturing variability on these new nominal designs were quantified by applying the delta perturbations. In the end, a robust-optimal solution was obtained that not only demonstrated a reduced variability in life, but also indicated considerable improvements in the mean and nominal lives as compared to the base turbine blade design.

Contributions

The research presented in this thesis has led to the following publications :

1. N. Thakur, A. Keane, P.B. Nair, Capture of Manufacturing Uncertainty in Turbine Blades through Probabilistic Techniques, in: Proceedings of the 7th ASMO-UK/ISSMO International Conference on Engineering Design Optimization, Bath, UK, 2008, pp. 387-396.

2. N. Thakur, A. Keane, P.B. Nair, Probabilistic Analysis of Manufacturing Uncertainty in Turbine Blades, in: Proceedings of the ASME 2009 International Design Engineering Technical Conferences & Computers and Information in Engineering Conference (IDETC/CIE 2009), no. DETC2009-86190, San Diego, California, USA, 2009.

3. N. Thakur, A.J. Keane, P.B. Nair, Estimating the effect of Manufacturing Variability on Turbine Blade Life, in: M. Beer, R.L. Muhanna, R.L. Mullen (Eds.), Proceedings of the 4th International Workshop on Reliable Engineering Computing (REC 2010), Singapore, 2010, pp. 311-322.

4. N. Thakur, A. Keane, P.B. Nair, A.R. Rao, Probabilistic Measurement Data Analysis for estimating the impact of Manufacturing Variability on Turbine Blade Life, ASME Journal of Mechanical Design - Under Review.

5. N. Thakur, A.J. Keane, P.B. Nair, Robust Design of Turbine Blades against Manufacturing Variability, (In Preparation).

Manufacturing and Measurement Processes

The casting process used for manufacturing the hollow turbine blades has been explained in detail. An insight into the various processes used for manufacturing the turbine blades helped in understanding the various sources of manufacturing variability. The possible sources of geometric variations in the blades were identified as :

- Unwanted deviations in the core position due to the buffer space allowed for core movement when the molten wax is poured into the dies.
- Unwanted deformations in the core shape when hot air at high pressure is passed through the mold assembly for wax removal.
- Thermal expansion of the core when molten metal is pumped into the casts, and undesirable core deformations due to the high hydrostatic pressure of the molten metal.
- The possibility of trapped air bubbles inside the ceramic core models which may expand due to the high temperature, or, contract due to the high hydrostatic pressure of the molten metal.
- Wear and tear of tools and changes in the surrounding temperature and humidity levels may cause some manufacturing drift with time.

Different procedures used for blade inspection were also presented. The ultrasonic blade wall thickness measurement process was described in detail. Various sources of measurement error that may be affecting the measurement data during ultrasonic wall thickness inspection are briefly summarized as follows:

- Non-firm clamping of the blades over the ultrasonic head may lead to left and right misalignments of the blade resulting in over-thick readings.
- Thick markings indicating the measurement cross-sections on the blade surface may lead to offsets in the measurement planes.
- The surfaces across which measurements are being taken are hidden from the view of the operator leading to inaccuracies.
- Any misalignment of the blade while pressing the pedal for recording the measurements may lead to measurement error.

- Human error remains a possibility that cannot be ignored.

Manufacturing Variability Analysis

A de-noising methodology that employs PCA and FFT is proposed for filtering out the measurement error from the measured data and capturing the underlying effects of manufacturing variability. A technique for dimensionality reduction in case of PCA, and threshold selection in case of FFT, was proposed that uses prior information available on the measurement error. This prior knowledge on the measurement variability was obtained by a statistical analysis of repeated measurements taken on a randomly selected sample of turbine blades. In the end, the effects of manufacturing variability were captured in terms of the manufacturing drift with time and the blade to blade manufacturing variations. Variance plots obtained from the repeated measurements indicated the following :

- A large curvature in the external airfoil surface leads to greater measurement error.
- A relatively firmer hold on the blade while taking measurements reduces the measurement variability.
- The variability in measurements is relatively small as compared to the magnitude of thicknesses, indicating, that the operators taking these measurements are well-trained.

Application of the proposed methodology to the turbine blade ultrasonic wall thickness measurement data resulted in 42 sets of 18 thickness measurements. These 42 sets are representative of the typical thicknesses of the blades coming out of the manufacturing process. 31 of these blades were obtained from the application of PCA and FFT techniques on the measurement data and captured the effects of manufacturing drift with time. The remaining 11 blades were obtained from a statistical data analysis of the repeated measurements and represented the effects of blade to blade manufacturing variations.

3-d Geometry Manipulation using Limited Measurements

A FFD based methodology was proposed, that works in conjunction with non-linear optimization, for manipulating 3-d geometries from a limited number of available measurements. This methodology was devised to characterize the 3-d geometric variability in turbine blade shapes, from the 42 sets of 18 thickness measurements available per blade. In a separate study, it was observed that the variations in manufacturing processes have negligible effects on the external blade airfoil geometry. This implies that the brunt of manufacturing variability is borne by the internal core shapes. In order to characterize these variations, the proposed FFD based methodology was employed along with non-linear optimization to obtain the best matches to the probable manufactured core shapes. Alternatives to non-linear optimization, e.g., constrained and unconstrained forms of linear least-squares solution, were also explored. It was found that although the linear least-squares approach may prove to be useful for a variety of problems, the non-linear optimization method was well-suited for the present problem due to its ability to generate more regularized geometries. This was desirable since the blades are not expected to deviate greatly from their base design.

The application of the proposed methodology resulted in 42 different geometries representing the probable manufactured core shapes. The deformed cores were compared with the nominal core and it was found that the manipulated geometries agreed quite well with each other. This is desirable since similar deviations from the nominal are expected in the manufactured shapes. It was also observed that the suction surface at the Tip section for the deformed and nominal cores almost overlapped each other. This area is the critical region of blade failure. Hence, special care is taken during blade manufacture to ensure that the critical region meets the design specifications. All these observations indicated that the proposed FFD based approach worked fairly well for the present problem.

Linear Elasticity based Mesh Morphing

An approach that employs a linear elasticity solving (LES) based method was used for morphing the nominal turbine blade volume mesh multiple times. Using this approach, probable representations of the manufactured turbine blades were obtained in FEA ready form. The application of the FFD based methodology for the 42 sets of thickness measurements resulted in deformed core surface meshes for each of these measurement sets. The nodal displacements to be applied on the core surface were calculated by subtracting the nodal coordinates of the deformed core surface from the nodal coordinates of the nominal core mesh. Keeping the external geometry fixed, these displacements were applied to the nodes on the internal core surface of the turbine blade volume mesh. This was followed by running the linear elasticity solver available within the FEA tool for obtaining 42 different volume meshes representing the probable manufactured turbine blade shapes.

Effects of Manufacturing Variability on Turbine Blade Life

The 42 turbine blade volume meshes obtained from the application of the LES based approach were analysed using FEA to estimate the effects of manufacturing variability on the blade life. As expected, no shifts in the critical region were observed for the perturbed geometries. The presence of manufacturing variations resulted in reducing the life for most of the probable turbine blade shapes. However, they also demonstrated some positive effects on a couple of blades by slightly improving their values of life. On a normalized scale, the blades were designed for an average life of 1.448, but, the mean life of the probable manufactured blades was observed to be around 1.424, which is approximately 1.7% lower relative to the designed life. Also, the normalized life for the reconstructed blades varied between 1.395 and 1.465, the former being approximately 3.7% lower relative to the nominal life. The standard deviation in life was calculated to be around 0.0138.

Response Surface Models for Lifing Predictions

An effort was made to create response surface models (RSMs) for predicting the turbine blade life from the 18 thickness measurements, since, the computational time required for the FEA runs was relatively high. Kriging in combination with the LP_τ DOE technique was implemented to generate surrogates for modeling the relationship between the 18 input thicknesses and the output values of life. A leave-one-out cross-validation test was performed on the resulting RSM and it was shown that the scatter in the correlation plots was unacceptably high. Simpler variants of the original, more complicated problem, were also tried with no success. This study led to the conclusion that generating reliable RSMs was not an option for the present problem, and more accurate results could be obtained for the turbine blade lifing analysis by using the full computational models.

Robust Design of Turbine Blade against Manufacturing Variability

The robust design optimization of turbine blades was performed by using an iSIGHT workflow that employed a combination of tools, including, CAD, FFD, FEA, MATLAB, JAVA, CADfix, Parasolid and LES solvers. This workflow permitted changes in the design of the blades by modifying the core shape and position. Every new geometry was then analysed using computational models for estimating the probable values of mean life and standard deviation in life due to the presence of manufacturing variability. The objective of the robust design study was to seek a turbine blade design with improved mean and nominal lives and reduced variability in the values of life as compared to the base design.

The benefits of selecting an optimal deterministic design were explored by running a parallel optimization study with the single objective of improving the nominal life. It was noted that selecting the optimal deterministic design may not be the best solution to the current problem, since the core geometry for this design was dangerously close to the external blade airfoil surface. As a result of this closeness, the core protruded out of the blade surface for 17 out of the 42 perturbed geometries that represented the effects of manufacturing variations. This was followed by picking up the next best design point obtained from the deterministic optimization study. This design appeared to be relatively more reliable as 39 out of the 42 perturbations passed successfully though the FEA. Hence, it was selected for comparison with the robust-optimal solution. The selected deterministic design indicated an improvement in nominal life of around 2.41%, and a 3.13% improvement in mean life, relative to the base design. The reduction in standard deviation for this design was observed to be around 28.72% relative to the base geometry. In comparison, the optimal robust solution demonstrated a relative improvement in the nominal and mean lives of around 2.05% and 3.03% respectively, as compared to the base design. The relative reduction observed in standard deviation for the robust-optimal solution was around 57.23%, which is around 28.5% lesser than that obtained from the selected deterministic design. Therefore, the robust-optimal solution definitely offerred greater reductions in the turbine blade life variability, provided a slight compromise in the nominal and mean lives was acceptable.

Examination of the critical region for the base model and the optimal robust design indicated that there were no shifts in the critical region. In fact, the critical area for the robust solution was slightly smaller than that for the base design. Also, the stress profile plots for the two geometries indicated that the worst principal stress for the base geometry was higher and more concentrated in the critical region leading to a lesser value of mean and nominal lives as compared to the robust solution. On the other hand, the robust turbine blade design demonstrated relatively more distributed values of worst principal stress in the critical region resulting in improved nominal and mean lives and reduced standard deviation.

An indepth study of the base and deformed geometries indicated the following:

- Deviations in the core towards the suction surface tend to improve the nominal and mean lives.

- Moving the core towards the leading edge reduces the standard deviation in life.
- Drifts in the core towards the pressure surface reduce the nominal and mean lives.
- Moving the core towards the trailing edge increases the standard deviation in life, but, this value is usually observed to be much better than the standard deviation for the base design.

8.2 Future Research

Future research work could look for improvements in the techniques used for manufacturing variability quantification, and reducing the computational effort required for robust design studies of complicated parts. Some directions for future research are outlined below:

- In the present work, manufacturing variability was captured as the effects due to manufacturing drift with time and the blade to blade manufacturing error. It may be interesting to segregate the manufacturing variations caused by individual procedures that constitute the manufacturing process. The procedures leading to the most geometric variations may then be identified. This may be followed by making suitable suggestions for improvement in the current manufacturing processes. Finally, it may lead to a reduction of the sources, and hence the effects, of manufacturing variability.
- In the current research work, manufacturing variability was only accounted for by a limited number of available measurements. A FFD based methodology was implemented for characterizing the geometric variability from the limited measurements by maintaining a balance between the global and local deformations. It may be interesting to obtain more accurate representations of the manufactured shapes by collecting X-ray scans on these parts. The scanned data may then be analysed using PCA based techniques to characterize the geometric variability more accurately.
- The FFD based methodology proposed in the present work analysed the effects of manufacturing variability on the internal core shape. Fortunately, negligible effects of variations due to the manufacturing processes were observed on the external blade airfoil geometry. For some cases, it is highly probable that the sources of geometric variability

lead to deviations in both the external and internal shapes of complicated parts. In that case, it becomes essential to characterize the coupled behaviour of 3-d geometric variations. This leads to the need for more sophisticated methodologies for geometry manipulation that may be implemented for simulating the coupled behaviour of 3-d variations in both the external and internal geometries.

- For the turbine blade problem, it was desirable to create RSMs for reducing computational costs. However, the leave-one-out cross validation procedure indicated that generating reliable RSMs for the present problem was not an option. Unsuccessful attempts were made to break down the more complicated problem of modeling the relationship between the blade measurements and lifing predictions, to its simpler variants. It may be an interesting proposition to break down the problem further into each of the individual processes involved in estimating the value of life starting from the thickness measurements. Efforts may then be made to generate a series of RSMs, each representing one procedure at a time, from the network of methodologies used for the current problem. These surrogates may then be stitched together to result in a complicated network of approximate models that may be more reliable than the current RSMs. Although creating too many surrogates adds to the prediction error due to the cumulative error effects, exploring this option may lead to saving considerable computational costs if successful.
- Since the RSMs generated for the present case did not prove to be very reliable, a sensitivity analysis was not performed for the current problem. It may, however, prove to be very interesting to find out which of the measurements taken on the turbine blades affect their life the most. Suitable recommendations may then be made to focus on the more important measurements during blade inspection, resulting in saving the measurement costs.

Appendix A

Linear Algebra

The theorems presented in this chapter are based on the paper by Shlens [19].

A.1 Theorem 1

If $\mathbf{X}_0$ is any matrix, the matrices $\mathbf{X}_0\mathbf{X}_0^{\mathrm{T}}$ and $\mathbf{X}_0^{\mathrm{T}}\mathbf{X}_0$ are both symmetric.

For a matrix to be symmetric, it should be equal to its transpose. Hence, taking the transpose of $\mathbf{X}_0\mathbf{X}_0^{\mathrm{T}}$ we obtain,

$$(\mathbf{X}_0\mathbf{X}_0^{\mathrm{T}})^{\mathrm{T}} = \mathbf{X}_0^{\mathrm{TT}}\mathbf{X}_0^{\mathrm{T}} = \mathbf{X}_0\mathbf{X}_0^{\mathrm{T}}. \tag{A.1}$$

Similarly, for $\mathbf{X}_0^{\mathrm{T}}\mathbf{X}_0$ we obtain,

$$(\mathbf{X}_0^{\mathrm{T}}\mathbf{X}_0)^{\mathrm{T}} = \mathbf{X}_0^{\mathrm{T}}\mathbf{X}_0^{\mathrm{TT}} = \mathbf{X}_0^{\mathrm{T}}\mathbf{X}_0. \tag{A.2}$$

A.2 Theorem 2

If $\mathbf{L}$ is an orthogonal matrix, then $\mathbf{L}^{-1} = \mathbf{L}^{\mathbf{T}}$.

Let $\mathbf{L}$ be an $n \times n$ matrix such that,

$$\mathbf{L} = \begin{pmatrix} \mathbf{l_1} & \mathbf{l_2} & \mathbf{l_3} & \cdots & \mathbf{l_n} \end{pmatrix}, \tag{A.3}$$

where $\mathbf{l_i}$ is the i^{th} *column* matrix. By definition of an inverse matrix, we know that,

$$\mathbf{L}^{-1}\mathbf{L} = \mathbf{I}, \tag{A.4}$$

where $\mathbf{I}$ is the identity matrix. Therefore, a proof that $\mathbf{L^T L} = \mathbf{I}$ should be sufficient to prove that $\mathbf{L}^T = \mathbf{L}^{-1}$. Now,

$$\mathbf{L^T L} = \begin{pmatrix} \mathbf{l_1} \\ \mathbf{l_2} \\ \mathbf{l_3} \\ \vdots \\ \mathbf{l_n} \end{pmatrix} \begin{pmatrix} \mathbf{l_1} & \mathbf{l_2} & \mathbf{l_3} & \cdots & \mathbf{l_n} \end{pmatrix} = \begin{pmatrix} \mathbf{l_1 . l_1} & \mathbf{l_1 . l_2} & \mathbf{l_1 . l_3} & \cdots & \mathbf{l_1 . l_n} \\ \mathbf{l_2 . l_1} & \mathbf{l_2 . l_2} & \mathbf{l_2 . l_3} & \cdots & \mathbf{l_2 . l_n} \\ \mathbf{l_3 . l_1} & \mathbf{l_3 . l_2} & \mathbf{l_3 . l_3} & \cdots & \mathbf{l_3 . l_n} \\ \vdots & \vdots & \vdots & \vdots & \vdots \\ \mathbf{l_n . l_1} & \mathbf{l_n . l_2} & \mathbf{l_n . l_3} & \cdots & \mathbf{l_n . l_n} \end{pmatrix}. \tag{A.5}$$

But, the columns of an orthogonal matrix are orthogonal to each other. Thus, the dot product of any two columns is zero and the dot product of a column with itself is one. Substituting this in expression (A.5) we obtain,

$$\mathbf{L^T L} = \begin{pmatrix} 1 & 0 & 0 & \cdots & 0 \\ 0 & 1 & 0 & \cdots & 0 \\ 0 & 0 & 1 & \cdots & 0 \\ \vdots & \vdots & \vdots & \vdots & \vdots \\ 0 & 0 & 0 & \cdots & 1 \end{pmatrix} = \mathbf{I}. \tag{A.6}$$

Comparing equations (A.4) and (A.6), we can observe that $\mathbf{L}^T = \mathbf{L}^{-1}$.

A.3 Theorem 3

A symmetric matrix is diagonalized by a matrix of its orthonormal eigenvectors.

Let $\mathbf{A}$ be a square $n \times n$ symmetric matrix with associated eigenvectors, $\mathbf{E} = [\mathbf{e_1} \quad \mathbf{e_2} \quad \cdots \quad \mathbf{e_n}]$, where the i^{th} column of $\mathbf{E}$ is the eigenvector $\mathbf{e_i}$. According to this theorem, there exists a diagonal matrix $\mathbf{D}$ such that $\mathbf{A} = \mathbf{EDE^T}$.

First, lets assume that $\mathbf{A}$ is some matrix, not necessarily symmetric, which has independent eigenvectors $\{\mathbf{e_1}, \mathbf{e_2}, \cdots, \mathbf{e_n}\}$ constituting the matrix $\mathbf{E}$ such that, $\mathbf{E} = [\mathbf{e_1} \quad \mathbf{e_2} \quad \cdots \quad \mathbf{e_n}]$. Let $\mathbf{D}$ be the diagonal matrix where the i^{th} eigenvalue is placed in the ii^{th} position.

Now, multiplying $\mathbf{A}$ by $\mathbf{E}$ and $\mathbf{E}$ by $\mathbf{D}$ we obtain,

$$\mathbf{AE} = \begin{pmatrix} \mathbf{Ae_1} & \mathbf{Ae_2} & \cdots & \mathbf{Ae_n} \end{pmatrix}, \quad \text{and} \tag{A.7}$$

$$\mathbf{ED} = \begin{pmatrix} \lambda_1 \mathbf{e_1} & \lambda_2 \mathbf{e_2} & \cdots & \lambda_n \mathbf{e_n} \end{pmatrix}. \tag{A.8}$$

Now, according to the definition of eigenvalue equation, $\mathbf{Ae_i} = \lambda_i \mathbf{e_i}$ for all i. Hence $\mathbf{AE} = \mathbf{ED}$. Rearranging this expression results in $\mathbf{A} = \mathbf{EDE}^{-1}$. This implies that any matrix can be orthogonally diagonalized if and only if that matrix's eigenvectors are all linearly independent.

Let λ_1 and λ_2 be distinct eigenvalues for the eigenvectors $\mathbf{e_1}$ and $\mathbf{e_2}$ of some symmetric matrix. Now,

$$\begin{aligned}
\lambda_1 \mathbf{e_1}.\mathbf{e_2} &= (\lambda_1 \mathbf{e_1})^T \mathbf{e_2}, \\
&= (\mathbf{Ae_1})^T \mathbf{e_2}, \\
&= \mathbf{e_1}^T \mathbf{A}^T \mathbf{e_2}, \\
&= \mathbf{e_1}^T \mathbf{Ae_2}, \\
&= \mathbf{e_1}^T (\lambda_2 \mathbf{e_2}), \\
\lambda_1 \mathbf{e_1}.\mathbf{e_2} &= \lambda_2 \mathbf{e_1}.\mathbf{e_2}, \quad \text{or} \\
(\lambda_1 - \lambda_2)\mathbf{e_1}.\mathbf{e_2} &= 0. \qquad \text{(A.9)}
\end{aligned}$$

Since we have assumed that we are taking distinct eigenvalues, equation (A.9) implies that $\mathbf{e_1}.\mathbf{e_2} = 0$. This means that the eigenvectors of a symmetric matrix are orthogonal.

Going back to our original assumption that $\mathbf{A}$ is a symmetric matrix, by the proof above we know that the eigenvectors of $\mathbf{A}$ are all orthogonal. This implies that $\mathbf{E}$ is an orthogonal matrix. Therefore, by Theorem 1, $\mathbf{E}^T = \mathbf{E}^{-1}$ and the final result can be written as,

$$\mathbf{A} = \mathbf{EDE}^T \qquad \text{(A.10)}$$

Thus, we can state that a symmetric matrix is diagonalized by a matrix of its eigenvectors.

Appendix B

Multivariate Analysis of Variance (MANOVA)

B.1 Background

Multivariate Analysis of Variance (MANOVA) is simply an extension of the Analysis of Variance (ANOVA) technique, with the difference that while ANOVA is used in problems with one dependant variable, MANOVA does the same for multiple dependant variables [153]. The purpose of ANOVA is to quantitatively estimate the relative contribution each parameter (independent variable) variation makes to the overall response (dependant variable) variation [154]. Comparatively, MANOVA is preferred in two major situations: 1) when a single, overall statistical test is desired on several correlated dependant variables instead of performing multiple individual tests, and, 2) when it is important to explore how independent variables influence some patterning of response on the dependant variables [155]. Testing of the multiple dependant variables is accomplished by creating new dependant variables that maximize group differences. These new dependant variables are linear combinations of the original dependant variables [153].

The key assumptions made by MANOVA are :

- it assumes normal distribution of the dependant variable within the groups to be tested. Although, it is robust to non-normality caused by skewness, transformation or removal of outliers should be done before performing MANOVA,

- it assumes the existence of linear relationships among all pairs of dependant variables, all pairs of covariates, and all dependant variable-covariate pairs in each group,
- it assumes that the dependant variables have equal variance across the range of independent variables and their covariances are homogeneous across each group [153].

It is important to notice that MANOVA also has certain limitations [153] :

- It is extremely sensitive to outliers. In the presence of outliers, it may result in a *Type I* error (rejection of the null hypothesis when it is true) or a *Type II* error (failure to reject the null hypothesis when it is false) without indicating the nature of error in the analysis.
- If there is a high correlation between dependant variables, one dependant variable becomes a near-linear combination of the other dependant variable leading to statistical redundancy.
- MANOVA is more complicated as compared to ANOVA and hence there may be some ambiguity about which parameter value affects each dependant variable.

All these assumptions and limitations however, do not undermine the importance of MANOVA as an efficient statistical technique. It has been used successfully in various kinds of research, e.g., the study of evolutionary change in terms of genetic variation [156], study of the influence of days and months on market prices in the electricity market [157], analysis of information contained in speech signals about the linguistic message, the speaker and the communication channel [158], etc.

Simplifying things further, we may also state that ANOVA is used to test whether the means for two or more groups are taken from the same sampling distribution. On the other hand, MANOVA is used to test whether the *vectors* of means (since every set of measurements for each dependant variable has its own mean) for two or more groups are sampled from the same sampling distribution [155]. A detailed exposition of ANOVA/MANOVA techniques along with their mathematical formulations and practical applications are available in great detail in various textbooks in the literature [159, 160, 161, 154].

B.2 Mathematical Formulations

The following discussion presents the basic mathematics behind ANOVA and then moves on to explaining MANOVA and its direct relationship with ANOVA. The mathematical formulations of ANOVA and MANOVA that follow are based on the book by Harris [159].

Let us assume that our input data matrix $\mathbf{X}$ is divided into g groups such that $m_1 = m_2 = m_3 = \cdots = m_g = m_0$ and $n = 1$, i.e., each group has only one measurement variable. Please note that in reality the values of $m_1, m_2, m_3, \cdots, m_g$ may be different and $n \neq 1$. Here, the sample size is assumed to be m_0 for all the g groups for ease of explanation. $n = 1$ is assumed for explaining the working of the ANOVA technique first. Now, the *null hypothesis* may be stated as :

$$H_0 : \mu_1 = \mu_2 = \cdots = \mu_g, \tag{B.1}$$

where, μ is the standard symbol for group mean. If this null hypothesis is true, then on an average we would obtain,

$$\overline{X}_1 = \overline{X}_2 = \cdots = \overline{X}_g. \tag{B.2}$$

The next task is to select a single statistic that will summarize how far the sample means depart from the equality implied by H_0. In this case, let us adopt the sample variance of the g means,

$$s^2_{\overline{X}} = \sum_{j=0}^{g} (\overline{X}_j - \overline{\overline{X}})^2/(g-1). \tag{B.3}$$

In equation (B.3) above, $\overline{\overline{X}}$ means the overall mean matrix of the cumulative data. The second thing we need to know is whether the magnitude of the differences among the sample means (as measured by the variances of X) is consistent with the assumption of identical population means. A basis for comparison is provided by the well-known relationship between the variance of a population and the variance of means of samples drawn from that population,

$$Var_{\overline{X}^2} = \frac{Var}{m_0}, \tag{B.4}$$

where m_0 is the size of the sample on which each mean is calculated. Following this, it may be informative to compare the ratio of the direct estimate of $Var_{\overline{X}^2}$, with an estimate of $Var_{\overline{X}^2}$ assuming H_0, as given below :

$$F = \frac{s^2_{\overline{X}}}{s^2_w/m_0}, \tag{B.5}$$

where,

$$s_{\overline{X}}^2 = \left\{ (\overline{X}_1 - \overline{\overline{X}})^2 + (\overline{X}_2 - \overline{\overline{X}})^2 + \cdots + (\overline{X}_g - \overline{\overline{X}})^2 \right\} / (g-1), \tag{B.6}$$

$$s_w^2 = \left\{ \sum (X_1 - \overline{X}_1)^2 + \sum (X_2 - \overline{X}_2)^2 + \cdots + \sum (X_g - \overline{X}_g)^2 \right\} / (M-g). \tag{B.7}$$

Here, $s_{\overline{X}}^2$ denotes the sample variance in between groups, s_w^2 denotes the sample variance within groups, and the total number of measurements are denoted by $M = m_0 g$. Using expressions (B.5), (B.6) and (B.7) above, we may re-write the equation for F as,

$$F = \frac{\sum m_{0j} (\overline{X}_j - \overline{\overline{X}})^2 / (g-1)}{\sum \sum (X_j - \overline{X}_j)^2 / (M-g)} = \frac{SS_b/(g-1)}{SS_w/(M-g)} = \frac{MS_b}{MS_w}, \tag{B.8}$$

where, the symbol SS stands for *sum of squares*, MS stands for *mean squares*, subscript b stands for *between groups* and subscript w stands for *within groups*. Equation (B.8) represents the expression of the F statistic for univariate ANOVA. In this case, H_0 is true when $F \approx 1$. However, if $F>1$, then the alternative hypothesis is applicable to the case under study.

Now, applying the same theory to MANOVA and going back to our original data matrix $\mathbf{X}$ where we have $n \neq 1$ measured variables within each of the g groups, we obtain the expression for F as,

$$F(\mathbf{c}) = \frac{MS_{b,C}}{MS_{w,C}} = \frac{\sum m_{0j} (\overline{C}_j - \overline{\overline{C}})^2 / (g-1)}{\sum \sum (C_j - \overline{C}_j)^2 / (M-g)} = \frac{\mathbf{c^T B c}}{\mathbf{c^T W c}} \left(\frac{M-g}{g-1} \right), \tag{B.9}$$

where $MS_{b,C}$ is the mean square between groups and $MS_{w,C}$ is the within group mean square for the dependant variable C. C is given by,

$$C = c_1 X_1 + c_2 X_2 + \cdots + c_n X_n = \mathbf{Xc}, \tag{B.10}$$

where $\mathbf{c}$ is the matrix containing coefficients by which the original measured variables are multiplied. Recall that the testing of multiple dependant variables in MANOVA is accomplished by creating new dependant variables that are linear combinations of the original measured variables. In equation (B.9), $\mathbf{B}$ is the between-group SSCP (sums of squares and cross-products) matrix,

$$\mathbf{B} = \begin{pmatrix} SS_{b;1} & SP_{b;1,2} & SP_{b;1,3} & \cdots & SP_{b;1,n} \\ SP_{b;1,2} & SS_{b;2} & SP_{b;2,3} & \cdots & SP_{b;2,n} \\ SP_{b;1,3} & SP_{b;2,3} & SS_{b;3} & \cdots & SP_{b;3,n} \\ \vdots & \vdots & \vdots & \cdots & \vdots \\ SP_{b;1,n} & SP_{b;2,n} & SP_{b;3,n} & \cdots & SS_{b;n} \end{pmatrix}, \tag{B.11}$$

where,

$$SP_{b;r,s} = \sum m_{0j}(\overline{X}_{j,r} - \overline{\overline{X}}_r)(\overline{X}_{j,s} - \overline{\overline{X}}_s) \tag{B.12}$$

and,

$$SS_{b;r} = SP_{b;r,r} = \sum m_{0j}(\overline{X}_{j,r} - \overline{\overline{X}}_r)^2, \tag{B.13}$$

on variable r in group j, such that $s = 1, 2, \cdots, n$. $\mathbf{W}$ is the within-group covariance matrix and is given as,

$$SP_{w;r,s} = \sum \sum (X_{j,r} - \overline{X}_r)(X_{j,s} - \overline{X}_s). \tag{B.14}$$

The overall objective is to determine the value of $\mathbf{c}$ such that $\mathrm{F}(\mathbf{c})$ is maximized. The subsequent values of C (also called the *canonical* variables) give us an idea of the separation between groups. For example, in our case, $C1$ is the linear combination of the columns of $\mathbf{X}$ that represents the maximum separation between groups and $C2$ represents the maximum separation subject to it being orthogonal to $C1$, and so on. Therefore, a scatter plot of $C1$ vs. $C2$ or a dendrogram plot of the group means after a MANOVA analysis may help in determining any noticeable differences between the measurements contained in each of the time-based groups.

Appendix C

CDI and MVA Workflows

C.1 Changing the Blade Design

A zoomed in view of the CDI workflow is shown in Figure C.1. A detailed description of its various components and the logic of the workflow is given below:

- **Prologue**: This component contains a JAVA script that is used for initializing parallel runs of the CDI workflow. For the current workflow, this component was disabled because a lot of computational resources were already being consumed by the parallel runs of the MVA workflow.

- **Assign_default**: This component assigns high default values to the nominal life, mean life and *std*. Since our objective is to minimize the three objectives, high default values are assigned to these variables so that the optimizer is not misled.

- **Data Exchanger**: This acts as a preprocessor for the FFD process. The values of the design variables are written into files by this component in the format required by the FFD.

- **FFD**: This component extracts the core from the base model and performs FFD to produce a new core shape on the basis of the values held by the 40 design variables.

- **Generate Deformed Core**: This is a CAD based component that takes the solid blade model (without any internal passages) and performs a Boolean subtraction of the newly produced core from this solid model resulting in a fresh nominal geometry.

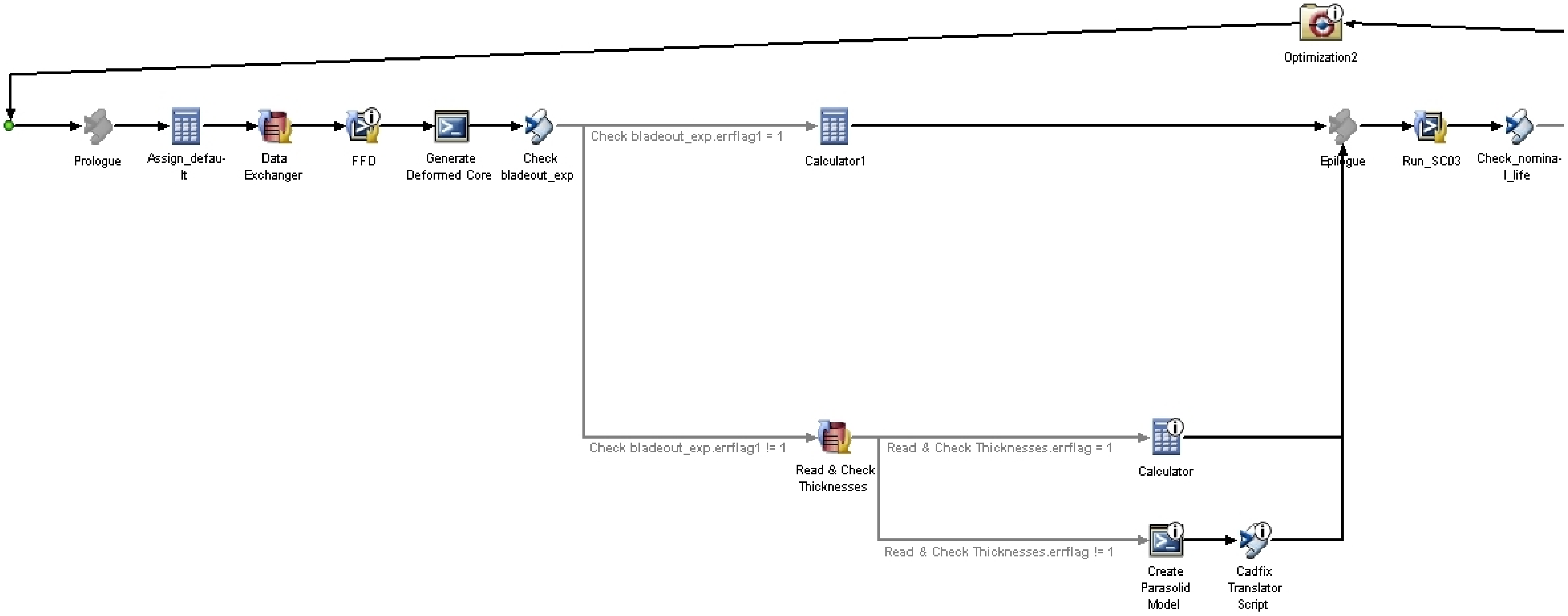

Figure C.1: The workflow used for changing the design intent (CDI) of the turbine blades for robust design optimization.

- **Check bladeout_exp**: This component consists of a JAVA script that checks if the blade geometry file has been created successfully by the previous component. Based on the availability of this file, it assigns a value of 1 or 0 to the variable $errflag1$. $errflag1 = 1$ implies that the geometry file has not been created. In that case, the rest of the workflow is not executed due to the conditional statement following this component. The workflow carries on as normal if the value of $errflag1 \neq 1$.

- **Calculator1**: This is a dummy component that helps in skipping the rest of the workflow if the geometry file is not created by the CAD tool.

- **Read & Check Thicknesses**: This component measures the 18 thickness values on the new nominal design. It then checks if any of these 18 values are negative or zero. Zero or negative values imply that the core has protruded out of the blade surface, and in that case, the rest of the workflow is skipped by applying a conditional check on the value of $errflag$.

- **Calculator**: This is a dummy component that assists in skipping the remainder of the workflow if the core has protruded out of the blade surface.

- **Create Parasolid Model** and **Cadfix Translator Script**: These two components use Parasolid and CADfix to fix any mismatching faces in the nominal geometry model created by the CAD tool. These mismatches may have occurred when the base core was picked up and modified by the FFD process in order to create a new core model. Such problems in the geometry usually lead to failure of the meshing routines in the FEA tool. The repaired geometry model obtained from these components is finally converted into a format readable by the FEA tool and passed on.

- **Epilogue**: This component consists of a JAVA script that aids the Prologue in parallel execution. As stated before, the Prologue and Epilogue were disabled in the current workflow.

- **Run_SC03**: This component consists of a batch script that generates a mesh on the new design and performs FE calculations for estimating the value of nominal life.

- **Check_nominal_life**: This component consists of a JAVA script that checks if the nominal life is greater than or equal to 1.2. If this condition is satisfied, a value 0 is assigned to *errflag_life* which allows the nominal mesh to pass through to the MVA workflow.

The workflow explained in this section was developed as a separate work package in the Computational Engineering and Design Group, University of Southampton in collaboration with Rolls-Royce plc. The purpose of this workflow was to change the design of the turbine blades. Further details on the execution of various components and processes constituting this workflow are beyond the scope of the present work. For the technical details of this workflow, the reader is referred to the RR technical report [162].

C.2 Accounting for Manufacturing Variations

A zoomed in view of the MVA workflow is shown in Figure C.2. Various components of this workflow are described as follows:

- **manuf_life**: This component is the main driver for the MVA workflow. It picks up the nominal mesh from the CDI workflow and passes it on to the various components of the MVA workflow.
- **Get_gbp_file**: This component is a preprocessor that creates the files needed for the FEA.
- **Prep_SC03**: This component is also essentially a preprocessing unit. It extracts the core surface and blade surface meshes from the volume mesh of the nominal turbine blade. These surface meshes are used later for FFD and mesh morphing.
- **Prep_MATLAB**: This component is a preprocessor that uses a MATLAB script for creating the input files needed for the FFD process. If the execution of the MATLAB script fails, a value of -1.0 is passed on to *exit_code_prepmatlab* which takes the control of the workflow to the next run, without executing the subsequent components.
- **calc_coords**: This component calculates the perturbations to be applied to each new nominal mesh based on the thickness values of the new model.
- **Uncertainty**: This is the main driver for another subflow in the loop. This subflow is responsible for applying the 42 sets of manufacturing perturbations to the nominal

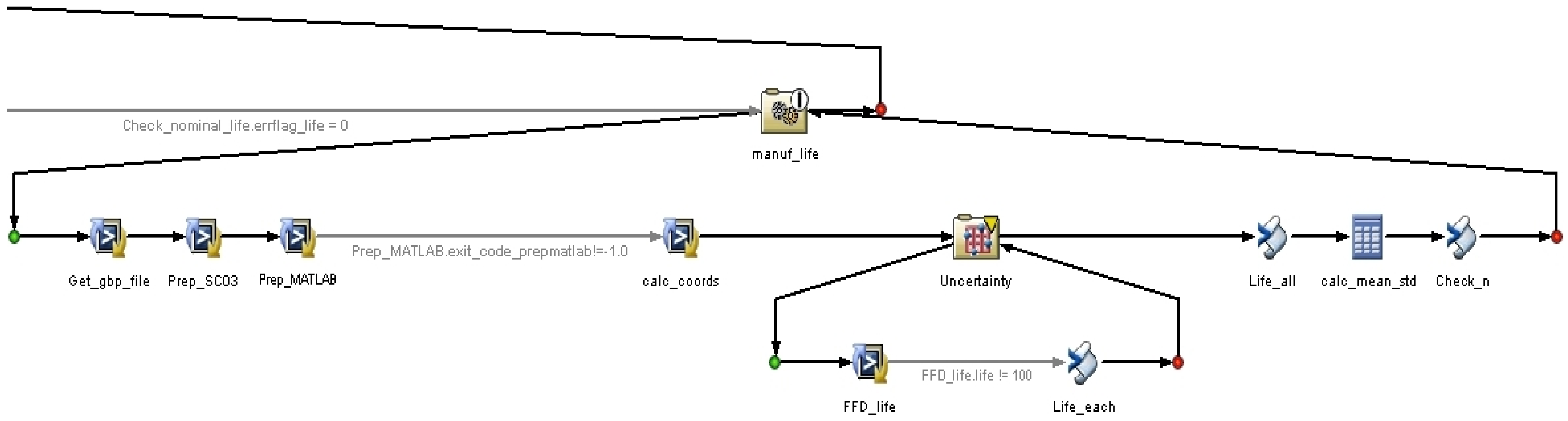

Figure C.2: The workflow used for manufacturing variability analysis (MVA) on each of the new turbine blade designs coming out of the CDI.

mesh and performing FEA for estimating the probable values of life. The subflow can be executed in parallel or in series based on the settings of this component.

- **FFD_life**: This component performs a series of functions. First, it executes the FFD and non-linear optimization on the nominal core in order to generate the probable manufactured core shapes. It then extracts the nodal displacements to be applied to the nominal core for each new shape of the core. This is followed by the application of the LES based approach for morphing the blade volume mesh. Finally, FEA is carried out to estimate the life for each probable shape of the turbine blades. The default value assigned to the blade life is 100. If any of the 42 meshes fail, care is taken that these default values are not passed on to the next component by imposing a check on the value of life.
- **Life_each**: This component consists of a JAVA script that picks up the value of life for each successful run of **FFD_life** and writes it into a file that is needed by the next component.
- **Life_all**: This component executes a JAVA script that picks up the values of life from the files created by **Life_each** and populates these values into an array.
- **calc_mean_std**: This component picks up the array containing the values of life for each probable manufactured blade shape and calculates the mean and standard deviation.
- **Check_n**: This component imposes a check on the number of meshes that went successfully through the FE analysis. If this number is zero, default values are assigned to the mean life and *std*, or else, these values remain unchanged. This component was modified later to add a penalty value to the standard deviation depending on the number of failed meshes.

The details on the implementation of the FFD and LES based methodologies and the FE analysis for estimating the effects of manufacturing variability on turbine blade life have already been presented in Chapters 4 and 5. The values of mean life and *std* calculated from this workflow for each new nominal design were passed on to NSGA-II for the optimization process.

Appendix D

Codes for PCA and FFT Analysis

The codes for PCA and FFT analysis were written in MATLAB. These codes pick up the measurement data, filter out the measurement error from this data based on the threshold values, and finally reconstruct the measurements capturing the effects of manufacturing variability with time.

D.1 PCA Analysis

```
%Step 1 - Load the group data
X = load(‘data.txt’);
%Step 2 - Calculation of the Empirical Mean
MeanData = mean(X,2);
U = MeanData;
%Step 3 - Calculation of the deviations from the Mean
[n,m] = size(X);
uh = repmat(U,1,m);
B = X - uh;
%Step 4 - Calculation of the Covariance Matrix
c = B*B’;
C = c/(m-1);
%Step 5 - Finding the EigenValues and EigenVectors of the Covariance matrix
[EigVec,EigVal] = eigs(C, n);
V = EigVec;
```

```
open threshold_variance_plot.fig %Open the threshold variance plot
pause
hold on;

%Reconstruction
for j = 1:n
vec = V(:,1:j);
for i = 1:1:m
a = vec\B(:,i);
error(:,i) = B(:,i)-(vec*a);
recon_blade(:,i) = vec*a + U; %Reconstructed blades
end;

%For getting the mean blade per group
mean_blade = mean(recon_blade,2);

%Plot the variance per measurement position for each group
variance = var(error,0,2);
plot(variance,‘b--’);

%This portion of the code is used for visual examination of
%dimensionality reduction and for determining the correct dimensionality
%by comparing the means of mean variances.
pause
mean_var = mean(variance)*ones(1,n);
plot(mean_var,‘r--’);
pause

end;
```

D.2 FFT Analysis

```
clear all;
close all;
timestamp = load('Timestamp.txt'); %Load the timestamp of manufacturing
time = mat2cell(timestamp,[length(timestamp)],[3 3]);
load data.txt; %Load measurement data for all the blades comprising one group
[n m] = size(data);
x = [time{1,2} data];
x = sortrows(x); %Sort the data according to time of manufacture
%Perform Fourier Transform
z = reshape(x,n*m,1);
plot(z(1:n*m),'b+-');
y = fft(z);
Pyy = y.*conj(y);
for i=1:m*n
    if abs(y(i))<TM %selected a value of TM based on data
        y(i) = 0;
    end;
end;
iy = real(ifft(y));
hold on
plot(iy(1:m*n),'rx-');
```

Appendix E

Codes for Free Form Deformation (FFD)

The codes for FFD were written in MATLAB. These codes were divided into two modules. The first module, '**ffd.m**', encloses the geometry in lattice control points, initializes all the variables needed for the optimization process, calls the optimizer and invokes a subroutine for performing the objective function calculations. Finally, this code picks up the optimal values of control points and reconstructs the whole deformed geometry. The second module, '**optffd.m**', is a subroutine that is invoked by **ffd.m** for obtaining the deformed coordinates of the measurement points and calculating the objective function value based on these deformed positions. This module is run repeatedly by the optimizer until the convergence of the objective function is achieved.

E.1 Main Module

This is the main module, '**ffd.m**'.

```
clear all;
close all;

global l; %declaring global variables to pass on to ffdfunction
global m;
global n;
```

```
global Bk;

global Bj;

global Bi;

global LatticeCtrlPts;

global Bk_new;

global Bj_new;

global Bi_new;

global expected;


%load the coordinates of the core surface mesh

cord = load('Core_coordinates.txt');


X = cord(:,1);

Y = cord(:,2);

Z = cord(:,3);

%input file is ready


%Calculating the center point of solid

max_x = max(X);

min_x = min(X);

max_y = max(Y);

min_y = min(Y);

max_z = max(Z);

min_z = min(Z);


Cntr_x = (max_x + min_x)/2;

Cntr_y = (max_y + min_y)/2;

Cntr_z = (max_z + min_z)/2;


%Calculating half dimensions/radius along each axis

HalfDimX = (max_x - min_x)/2;

HalfDimY = (max_y - min_y)/2;

HalfDimZ = (max_z - min_z)/2;
```

```
%Calculate the LatticeOrigin

LatticeOrigin_x = Cntr_x - HalfDimX;

LatticeOrigin_y = Cntr_y - HalfDimY;

LatticeOrigin_z = Cntr_z - HalfDimZ;

LatticeOrigin = [LatticeOrigin_x LatticeOrigin_y LatticeOrigin_z];


%Number of intervals to subdivide along each axis

NumIntX = 2;

NumIntY = 1;

NumIntZ = 7;


%Calculate actual dimension of solid

DimX = HalfDimX*2;

DimY = HalfDimY*2;

DimZ = HalfDimZ*2;


%Calculate step vectors along each axis

StepInX = DimX / NumIntX;

StepInY = DimY / NumIntY;

StepInZ = DimZ / NumIntZ;


%Find co-ordinates of lattice control points

NumIntZ_mod = NumIntZ;

k = 1;

TempX = LatticeOrigin_x;

for i = 1:NumIntX+1

    TempY = LatticeOrigin_y;

    for j = 1:NumIntY+1

        TempZ = LatticeOrigin_z;

        for k = k:NumIntZ_mod+1

            LatticeCtrlPts(k,1) = TempX;

            LatticeCtrlPts(k,2) = TempY;
```

```
            LatticeCtrlPts(k,3) = TempZ;

            TempZ = TempZ + StepInZ;

        end;

        TempY = TempY + StepInY;

        NumIntZ_mod = NumIntZ + k;

        k = k + 1;

    end;

    TempX = TempX + StepInX;

end;


%Finding (s,t,u) points for the co-ordinates defining the solid

for i = 1:length(X)

    stu(i,1) = (X(i,1) - LatticeOrigin(1))/DimX;

    stu(i,2) = (Y(i,1) - LatticeOrigin(2))/DimY;

    stu(i,3) = (Z(i,1) - LatticeOrigin(3))/DimZ;

end;


%Calculate the Bernstein basis functions

s = stu(:,1);

t = stu(:,2);

u = stu(:,3);

l = NumIntX;

m = NumIntY;

n = NumIntZ;




for r = 1:length(s)


for k = 0:n

    f(k+1) = factorial(n)/(factorial(n-k)*factorial(k));

    Bk(r,k+1) = f(k+1)*((1-u(r))^(n-k))*(u(r)^k);

end;
```

```
for j = 0:m

    f(j+1) = factorial(m)/(factorial(m-j)*factorial(j));

    Bj(r,j+1) = f(j+1)*((1-t(r))^(m-j))*(t(r)^j);

end;


for i = 0:l

    f(i+1) = factorial(l)/(factorial(l-i)*factorial(i));

    Bi(r,i+1) = f(i+1)*((1-s(r))^(l-i))*(s(r)^i);

end;


end;


%load index of the measurement locations

index = load('index_nodes.txt');


Bk_new = Bk(index,:);

Bj_new = Bj(index,:);

Bi_new = Bi(index,:);


%initializing the 48 variables for lower and upper bound calculations

init_controlpts(1:4,:) = LatticeCtrlPts(4:7,:);

init_controlpts(5:8,:) = LatticeCtrlPts(12:15,:);

init_controlpts(9:12,:) = LatticeCtrlPts(20:23,:);

init_controlpts(13:16,:) = LatticeCtrlPts(28:31,:);

init_controlpts(17:20,:) = LatticeCtrlPts(36:39,:);

init_controlpts(21:24,:) = LatticeCtrlPts(44:47,:);


%calculating the lower bounds for 24 variables

lb_variables = init_controlpts - (10*ones(24,2));


%calculating the upper bounds for 24 variables

ub_variables = init_controlpts + (10*ones(24,2));
```

```
%calculating the lb and ub for all 48 lattice control points
lb(1:3,:) = LatticeCtrlPts(1:3,:);
lb(4:7,:) = lb_variables(1:4,:);
lb(8:11,:) = LatticeCtrlPts(8:11,:);
lb(12:15,:) = lb_variables(5:8,:);
lb(16:19,:) = LatticeCtrlPts(16:19,:);
lb(20:23,:) = lb_variables(9:12,:);
lb(24:27,:) = LatticeCtrlPts(24:27,:);
lb(28:31,:) = lb_variables(13:16,:);
lb(32:35,:) = LatticeCtrlPts(32:35,:);
lb(36:39,:) = lb_variables(17:20,:);
lb(40:43,:) = LatticeCtrlPts(40:43,:);
lb(44:47,:) = lb_variables(21:24,:);
lb(48,:) = LatticeCtrlPts(48,:);

ub(1:3,:) = LatticeCtrlPts(1:3,:);
ub(4:7,:) = ub_variables(1:4,:);
ub(8:11,:) = LatticeCtrlPts(8:11,:);
ub(12:15,:) = ub_variables(5:8,:);
ub(16:19,:) = LatticeCtrlPts(16:19,:);
ub(20:23,:) = ub_variables(9:12,:);
ub(24:27,:) = LatticeCtrlPts(24:27,:);
ub(28:31,:) = ub_variables(13:16,:);
ub(32:35,:) = LatticeCtrlPts(32:35,:);
ub(36:39,:) = ub_variables(17:20,:);
ub(40:43,:) = LatticeCtrlPts(40:43,:);
ub(44:47,:) = ub_variables(21:24,:);
ub(48,:) = LatticeCtrlPts(48,:);

%Load the desired coordinates of measurement points
expected = load('Expected_xy.txt');

%call the subroutine for optimization
```

```
fun = @optffd;
init_lcp = LatticeCtrlPts(:,1:2);
[final_controlpts,fval,exitflag,output] = fmincon(fun,init_lcp,[],[],[],[],lb,
ub);
%Optimal lcp positions obtained
New_LatticeCtrlPts = [final_controlpts LatticeCtrlPts(:,3)];
%Reconstruct the deformed core coordinates
for r = 1:length(Bk)
    p = 1; New_X(r,1:3) = 0;
for i = 0:l
    New_X1(r,1:3) =0;
for j = 0:m
    New_X2(r,1:3) = 0;
for k = 0:n
    New_X2(r,1) = New_X2(r,1) + (Bk(r,k+1)*New_LatticeCtrlPts(p,1));
    New_X2(r,2) = New_X2(r,2) + (Bk(r,k+1)*New_LatticeCtrlPts(p,2));
    New_X2(r,3) = New_X2(r,3) + (Bk(r,k+1)*New_LatticeCtrlPts(p,3));
    p = p+1;
end;
New_X1(r,1) = New_X1(r,1) + New_X2(r,1)*Bj(r,j+1);
New_X1(r,2) = New_X1(r,2) + New_X2(r,2)*Bj(r,j+1);
New_X1(r,3) = New_X1(r,3) + New_X2(r,3)*Bj(r,j+1);
end;
New_X(r,1) = New_X(r,1) + New_X1(r,1)*Bi(r,i+1);
New_X(r,2) = New_X(r,2) + New_X1(r,2)*Bi(r,i+1);
New_X(r,3) = New_X(r,3) + New_X1(r,3)*Bi(r,i+1);
end;
end;

%clearing the global variables
clear global l;
clear global m;
clear global n;
```

```
clear global Bk;

clear global Bj;

clear global Bi;

clear global LatticeCtrlPts;

clear global Bk_new;

clear global Bj_new;

clear global Bi_new;

clear global expected;
```

E.2 Subroutine

This is the subroutine, '**optffd.m**', called by the main module.

```
function Objective = optffd(controlpts)


global l; %passing the global variables

global m;

global n;

global Bk;

global Bj;

global Bi;

global LatticeCtrlPts;

global Bk_new;

global Bj_new;

global Bi_new;

global expected;


%Modify LatticeCtrlPts to deform

LatticeCtrlPts = [controlpts LatticeCtrlPts(:,3)];


%Calculate the new coordinates for measurement points

for r = 1:length(Bk_new)
```

```
    p = 1; New_X(r,1:3) = 0;
for i = 0:l
    New_X1(r,1:3) =0;
for j = 0:m
    New_X2(r,1:3) = 0;
for k = 0:n
    New_X2(r,1) = New_X2(r,1) + (Bk_new(r,k+1)*LatticeCtrlPts(p,1));
    New_X2(r,2) = New_X2(r,2) + (Bk_new(r,k+1)*LatticeCtrlPts(p,2));
    New_X2(r,3) = New_X2(r,3) + (Bk_new(r,k+1)*LatticeCtrlPts(p,3));
    p = p+1;
end;
New_X1(r,1) = New_X1(r,1) + New_X2(r,1)*Bj_new(r,j+1);
New_X1(r,2) = New_X1(r,2) + New_X2(r,2)*Bj_new(r,j+1);
New_X1(r,3) = New_X1(r,3) + New_X2(r,3)*Bj_new(r,j+1);
end;
New_X(r,1) = New_X(r,1) + New_X1(r,1)*Bi_new(r,i+1);
New_X(r,2) = New_X(r,2) + New_X1(r,2)*Bi_new(r,i+1);
New_X(r,3) = New_X(r,3) + New_X1(r,3)*Bi_new(r,i+1);
end;
end;

%Calculate the Objective function for the expected (x,y) values and
%deformed (x,y) positions of nodes in the morphed mesh.

Objective = 0;
for i = 1:length(New_X)
     Objective = Objective + ((New_X(i,1)-expected(i,1))^2 +
     (New_X(i,2)-expected(i,2))^2);
end;
```

Bibliography

[1] A. Kumar, Robust Design Methodologies: Application to Compressor Blades, Ph.D. thesis, School of Engineering Sciences, University of Southampton, Southampton, UK (2006).

[2] C. W. Moeckel, Probabilistic Turbine Blade Thermal Analysis of Manufacturing Variability and Toleranced Designs, Master's thesis, Department of Aeronautics and Astronautics, Massachusetts Institute of Technology (2006).

[3] Rolls-Royce, Delivering value through services for the 21st century, Webpage, http://www.rolls-royce.com/service/downloads/service.pdf (2004).

[4] S. Bagnall, D. Shaw, J. Mason-Flucke, Implications of 'Power by the Hour' on Turbine Blade Lifing, in: RTO AVT Specialists' Meeting on Design for Low Cost Operation and Support, Ottawa, Canada, 1999, pp. 12(1)–12(10).

[5] D. Robinson, A survey of probabilistic methods used in reliability, risk and uncertainty analysis: Analytical Techniques I, Tech. Rep. SAND98-1189, Sandia National Laboratories, Livermore, California (1998).

[6] T. A. Zang, M. J. Hemsch, M. W. Hilburger, S. P. Kenny, J. M. Luckring, P. Maghami, S. L. Padula, W. J. Stroud, Needs and Opportunities for Uncertainty-Based Multidisciplinary Design Methods for Aerospace Vehicles, Tech. Rep. NASA/TM-2002-211462, NASA Langley Research Center, Hampton, Virginia (2002).

[7] V. E. Garzon, D. L. Darmofal, Impact of geometric variability on axial compressor performance, Journal of Turbomachinery 125 (4) (2003) 692–703.

[8] D. Mavris, B. Roth, Assessment of Uncertainty in Aerospace Propulsion System Design and Simulation, Scholarly Materials and Research at Georgia Tech (SMARTech),

http://smartech.gatech.edu/bitstream/1853/6421/1/JANNAF03_final_manuscript.pdf (2003).

[9] C. V. Sidwell, On the Impact of Variability and Assembly on Turbine Blade Cooling Flow and Oxidation Life, Ph.D. thesis, Department of Aeronautics and Astronautics, Massachusetts Institute of Technology (2004).

[10] V. E. Garzon, Probabilistic Aerothermal Design of Compressor Airfoils, Ph.D. thesis, Massachusetts Institute of Technology (2003).

[11] V. Carl, E. Becker, A. Sperling, Quantitative wall thickness Measurement with Impulse-Video-Thermography, in: 7th European Conference on Non-Destructive Testing, Copenhagen, Denmark, ECNDT, 1998.

[12] A. Bronnikov, D. Killian, 3d Tomography of Turbine Blades, in: International Symposium on Computerized Tomography for Industrial Applications and Image Processing in Radiology, Berlin, Germany, Vol. 4, 1999.

[13] Y. L. Bihan, P.-Y. Joubert, D. Placko, Wall thickness evaluation of single-crystal hollow blades by eddy current sensor, NDT and E International 34 (5) (2001) 363–368.

[14] T. W. Sederberg, S. R. Parry, Free-Form Deformation of Solid Geometric Models, Computer Graphics 20 (4) (1986) 151–160.

[15] Engineous, iSIGHT, Webpage, http://www.engineous.com/iSIGHT.cfm (2008).

[16] I. TranscenData, CADfix, Webpage, http://www.transcendata.com/products/cadfix/ (2010).

[17] S. P. Software, Parasolid, Webpage, http://tinyurl.com/y8dupx3 (2010).

[18] K. Deb, A. Pratap, S. Agarwal, T. Meyarivan, A Fast and Elitist Multiobjective Genetic Algorithm: NSGA-II, IEEE Transactions on Evolutionary Computation 6 (2) (2002) 182–197.

[19] J. Shlens, A Tutorial on Principal Component Analysis, Tutorial lecture notes, http://www.snl.salk.edu/ shlens/pub/notes/pca.pdf (2005).

[20] L. I. Smith, A tutorial on Principal Component Analysis, Student Tutorial, http://reflect.otago.ac.nz/cosc453/student_tutorials/principal_components.pdf (2002).

[21] M. E. Wall, A. Rechtsteiner, L. M. Rocha, A Practical Approach to Microarray Data Analysis, Kluwer: Norwell, Ch. 5, pp. 91–109.

[22] G. Zsemlye, Shape Prediction from Partial Information, Ph.D. thesis, Swiss Federal Institute of Techology, Zurich, Switzerland (2005).

[23] B. Allen, B. Curless, Z. Popović, The space of human body shapes: reconstruction and parameterization from range scans, in: ACM SIGGRAPH 2003, ACM, San Diego, CA, USA, 2003.

[24] M. Ferreira, C. Faria, E. Paes, Oceanographic characterization of northern Sao Paulo Coast: a chemometric study, Chemometrics and Intelligent Laboratory Systems 47 (2) (1999) 289–297.

[25] K.-P. Chiang, A. Taniguchi, Distribution and modification of diatom assemblages in and around a warm core ring in the western North Pacific Frontal Zone east of Hokkaido, Journal of Plankton Research 22 (11) (2000) 2061–2074.

[26] P.-A. Baeriswyl, M. Rebetez, Regionalization of Precipitation in Switzerland by Means of Principal Component Analysis, Theoretical and Applied Climatology 58 (1997) 31–41.

[27] M. Rabbette, P. Pilewskie, Principal Component Analysis of Arctic Solar Irradiance Spectra, Webpage, http://geo.arc.nasa.gov/sgp/radiation/rad5.html.

[28] M. Hagan, R. Roble, J. R. III, M. Mlynczak, Complex Principal Component Analysis in the middle Atmosphere : A Feasibility Study using Satellite Sampled Model Data and its Possible Application to Saber Temperatures, in: EGS - AGU - EUG Joint Assembly, Nice, France, Vol. 5, European Geophysical Society, 2003.

[29] N. S. Rao, D. J. Devadas, K. S. Rao, Interpretation of groundwater quality using principal component analysis from Anantapur district, Andhra Pradesh, India, Environmental Geosciences 13 (4) (2006) 239 – 259.

[30] D. Klassen, R. Howell, P. Johnson, J. Bell, Principal Components Analysis of Martian Spectral Images, in: 28th Annual Meeting of the Division for Planetary Sciences of the American Astronomical Society, Tucson, Arizona, 1996.

[31] D. P. Donovan, A. I. Carswell, Principal component analysis applied to multiwavelength lidar aerosol backscatter and extinction measurments, Applied Optics 36 (36) (1997) 9406–9424.

[32] V. Šmídl, A. Quinn, On Bayesian principal component analysis, Computational Statistics & Data Analysis 51 (9) (2007) 4101–4123.

[33] M. E. Tipping, C. M. Bishop, Probabilistic Principal Component Analysis, Journal of the Royal Statistical Society: Series B (Statistical Methodology) 61 (3) (1999) 611–622.

[34] I. Jolliffe, Principal Component Analysis, Springer Series in Statistics, Second Edition, Springer, New York, USA, 2002.

[35] J. Mandel, Use of the Singular Value Decomposition in Regression Analysis, The American Statistician 36 (1) (1982) 15–24.

[36] T. P. Minka, Automatic choice of dimensionality for PCA, Tech. Rep. 514, MIT Media Laboratory, Vision and Modeling Group, 20 Ames Street, http://vismod.media.mit.edu/tech-reports/TR-514.pdf (2000).

[37] H.-L. Wei, S. A. Billings, Feature Subset Selection and Ranking for Data Dimensionality Reduction, IEEE Transactions on Pattern Analysis and Machine Intelligence 29 (1) (2007) 162–166.

[38] L. van der Maaten, An Introduction to Dimensionality Reduction Using Matlab, Tech. Rep. MICC 07-07, Universiteit Maastricht, Maastricht, The Netherlands (2007).

[39] M. T. Heideman, D. H. Johnson, C. S. Burrus, Gauss and the History of the Fast Fourier Transform, ASSP Magazine, IEEE 1 (4) (1984) 14–21.

[40] J. W. Cooley, J. W. Tukey, An Algorithm for the Machine Calculation of Complex Fourier Series, Mathematics of Computation 19 (90) (1965) 297–301.

[41] S. W. Smith, The Scientist and Engineer's Guide to Digital Signal Processing, California Technical Publishing, San Diego, CA, USA, 1997.

[42] R. Martin, D. Malah, R. V. Cox, A Noise Reduction Preprocessor for Mobile Voice Communication, EURASIP Journal on Applied Signal Processing 8 (2004) 1046–1058.

[43] I. Nakanishi, Y. Itoh, Y. Fukui, K. Fujii, Noise Reduction System using Modified DFT Pair, in: IEEE International Symposium on Circuits and Systems, ISCAS 2001, Sydney, Australia, Vol. 2, 2001, pp. 9–12.

[44] R. C. Hendriks, J. Jensen, , R. Heusdens, Noise Tracking Using DFT Domain Subspace Decompositions, IEEE Transactions on Audio, Speech, and Language Processing 16 (3) (2008) 541–553.

[45] H. Bensmail, J. Golek, M. M. Moody, J. O. Semmes, A. Haoudi, A novel approach for clustering proteomics data using Bayesian fast Fourier Transform, Bioinformatics 21 (10) (2005) 2210–2224.

[46] A. Abdel-Hafiez, Fourier Transformation Methods in the Field of Gamma Spectrometry, International Journal of Pure and Applied Physics 3 (1) (2007) 132–141.

[47] T. S. Ralston, I. Atkinson, F. Kamalabadi, S. A. Boppart, Multi-Dimensional Denoising of Real-Time Oct Imaging Data, in: IEEE International Conference on Acoustics, Speech and Signal Processing, ICASSP 2006, Vol. 2, 2006, pp. 1148–1151.

[48] C. Brown, W. Dreyer, W. Müller, Discrete Fourier Transforms and Their Application to Stress-Strain Problems in Composite Mechanics: A Convergence Study, Proceedings: Mathematical, Physical and Engineering Sciences 458 (2024) (2002) 1967–1987.

[49] O. Shentov, S. Mitra, U. Heute, A. Hossen, Subband DFT - Part I: Definition, interpretation and extensions, Signal Processing 41 (1995) 261–277.

[50] H. Guo, G. Sitton, C. Burrus, The Quick Discrete Fourier Transform, in: IEEE International Conference on Acoustics, Speech, and Signal Processing, ICASSP-94, Vol. III, 1994, pp. 445–448.

[51] S. Winograd, On Computing the Discrete Fourier Transform, Proceedings of the National Academy of Sciences of the United States of America 73 (4) (1976) 1005–1006.

[52] S. Winograd, On Computing the Discrete Fourier Transform, Mathematics of Computation 32 (141) (1978) 175–199.

[53] C. M. Rader, N. Brenner, A New Principle for Fast Fourier Transformation, IEEE Transactions on Acoustics, Speech and Signal Processing 24 (3) (1976) 264–266.

[54] D. M. Monro, Algorithm AS 83: Complex Discrete Fast Fourier Transform, Applied Statistics 24 (1) (1975) 153–160.

[55] D. M. Monro, Algorithm AS 97: Real Discrete Fast Fourier Transform, Applied Statistics 25 (2) (1976) 166–172.

[56] S. G. Johnson, M. Frigo, A modified split-radix FFT with fewer arithmetic operations, IEEE Transactions on Signal Processing 55 (1) (2007) 111–119.

[57] H. V. Sorensen, M. T. Heideman, Real-Valued Fast Fourier Transform Algorithms, IEEE Transactions on Acoustics, Speech and Signal Processing ASSP-35 (6) (1987) 849–863.

[58] M. Frigo, S. G. Johnson, The Design and Implementation of FFTW3, Proceedings of the IEEE 93 (2) (2005) 216–231.

[59] D. H. Klyde, R. E. Magdaleno, J. G. Reinsberg, The Effect of Tire Pressure on Aircraft Ground Handling, in: AIAA Atmospheric Flight Mechanics Conference, Monterey, CA, USA, no. 586, 2002.

[60] L. Chen, D. Edwards, Applications of Non-Uniform Sampling Techniques and Fast Fourier Transform in Plane Near-Field Antenna Measurements, in: Eighth International Conference on Antennas and Propagation, no. 1, 1993, pp. 311–314.

[61] W. H. Press, S. A. Teukolsky, W. T. Vetterling, B. P. Flannery, Numerical Recipes in FORTRAN, 2nd Edition, Cambridge University Press, 1994.

[62] V. Cherkassky, FFT Tutorial, Tutorial, http://www.phys.nsu.ru/cherk/fft.pdf (cited December 2008).

[63] S. N. bin Yahya, N. binti Mohd Suaib, A. bin Bade, S. M. B. H. Shamsuddin, Solid Deformation Modeling Techniques, Asian Journal of Information Technology 5 (3) (2006) 324–338.

[64] H. J. Lamousin, J. Warren N. Waggenspack, NURBS-Based Free-Form Deformations, Computer Graphics and Applications, IEEE 14 (6) (1994) 59–65.

[65] S. Coquillart, Extended Free-Form Deformation: A Sculpturing Tool for 3D Geometric Modeling, Computer Graphics 24 (4) (1990) 187–196.

[66] W. M. Hsu, J. F. Hughes, H. Kaufman, Direct Manipulation of Free-Form Deformations, Computer Graphics 26 (2) (1992) 177–184.

[67] N. Frisch, T. Ertl, Deformation of Finite Element Meshes using Directly Manipulated Free-Form Deformation, in: Proceedings of the seventh ACM symposium on Solid modeling and applications, Saarbrucken, Germany, ACM, 2002, pp. 249–256.

[68] R. A. Noble, G. J. Clapworthy, Direct Manipulation of Surfaces using NURBS-Based Free-Form Deformations, in: Proceedings of the IEEE International Conference on Information Visualization, 1999, pp. 238–243.

[69] P. Faloutsos, M. van de Panne, D. Terzopoulos, Dynamic Free-Form Deformations for Animation Synthesis, IEEE Transactions on Visualization and Computer Graphics 3 (3) (1997) 201–214.

[70] K. Singh, E. Kokkevis, Skinning Characters using Surface-Oriented Free-Form Deformations, in: Graphics Interface, 2000, pp. 35–42.

[71] J.-A. Désidéri, A. Janka, Multilevel Shape Parameterization for Aerodynamic Optimization - Application to Drag and Noise Reduction of Transonic/Supersonic Business Jet, in: P. Neittaanmaki, T. Rossi, S. Korotov, E. Onate, J. Periaux, D. Knorzer (Eds.), European Congress on Computational Methods in Applied Sciences and Engineering (ECCOMAS 2004), Jyväskylä, 2004.

[72] B. A. E. Majd, R. Duvigneau, J.-A. Désidéri, Aerodynamic shape optimization using a full and adaptive multilevel algorithm, in: G. Winter, J. Periaux, W. Haase, B. Galvan, B. Gonzalez, D. Greiner, A. Blesa (Eds.), Design Optimisation : Methods and Applications (ERCOFTAC 2006), 2006.

[73] J. A. Samareh, Aerodynamic Shape Optimization based on Free-Form Deformation, Vol. 6 of Collection of Technical Papers - 10th AIAA/ISSMO Multidisciplinary Analysis and Optimization Conference, 2004, pp. 3672–3683.

[74] S. S. Sarakinos, E. Amoiralis, I. K. Nikolos, Exploring Freeform Deformation Capabilities in Aerodynamic Shape Parameterization, in: The International Conference on Computer as a Tool (EUROCON 2005), Vol. 1, 2005, pp. 535–538.

[75] G. Farin, A History of Curves and Surfaces in CAGD, in: G. Farin, M. S. Kim, J. Hoschek (Eds.), Handbook of CAGD, Elsevier, 2002.

[76] K. M. Neuerburg, Bézier Curves, in: Proceedings of the Louisiana-Mississippi Section of the Mathematical Association of America, Clinton, MS, 2003.

[77] A. Requicha, H. Voelcker, Solid Modeling: A Historical Summary and Contemporary Assessment, IEEE Computer Graphics and Applications 2 (2) (1982) 9–24.

[78] S. S. Rao, Engineering Optimization Theory and Practice, 3rd Edition, Wiley-Interscience Publishers, John Wiley & Sons, Inc., and New Age International Publishers, Ltd., 1996.

[79] A. J. Keane, P. B. Nair, Computational Approaches for Aerospace Design, John Wiley & Sons Ltd., Chichester, West Sussex, England, 2005.

[80] R. Byrd, J. Gilbert, J. Nocedal, A Trust Region Method Based on Interior Point Techniques for Nonlinear Programming, Mathematical Programming 89 (1) (2000) 149–185.

[81] R. Byrd, M. E. Hribar, J. Nocedal, An Interior Point Algorithm for Large-Scale Nonlinear Programming, SIAM Journal on Optimization 9 (4) (1999) 877–900.

[82] T. Coleman, Y. Li, An Interior, Trust Region Approach for Nonlinear Minimization Subject to Bounds, SIAM Journal on Optimization 6 (1996) 418–445.

[83] T. Coleman, Y. Li, On the Convergence of Reflective Newton Methods for Large-Scale Nonlinear Minimization Subject to Bounds, Mathematical Programming 67 (2) (1994) 189–224.

[84] S. Han, A Globally Convergent Method for Nonlinear Programming, Journal of Optimization Theory and Applications 22 (1977) 297.

[85] R. Waltz, J. Morales, J. Nocedal, D. Orban, An interior algorithm for nonlinear optimization that combines line search and trust region steps, Mathematical Programming 107 (3) (2006) 391–408.

[86] P. Gill, W. Murray, M. Wright, Practical Optimization, Academic Press, London, UK, 1981.

[87] T. Coleman, Y. Li, A Reflective Newton Method for Minimizing a Quadratic Function Subject to Bounds on Some of the Variables, SIAM Journal on Optimization 6 (4) (1996) 1040–1058.

[88] M. Alexa, Recent Advances in Mesh Morphing, Computer Graphics Forum 21 (2) (2002) 173–196.

[89] K. Stein, T. Tezduyar, R. Benney, Mesh Moving Techniques for Fluid-Structure Interactions With Large Displacements, ASME Journal of Applied Mechanics 70 (2003) 58–63.

[90] S. Jakobsson, O. Amoignon, Mesh deformation using radial basis functions for gradient-based aerodynamic shape optimization, Computers & Fluids 36 (2007) 1119–1136.

[91] B. T. Helenbrook, Mesh deformation using the biharmonic operator, International Journal for Numerical Methods in Engineering 56 (2003) 1007–1021.

[92] C. Burg, Analytic study of 2D and 3D grid motion using modified Laplacian, International Journal for Numerical Methods in Fluids 52 (2006) 163–197.

[93] S. M. Shontz, S. A. Vavasis, A mesh warping algorithm based on weighted Laplacian smoothing, in: Proceedings of the 12th International Meshing Round-table, Santa Fe, USA, 2003, pp. 147–158.

[94] K. Stein, R. Benney, V. Kalro, T. E. Tezduyar, J. Leonard, M. Accorsi, Parachute fluid-structure interactions: 3-D computation, Computer Methods in Applied Mechanics and Engineering 190 (2000) 373–386.

[95] T. E. Tezduyar, S. Sathe, R. Keedy, K. Stein, Space-time finite element techniques for computation of fluid-structure interactions, Computer Methods in Applied Mechanics and Engineering 195 (17-18) (2005) 2002–2027.

[96] M. T. Bah, P. B. Nair, M. Browne, Mesh morphing for finite element analysis of implant positioning in cementless total hip replacements, Medical Engineering & Physics 31 (2009) 1235–1243.

[97] W. S. Slaughter, The Linearized Theory of Elasticity, Birkhäuser, Boston, USA, 2002.

[98] K.-J. Bathe, Finite Element Procedures, Prentice-Hall of India Private Limited, New Delhi, India, 2006.

[99] A. A. Giunta, S. F. W. Jr., M. S. Eldred, Overview of Modern Design of Experiments Methods for Computational Simulations, in: Proceedings of the 41st AIAA Aerospace Sciences Meeting and Exhibit, no. AIAA 2003-0649, Reno, Nevada, USA, 2003.

[100] J. Antony, Design of Experiments for Engineers and Scientists, Butterworth-Heinemann publications, Oxford, UK, 2003.

[101] I. Sobol, The distribution of points in a cube and approximate evaluation of integrals, USSR Computational Mathematics and Mathematical Physics 7 (1967) 86–112.

[102] I. Sobol, On the Systematic Search in a Hypercube, SIAM Journal on Numerical Analysis 16 (5) (1979) 790–793.

[103] I. Sobol, On quasi-Monte Carlo integrations, Mathematics and Computers in Simulation 47 (1998) 103–112.

[104] I. Sobol, B. Shukhman, Quasi-random points keep their distance, Mathematics and Computers in Simulation 75 (2007) 80–86.

[105] P. Bratley, B. L. Fox, Algorithm 659 Implementing Sobol's Quasirandom Sequence Generator, ACM Transactions on Mathematical Software 14 (1) (1988) 88–100.

[106] G. Matheron, Principles of geostatistics, Economic Geology 58 (1963) 1246–1266.

[107] D. Krige, A statistical approach to some mine valuations and allied problems at the Witwatersrand, Master's thesis, University of Witwatersrand, Johannesburg, South Africa (1951).

[108] J. Sacks, W. J. Welch, T. J. Mitchell, H. P. Wynn, Design and Analysis of Computer Experiments, Statistical Science 4 (4) (1989) 409–423.

[109] A. Keane, Wing Optimization Using Design of Experiment, Response Surface, and Data Fusion Methods, Journal of Aircraft 40 (4) (2003) 741–750.

[110] A. J. Keane, Comparison of Several Optimization Strategies for Robust Turbine Blade Design, Journal of Propulsion and Power 25 (5) (2009) 1092–1099.

[111] A. I. Forrester, A. J. Keane, Recent advances in surrogate-based optimization, Progress in Aerospace Sciences 45 (2009) 50–79.

[112] M. Schonlau, Computer Experiments and Global Optimization, Ph.D. thesis, University of Waterloo, Ontario, Canada (1997).

[113] D. R. Jones, M. Schonlau, W. J. Welch, Efficient global optimization of expensive black-box functions, Journal of Global Optimization 13 (1998) 455–492.

[114] D. R. Jones, A Taxonomy of Global Optimization Methods Based on Response Surfaces, Journal of Global Optimization 21 (2001) 345–383.

[115] A. I. Forrester, A. Sóbester, A. J. Keane, Engineering Design via Surrogate Modelling: A Practical Guide, John Wiley & Sons Ltd., West Sussex, UK, 2008.

[116] A. Keane, The OPTIONS Design Exploration System User Guide and Reference Manual, Webpage, http://www.soton.ac.uk/ãjk/options.ps (cited March 2010).

[117] J. L. Loeppky, J. Sacks, W. J. Welch, Choosing the Sample Size of a Computer Experiment: A Practical Guide, Technometrics 51 (4) (2009) 366–376.

[118] A. Rao, Manufacturing Cost Based Methodologies for Design Optimisation, Ph.D. thesis, School of Engineering Sciences, University of Southampton, Southampton, UK (2006).

[119] P. S. Pande, R. P. Neuman, R. R. Cavanagh, The Six Sigma Way: How GE, Motorola and Other Top Companies Are Honing Their Performance, McGraw-Hill Companies Inc., USA, 2000.

[120] S. M. Sanchez, Robust Design: Seeking the best of all possible worlds, in: J. Joines, R. Barton, K. Kang, P. Fishwick (Eds.), Proceedings of the 2000 Winter Simulation Conference, Orlando, Florida, USA, 2000, pp. 69–76.

[121] T. A. Cruse, Non-Deterministic, Non-traditional Methods (NDNTM), Tech. Rep. NASA/CR-2001-210976, NASA Glenn Research Center, Cleveland, Ohio, USA (2001).

[122] D. A. DeLaurentis, D. N. Mavris, Uncertainty Modeling and Management in Multidisciplinary Analysis and Synthesis, in: 38th AIAA Aerospace Sciences Meeting and Exhibit, no. AIAA-2000-0422, Reno, Nevada, USA, 2000.

[123] S. M. N., Robust Design, Tech. rep., Department of Aerospace Engineering, Indian Institute of Technology, Bombay, India (2002).

[124] R. H. Myers, A. I. Khuri, G. Vining, Response Surface Alternatives to the Taguchi Robust Parameter Design Approach, The American Statistician 46 (2) (1992) 131–139.

[125] M. W. Trosset, Taguchi and Robust Optimization, Tech. rep., Department of Computational & Applied Mathematics, Rice University, Houston, Texas, USA (1997).

[126] E. Capiez-Lernout, C. Soize, J.-P. Lombard, C. Dupont, E. Seinturier, Blade Manufacturing Tolerances Definition for a Mistuned Industrial Bladed Disk, Journal of Engineering for Gas Turbines and Power 127 (2005) 621–628.

[127] R. Unal, D. O. Stanley, C. R. Joyner, Propulsion System Design Optimization Using the Taguchi Method, IEEE Transactions on Engineering Management 40 (3) (1993) 315–322.

[128] V. N. Nair, Taguchi's Parameter Design: A Panel Discussion, Technometrics 34 (1992) 127–161.

[129] A. Shoemaker, K. Tsui, C. Wu, Economical Experimentation Methods for Robust Parameter Design, Technometrics 33 (4) (1991) 415–427.

[130] W. Welch, T.-K. Yu, S. M. Kang, J. Sacks, Computer Experiments for Quality Control by Parameter Design, Journal of Quality Technology 22 (1990) 15–22.

[131] G. Box, S. Jones, Designing products that are robust to the environment, Total Quality Management & Business Excellence 3 (3) (1992) 265–282.

[132] R. H. Myers, A. I. Khuri, G. Vining, Response Surface Alternatives to the Taguchi Robust Parameter Design Approach, The American Statistician 46 (2) (1992) 131–139.

[133] L. Huyse, R. M. Lewis, Aerodynamic Shape Optimization of Two-dimensional Airfoils Under Uncertain Conditions, Tech. Rep. NASA/CR-2001-210648, NASA Langley Research Center, Hampton, Virginia, USA (2001).

[134] A. Ben-Tal, A. Nemirovski, Robust Truss Topology Design via Semidefinite Programming, SIAM Journal on Optimization 7 (1997) 991–1016.

[135] C. Wang, D. Li, Z. Li, X. Jiang, Optimization of Controllers for Gas Turbine Based on Probabilistic Robustness, Journal of Engineering for Gas Turbines and Power 131 (5) (2009) 054502:1–054502:5.

[136] H.-G. Beyer, B. Sendhoff, Robust optimization - a comprehensive survey, Computer Methods in Applied Mechanics and Engineering 196 (2007) 3190–3218.

[137] S. Tsutsui, A. Ghosh, Y. Fujimoto, A Robust Solution Searching Scheme in Genetic Search, in: Parallel Problem Solving from Nature, Springer-Verlag, Berlin, Germany, 1996, pp. 543–552.

[138] S. Tsutsui, A. Ghosh, Genetic Algorithms with a Robust Solution Searching Scheme, IEEE Transactions on Evolutionary Computation 1 (3) (1997) 201–208.

[139] D. Parkinson, Robust Design by Variability Optimization, Quality and Reliability Engineering International 13 (1997) 97–102.

[140] I. Das, Robustness Optimization for Constrained Nonlinear Programming Problems, Engineering Optimization 32 (5) (2000) 585–618.

[141] S.-B. Yoon, I.-S. Jung, D.-S. Hyun, Robust Shape Optimization of Electromechanical Devices, IEEE Transactions on Magnetics 35 (3) (1999) 1710–1713.

[142] Y. Jin, B. Sendhoff, Trade-Off between Performance and Robustness: An Evolutionary Multiobjective Approach, in: C. F. et al. (Ed.), Evolutionary Multi-Criterion Optimization, Springer-Verlag, Berlin, Germany, 2003, pp. 237–251.

[143] A. Kumar, A. J. Keane, P. B. Nair, S. Shahpar, Robust Design of Compressor Fan Blades Against Erosion, Journal of Mechanical Design 128 (4) (2006) 864–873.

[144] A. Kumar, P. B. Nair, A. J. Keane, S. Shahpar, Robust design using Bayesian Monte Carlo, International Journal for Numerical Methods in Engineering 73 (2008) 1497–1517.

[145] I. Das, J. Dennis, A closer look at drawbacks of minimizing weighted sums of objectives for Pareto set generation in multicriteria optimization problems, Structural Optimization 14 (1997) 63–69.

[146] K. Deb, Multi-objective Genetic Algorithms: Problem Difficulties and Construction of Test Problems, Evolutionary Computation 7 (3) (1999) 205–230.

[147] J. Schaffer, Multiple objective optimization with vector evaluated genetic algorithms, in: J. Grefenstette (Ed.), Proceeding of the First International Conference on Genetic Algorithms, Lawrence Erlbaum, 1985, pp. 93–100.

[148] J. Horn, N. Nafpliotis, D. E. Goldberg, A Niched Pareto Genetic Algorithm for Multiobjective Optimization, in: Proceeding of the First IEEE Conference on Evolutionary Computation, Vol. 1, New Jersey, USA, 1994, pp. 82–87.

[149] C. M. Fonseca, P. J. Fleming, Genetic Algorithms for Multiobjective Optimization: Formulation, Discussion and Generalization, in: S. Forrest (Ed.), Proceeding of the Fifth International Conference on Genetic Algorithms, Morgan Kaufmann, California, USA, 1993, pp. 416–423.

[150] C. Fonseca, P. Fleming, An Overview of Evolutionary Algorithms in Multiobjective Optimization, Evolutionary Computation 3 (1) (1995) 1–16.

[151] A. Konak, D. Coit, A. Smith, Multi-objective optimization using genetic algorithms: A tutorial, Reliability Engineering and System Safety 91 (2006) 992–1007.

[152] A. Dias, J. de Vasconcelos, Multiobjective Genetic Algorithms Applied to Solve Optimization Problems, IEEE Transactions on Magnetics 38 (2) (2002) 1133–1136.

[153] A. French, J. Poulsen, A. Yu, Multivariate Analysis of Variance (MANOVA), Online lecture notes, http://online.sfsu.edu/∼efc/classes/biol710/manova/manovanew.htm (cited December 2008).

[154] C. Creveling, Tolerance Design A handbook for developing Optimal Specifications, Addison Wesley Longman, Inc., Reading, Massachusetts, 1997.

[155] G. Carey, Multivariate Analysis of Variance (MANOVA): I. Theory, Lecture notes, http://ibgwww.colorado.edu/∼carey/p7291dir/handouts/manova1.pdf (cited December 2008).

[156] D. Roff, Comparing G Matrices: A Manova Approach, Evolution 56 (6) (2002) 1286–1291.

[157] D. Moitre, F. Magnago, Using MANOVA Methodology in a Competitive Electric Market under Uncertainties, in: Transmission & Distribution Conference and Exposition: Latin America. TDC ’06. IEEE/PES, 2006, pp. 1–6.

[158] S. S. Kajarekar, H. Hermansky, Analysis of Information in Speech Based on MANOVA, in: NIPS, 2002, pp. 1189–1196.

[159] R. J. Harris, A Primer of Multivariate Statistics, 3rd Edition, Lawrence Erlbaum Associates, 2001.

[160] M. H. Kutner, C. J. Nachtsheim, J. Neter, W. Li, Applied Linear Statistical Models, 5th Edition, The McGraw-Hill Companies, Inc., 2005.

[161] M. H. DeGroot, M. J. Schervish, Probability and Statistics, 3rd Edition, Addison-Wesley, 2002.

[162] A. Rao, Automated Analysis Workflow Development for Design Optimisation, Tech. Rep. DNS 137948, Rolls-Royce plc., Derby, UK (2007).